Atomic Scale Electron Spin Resonance at High Zeeman Energies

Von der Fakultät Mathematik und Physik der Universität Stuttgart zur Erlangung der Würde eines Doktors der Naturwissenschaften (Dr. rer. nat.) genehmigte Abhandlung.

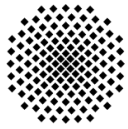

University of Stuttgart
Germany

vorgelegt von

Piotr Kot

aus Stuttgart

Hauptberichter	Dr. habil. Christian R. Ast
Mitberichter	Prof. Dr. Sebastian Loth
Prüfungsvorsitzende	Prof. Dr. Maria Daghofer

Tag der mündlichen Prüfung: 10.05.2022

Universität Stuttgart &
Max-Planck Institut für Festkörperforschung
2022

Acknowledgements

Whenever someone stands on the precipice of success, they are always there due to the contributions, advice and support of many people. Here are all the people that have helped me to successfully complete this dissertation.

First, I would like to thank Dr. habil. Christian R. Ast, my direct supervisor and thesis director. You took me in as your student back when I was still completing my bachelor's degree, and every year I learn more and more from you. My current level of scientific expertise and confidence are a direct result of your supervision. For that, I am deeply grateful.

To Prof. Klaus Kern, the director of my department, thank you for accepting me into the institute seven years ago. You were always there to support my research financially, but equally as important, you were also always there to motivate me to continue even when I had lost hope.

I would like to thank my thesis committee for their interest and evaluation of my work, Prof. Maria Daghofer and Prof. Sebastian Loth.

I would have not been able to accomplish the tasks presented in this dissertation without someone to teach me how to use the experiment. Robert Drost, thank you for taking the time and effort to share your knowledge of STMs and for always supporting me with any crazy idea I had. Aparajita Singha, thank you for sharing your expertise on electron spin resonance scanning tunneling microscopy. Your advice directly led us to measuring our first resonance signals.

To the people in my group, Haonan Huang, Maneesha Ismail, Sujoy Karan, Janis Siebrecht and Maximilian Uhl, I thank you for the comradery that I experienced with all of you and for all the insightful discussions we've had in our group meetings.

The department I was a part of for the past seven years has also supported me immensely in that time, with different people in the department providing help in different ways. To the

engineers in our department, Wolfgan Stiepany, Peter Andler and Marco Memmler, thank you for always being ready to fix whatever equipment happened to break at the time. You three were always prompt and effective at repairing whatever the issue may be. To Sabine Birtel, I do not think anyone in the department would survive without you. Your knowledge of the bureaucracy and intricacies of the institute is necessary for all of us to reach our goals. I thank you for all the help you have provided me. Lastly, to the fellow researchers in my department, I thank you all for the support and discussions we had on the institute grounds and the great parties and events we had off the institute grounds.

To my friends in Germany, with whom there is a large overlap with my department-mates, I spent the last seven years growing and learning with you. From the lows to the highs, I always had an ear to listen to me, a mouth to advise me and arms to embrace me. I will terribly miss you all and I hope many of you will visit me in Korea!

To my friends abroad, both in Poland and Canada, thank you for always supporting my endeavors even when it was not always clear what they were. All the continual encouragement never made me doubt whether completing a PhD is a good idea for me. I also hope to see many of you in Korea!

I would also like to thank Mr. Anthony J. Klassen, who sparked my passion for science when I was just a teenager in his physics classrom.

Lastly, and most importantly, I would like to thank my family. To my grandma, Wiera Walkowa, my aunt, Anna Młyniec, and my two little cousins, Michał and Piotruś, thank you for giving me a home away from home during my stay in Europe. I always knew that during the holidays I had family to return to. To my parents, Grażyna Kot and Aleksander Kot, I don't think I can write in words the emotions I am feeling right now. All of the success, opportunity and privilege I have experienced is because of you two. For that I will be grateful for the rest of my life.

List of Publications

1. Kot, P. *et al.* Electric field control of spin transitions on the atomic scale. *in preparation*

2. Uhl, M., Kot, P., Drost, R., Huang, H., Cuevas, J. C., & Ast, C. R. Multiband Josephson Effect in a Pb Tunnel Junction. *in preparation*

3. Drost, R., Uhl M., Kot, P., Siebrecht, J., Schmid, A., Merkt, J., Wünsch, S., Siegel, M., Kieler, O., Kleiner, R., & Ast, C. R. Combining Electron Spin Resonance Spectroscopy with Scanning Tunneling Microscopy at High Magnetic Fields. arXiv:2111.05910, (in review, 2022)

4. Kot, P., Drost, R., Uhl, M., Ankerhold, J., Cuevas, J. C., & Ast, C. R. Microwave-assisted tunneling and interference effects in superconducting junctions under fast driving signals. *Phys. Rev. B* **101**, 134507 (2020)

Abstract

Scanning tunneling microscopy (STM) and electron spin resonance (ESR) are both powerful tools for investigating physical phenomena in materials. The combination of the two has been sought out by the scientific community for decades and was successfully realized and demonstrated in 2015. Since then ESR-STM has been shown to be an extraordinary technique for studying the physics of spins on the atomic scale. In its short lifespan the community has shown the coherent control of single spins, the smallest magnetic resonance image of a single atom, the measurement of the flip flop rate between two entangled spin states and many more scientifically relevant and exciting results. With the goal to join this community, we present in this dissertation the development and first results of a new state of the art ESR-STM.

In the first half of this thesis we outline the way we designed a high frequency (HF) antenna and outfitted a commercial STM with HF cabling that allows us to measure resonance signals at up to three times higher Zeeman energy (ZE) than previously reported. We had to design and implement both HF cabling and a HF antenna, as it is increasingly difficult to deliver radio signals the higher their frequency. Our desired frequency range was 60 GHz to 90 GHz which, with a base temperature of 320 mK, would allow us to operate in a regime where the spin state is initialized to the ground state. Prior to initial ESR measurements we also took the opportunity to study microwave-assisted tunneling in superconducting junctions. This was in conjunction with measuring the transfer function of our HF set-up, which was done by observing the Tien-Gordon (TG) response of the coherence peaks. We provide insight into the tunneling processes that occur in a superconducting gap using microwave-assisted tunneling, and find that the separate processes interact with each other due to the TG model breaking down at high conductances.

In the second half of the thesis we present our first results showing ESR sweeps from 60 GHz to 98 GHz, establishing that we successfully implemented an ESR-STM that functions in our designed operational frequency range. We then follow the proof of principle with the first two projects we worked on, bias dependent ESR-STM and temperature dependent ESR-STM.

We show that spin transitions couple to the electric field in the junction due to a *g*-factor and tip field modulation that occurs when the spin system moves away from the substrate. We show that this should be a general effect for any spin system whose *g*-factor is dependent on the crystal field or spin-orbit coupling. Furthermore, we use this bias dependent ESR technique to control several spin transitions by shifting them from a region where the transitions are of equal energy to one where they are not, simply by changing the bias. In this way we demonstrate that the bias is one more tuning parameter in ESR experiments, similar to the tip field. Lastly, with temperature dependent ESR-STM we show preliminary data and specify challenges that have to be overcome. With the preliminary results we speculate that the system initializes around 1 K and that the temperature dependency of the ESR peak is dependent on the ZE.

Zusammenfassung

Rastertunnelmikroskopie (RTM) und Elektronenspinresonanz (ESR) sind leistungsfähige Werkzeuge zur Untersuchung physikalischer Phänomene in Materialien. Die Kombination der zwei Techniken wurde über Jahrzehnte von der wissenschaftlichen Gemeinschaft angestrebt und im Jahr 2015 erfolgreich umgesetzt und demonstriert. Seitdem hat sich ESR-RTM als außergewöhnliche Technik zur Erforschung der Physik von Spins auf atomarer Ebene erwiesen. Innerhalb kurzer Zeit hat die wissenschaftliche Gemeinschaft die kohärente Kontrolle einzelner Spins, das kleinste Magnetresonanzbild eines Atoms, die Messung der Flip-Flop-Rate zwischen verschränkten Spinzuständen und viele weitere wissenschaftlich relevante und spannende Ergebnisse gezeigt. Mit dem Ziel, ein Teil dieser wissenschaftlichen Gemeinschaft zu werden, präsentieren wir in dieser Dissertation die Entwicklung und erste Ergebnisse eines ESR-RTMs auf dem neuesten Stand der Technik.

In der ersten Hälfte der Arbeit skizzieren wir, wie wir eine Hochfrequenzantenne (HF-Antenne) konstruiert haben und ein RTM mit HF-Verkabelung ausgestattet haben, was es uns ermöglicht, Resonanzsignale bei Zeeman-Energien (ZE) zu messen, die bis zu dreimal höher liegen als bisher berichtet. Wir mussten sowohl die HF-Verkabelung wie auch die HF-Antenne konstruieren und implementieren, da es mit höherer Frequenz zunehmend schwieriger wird, Radiosignale zu übertragen. Unser angestrebter Frequenzbereich war 60 GHz bis 90 GHz, was es uns ermöglichen sollte, mit einer Basistemperatur von 320 mK in einem Regime zu arbeiten, in dem der Spinzustand im Grundzustand initialisiert ist. Vor den ESR-Messungen haben wir außerdem die Möglichkeit genutzt, mikrowellenunterstütztes Tunneln in supraleitenden Kontakten zu untersuchen. Dies erfolgte in Verbindung mit der Messung der Transferfunktion unserer HF-Verkabelung, welche durchgeführt wurde, indem das Tien-Gordon (TG)-Verhalten der Kohärenzpeaks beobachtet wurde. Wir bieten Einblicke in die Tunnelprozesse, die in einer supraleitenden Energielücke bei mikrowellenunterstütztem Tunneln stattfinden. Wir finden, dass die verschiedenen Prozesse aufgrund des Scheiterns des TG-Modells bei hohen Leitfähigkeiten miteinander interagieren.

In der zweiten Hälfte der Arbeit präsentieren wir unsere ersten Ergebnisse und zeigen ESR-Spektren von 60 GHz bis zu 98 GHz, was darlegt, dass wir erfolgreich die Technik des ESR-RTMs implementiert haben und dass diese im gewählten Frequenzbereich funktioniert. Nach dem Proof-of-Principle-Nachweis folgen zwei Projekte, an denen wir gearbeitet haben, nämlich von der Biasspannung abhängiges ESR-RTM und temperaturabhängiges ESR-RTM. Wir zeigen, dass Spinübergänge aufgrund einer Modulation des *g*-Faktors und im Magnetfeld der Spitze, die stattfindet, wenn das Spinsystem sich vom Substrat entfernt, mit dem elektrischen Feld im Tunnelkontakt wechselwirken. Wir zeigen, dass dies ein allgemeiner Effekt für jedes Spinsystem, dessen *g*-Faktor vom Kristallfeld oder der Spin-Bahn-Kopplung abhängt, ist. Außerdem nutzen wir von der Biasspannung abhängiges ESR-RTM, um mehrere Spinübergänge zu kontrollieren und um sie von einer Region, in der die Übergänge bei gleicher Energie sind, zu einer Region, wo dies nicht der Fall ist, zu bewegen. Auf diese Weise zeigen wir, dass die Vorspannung eine weitere Stellgröße in ESR-Experimenten ist, ähnlich dem Magnetfeld der Spitze. Zum Schluss zeigen wir zum Thema Temperaturabhängigkeit vorläufige Daten und spezifizieren Herausforderungen, die bewältigt werden müssen. Mit den vorläufigen Ergebnissen spekulieren wir, dass das System bei etwa 1 K initialisiert wird und dass die Temperaturabhängigkeit des ESR-Maximums von der ZE abhängt.

Contents

List of Figures

List of Acronyms

CP	Cooper pair
DC	direct current
DFT	density functional theory
DOS	density of states
ESR	electron spin resonance
FCS	full counting statistics
FES	field emission spectroscopy
FG	frequency generator
FWHM	full width at half-maximum
HF	high frequency (60 - 100 GHz)
IETS	inelastic tunneling spectroscopy
IVC	inter vacuum chamber
LHe	liquid helium-4
LN_2	liquid nitrogen
LF	low frequency (0 - 40 GHz)
MARs	multiple Andreev reflections
ML	monolayer
NMR	nuclear magnetic resonance
PSD	power spectral density
RF	radio frequency
STM	scanning tunneling microscopy
SC	superconductor
SIS	superconductor-insulator-superconductor
SP	spin-polarized
TF	transfer function
TG	Tien-Gordon
TM	Tedrow-Meservey
STS	scanning tunneling spectroscopy
UHV	ultra-high vacuum
ZE	Zeeman energy

1 Introduction

In the famous lecture ”There’s plenty of room at the bottom”, the idea was posited to engineer materials on the atomic scale [29]. Many researchers attribute this to be the spark that birthed the field of nanoscience, and a good portion of scientific resources in the past six decades have been put into exploring this idea. In fact many concepts in this lecture have been realized in the past decades, for example the manipulation and controllable rearrangement of atoms, the ability to store information on the nanoscale, and the miniaturization of electronics and computers [36, 43, 60, 66, 94]. Recently work has even begun on ideas past the original lecture in the form of using quantum properties of nanoscale objects to perform quantum computations [3, 24, 40]. Even with these developments, there are many ideas and phenomena that are not yet feasible and/or applicable in practice; resources are continued to be put into study of nanotechnology and the field is of great interest to the scientific community.

To achieve the aforementioned feats, scientists have had to build special tools to investigate and control materials down to the nanoscale. One of these tools is scanning tunneling microscopy (STM) [13]. STM is a form of scanning probe microscopy where one brings a physical probe close to the material of interest in order to image and study the surface. Furthermore, the physical probe, known as the tip, can be used to manipulate the surface and is even able to move, pick up and drop individual atoms [11, 94]. With such a tool researchers are able to make images of surfaces down to picometer resolution, study the magnetic, electronic and physical properties of materials down to the atomic scale, and even make movies by moving atoms and using them as pixels [10, 18, 25, 35, 57, 116]! Currently, STMs are often combined with other functionalities, which allow them to study phenomena that are usually not accessible with a basic STM. For example, in photon-STMs a photon detector is put near the STM junction to investigate the emission of light induced by the current on the material [78]. Another example is the implementation of pump-probe schemes into STMs that allow them to study temporal dynamics down to nanosecond resolution [55]. One of the functionalities that the STM community had fervently tried to combine with STMs is electron spin resonance

(ESR) [7, 59]. This was first convincingly demonstrated in 2015 and the technique has since then been aptly named ESR-STM [11].

ESR is a form of spin resonance and is used to study the magnetic properties of materials [118]. Very importantly, its cousin nuclear magnetic resonance (NMR), is a technique that has revolutionized medical imaging and characterization of chemical and physical compounds [23, 30]. We are now even able to take real time NMR images and see directly how internal biological mechanisms function [102]. ESR has similar capabilities but is more suited to studying spin physics at higher energies. The combination of ESR and STM has led to many novel observations and experiments such as: making the smallest magnetic resonance image on a single atom, the study of singlet and triplet transitions in coupled spin systems, the ability to coherently control the states of an individual spin, the real time observation of two spins flip flopping and the investigation into magnetic fields of individual atoms [6, 16, 104, 109, 113]. Even in its infancy, it is clear that ESR-STM is a very powerful tool to study magnetic properties of materials on the nanoscale. With the general goal in mind of pushing the field of nanotechnology forward, and the more specific goal to be able to study spin physics on the atomic scale, we present in this dissertation the development of a new state of the art ESR-STM that is capable of probing resonances at triple the energies previously reported [11, 84, 103, 104, 108].

Our motivation to push the energy splitting of our ESR-STM experiments beyond the norm is twofold. The first reason is that we wanted to take advantage of the Tedrow-Meservey (TM) effect which would require for us to work at higher magnetic fields than previously reported [62]. As the strength of the field is directly related to the energy of the resonance, the large fields that are needed for the TM effect makes it neccessary for us to be able to access resonances at high energies. The second reason why we wanted to expand the energy limit of ESR-STMs is that we wanted have a system where the spin was initialized to the ground state at base temperature. This would allow us to probe the thermally induced transition from a regime where only the ground state is populated to one where there is a mixture between the excited and ground state. Both of these ideas are investigated in this thesis. To access these two possibilities we first purchased a low temperature STM that has a base temperature of 300 mK, and then we outfitted the machine with high frequency (HF) cabling and a HF antenna that lets us radiate into the junction at frequencies from 60 GHz to 98 GHz. The details behind the HF cabling and antenna, along with the different methodologies used in the experiments performed during this thesis, are presented in the upcoming chapter. Chap. 3 then summarizes the theoretical background and knowledge needed to understand the remainder of the dissertation.

The scientific results are presented in the remaining five chapters before a conclusionary chapter. The results can be roughly divided into findings made prior to measuring an ESR signal, and findings made using the full capabilities of the system. The former pertains to studies of microwave-assisted tunneling in superconducting junctions, and studies of vanadyl oxide pthalocyanine molecules on a superconducting surface. In the first project we wanted to use our expertise on superconductors (SCs), along with the tunneling properties of superconducting junctions, to study the transmission of the HF cabling we installed. We successfully characterized the HF delivery of our set-up, and were also able to use microwave-assisted tunneling as a way to study tunneling processes between SCs. We then wanted to understand the feasibility of using the TM effect to measure ESR signals, so we studied a sample system that could use the TM effect in this way. VOPcs on Pb(111) was our system of choice and even though we found challenges in our way to measure an ESR signal, we found that VOPc nanocrystals on Pb(111) were an interesting and unique system that has not yet been reported in literature.

We present proof that our ESR-STM can measure ESR signals within our desired frequency range in Chap. 6, along with the details on how to characterize the tip and sample to perform such a measurement. We also briefly investigate the consequences of using a HF range on our transmission and ESR signals. The last two results chapters hold studies on bias dependent ESR-STM signals and thermally induced population dynamics in a spin system. In the latter we present an initial experiment and show that there are some obstacles that have to be overcome before a more complete experiment can be done. Nevertheless, we believe we see a transition from a regime where the spin is initialized to one where it is not. In the former studies on bias dependent ESR-STM, we find a new effect that has not been observed experimentally and has only been briefly mentioned in literature [28]. What we find is that we can directly control the energy of the spin transition with the bias voltage applied in our STM junction. This effect is due to a change in the *g*-factor of the spin and a change in the tip field felt by the system, which are both induced by a change in the electric field. Furthermore, this phenomenon is found to be stronger than in bulk ESR experiments and we believe it is a general effect for any spin system whose *g*-factor can be modulated by the crystal field or spin-orbit coupling. Lastly, we use this technique to control spin transitions of a coupled spin systems by showing an electrically induced transition from a regime where several transitions are at the same energy to one where they are not.

2 Experimental Methodology

2.1 Principles of Scanning Tunneling Microscopy

2.1.1 Quantum Tunneling

STM, as the name implies, functions on the basis of quantum tunneling. This is a non-classical effect that posits that an electron can pass through a finite energy barrier if the spatial distribution of the electron's wavefunction can reach through the barrier. In the case of STMs we consider the wavefunctions of the two electrodes that form our STM junction, the tip and the sample. If the tip and sample are brought close enough, with a distance of around 1 nm or smaller, the wavefunctions start to overlap through the vacuum space (which is our energy barrier) [101]. When the relative Fermi levels of the tip and sample are shifted, the electrons from the higher energy electrode will want to tunnel into the other electrode. In this way, we create a current between the tip and sample by applying a bias voltage which shifts their relative Fermi energies. This makes one thing clear, both the tip and sample have to be conducting so that there are states for electrons to tunnel into. This does not exclude thin insulating materials, i.e. monolayer (ML) MgO, which is considered to be an additional potential barrier in the tunneling junction. If we keep the bias constant then moving the tip closer to the sample will increase the current with the following dependency on the tip sample distance, z:

$$I \propto \exp(-2\kappa z). \tag{2.1}$$

Here, κ is a decay constant which depends on the mass and energy of the electron and the height of the potential barrier. Based on this equation we can consider the STM junction as a variable resistor whose resistance can be adjusted by the height of the tip (in more complicated models the capacitance also has to be considered). Using this tunneling phenomenon,

we can get topographical information and spectroscopic information of our sample which is explained in the following subsections.

2.1.2 Raster Scanning

Topographical information can be acquired by moving the tip relative to the plane of the sample while tunneling. A very basic schematic representation is shown in Fig. 2.1 where we see an example of a scan in constant current mode. In STM we have two modes, constant current and constant height which both use Eq. 2.2 in different ways. In constant height mode, the z-position of the tip is kept constant and the tip is moved in x and y (the plane of the sample). The current will change depending on the local conductance of the sample which results in topographical data. In the case of constant current, which is the mode in which all topography was taken for in this thesis, we create a feedback loop between z and the current. We ask our tip movement controllers to keep z at such a height that the current is kept constant at our set point current. We then move the tip in x and y and record how the

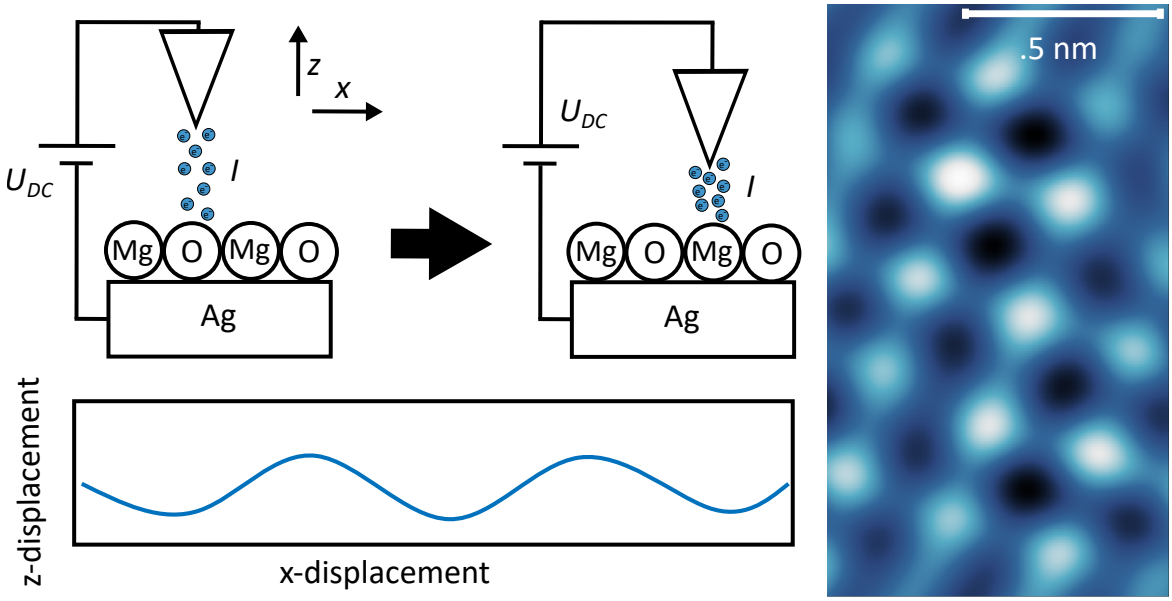

Figure 2.1: Schematic diagram explaining raster scanning in constant current mode. In the top left of the figure we see the z-movement of the tip when it moves from an O atom to an Mg atom as the current, I, is kept constant. In the bottom left we see a schematic of the expected z-displacement when the tip moves over a periodic lattice in the x-direction. Right of the figure shows the Fourier filtered topography of an MgO lattice measured at U_{DC} = -20 mV and I = 9 nA. The dark spots are the positions of Mg atoms and the bright spots are the positions of O atoms.

tip moves in z. As is the case for the constant height mode, local resistivities of the sample will change, and to compensate for the change in resistance the tip will have to move up or down to acquire the set point current. On the top left of Fig. 2.1 is a representation of the movement of the tip in z as it moves from a more conducting O atom to a less conducting Mg atom. We can measure the change in z with respect to to x, and we show what could be expected from the topography of a periodic lattice in the bottom left of Fig. 2.1. If we repeat this measurement at many values of y we can get information on how the z-position of the tip moves in the plane of the sample, which is our topography. On the right of Fig 2.1 we see Fourier filtered topography of a MgO lattice measured in constant current mode ($U_{DC} =$ -20 mV, $I = 9$ nA). We see a periodic square lattice expected for MgO [32]. In practice we do not continuously record the change in z but rather move discretely measuring the change in the tip sample distance point by point, hence why this is considered a form of raster scanning.

It is important to note that typically STMs move their tip and sample with the use of piezoelectric crystals, which are controlled by high voltage electronics. In our case we control the feedback of the set point current and the movement of our scanning piezos with commercially available electronics and software (Nanonis).

2.1.3 Tunneling Spectroscopy

The second piece of information one can acquire in any basic STM set-up is information on the density of states (DOS) of the tip and sample. This is done with a technique called scanning tunneling spectroscopy (STS). In this case the tip and sample distance is kept constant, and the bias applied between the tip and the sample is swept with the resulting current being recorded. If we consider Bardeen's approach, at low temperature the tunneling current is related to the voltage and the DOS of the tip and sample in the following way [63]:

$$I = \frac{4\pi e}{\hbar} \int_0^{eU_{DC}} \rho_{sample}(E_F + \epsilon)\rho_{tip}(E_F + \epsilon - eU_{DC})|M(\epsilon - eU_{DC}, \epsilon)|^2 d\epsilon, \tag{2.2}$$

where M is the tunneling matrix defining the coupling between the electron wavefunctions in the tip and sample. We can see from this that the tunneling current is dependent on the convolution between the DOS of the tip and sample, which can change when there is a shift in their relative Fermi levels. This equation can be further built upon to show that for a tip

with a spherical wavefunction at the apex (s-wave) the DOS of the sample is proportional to the derivative of the current with respect to bias [98].

$$\frac{dI}{dU} \propto \rho_{sample}(eU) \tag{2.3}$$

This equation is the basis of STS and we can see that the $I-U$ characteristics of a junction are directly related to the DOS of the sample. It is important to note that this approximation only works when the tip DOS is constant, which can often be achieved with correct tip shaping. Fig. 2.2 shows a schematic representation of STS where on the left we see the DOS of the tip and sample represented by blue blocks. When a bias voltage is applied, the two DOS move relative to each other in energy, and tunneling electrons from the tip tunnel into the DOS of the sample that is accessible to them at that bias voltage (in the opposite bias the electrons would move in reverse). If the DOS of the sample increases then the resulting dI/dU will increase. A representation of the data one could expect from the DOS on the left side of Fig. 2.2 is shown on the right of the figure.

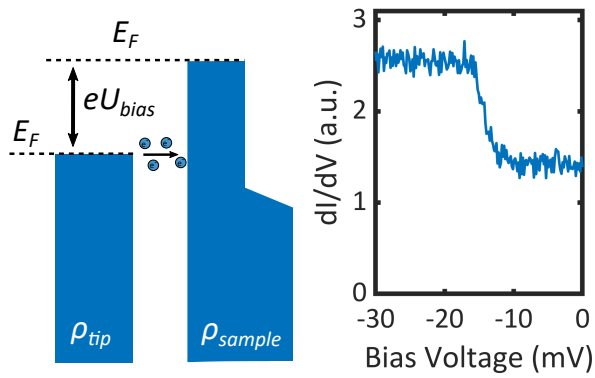

Figure 2.2: Schematic diagram on the left explaining STS. When a bias is applied between the tip and the sample, the relative Fermi levels between the two DOS changes. This causes the tunneling electrons from the tip to probe the change in the DOS of the sample. If there is a larger DOS then more electrons can tunnel. On the right is an example of real spectroscopy of what is schematically shown on the left. Spectroscopy was measured on Fe on MgO/Ag(100) at a set point of U_{DC} 100 mV and $I = 500$ pA.

We also usually use a lock-in amplifier, that is built into the electronics software, to increase signal to noise. We use the amplifier to modulate the bias we apply at a chosen frequency (usually 737 Hz) and then demodulate the current signal we get after it passes through the junction. It can be shown that this resulting signal, the lock-in signal, is proportional to dI/dU [95]. For all spectroscopic data in this dissertation a lock-in amplifier was used, where

we used modulation amplitudes from 50 µV to 1.5 mV depending on the size of the feature we were interested in measuring.

It is also important to state that what has been said in this chapter refers to the basic case where the tunneling process is elastic. There are forms of inelastic tunneling where the tunneling electron interacts with the environment and can either gain or lose energy [4, 37, 78]. A gain in energy only occurs when the environment has enough energy to give which is often provided thermally. As our experiments are at very low temperatures our inelastic tunneling processes involve electrons losing energy. In inelastic tunneling spectroscopy (IETS) there are often energy thresholds at which there is a change in the perceived DOS (i.e. steps in the resulting spectroscopy). In a simple example, a tunneling electron needs to have a certain energy to interact with the environment. If it has enough energy an additional signal can be made by that interaction which we pick up in the current. Examples that are relevant to this thesis are spin excitation spectroscopy and the IETS step found around -80 mV on on-site TiH molecules. We will be discussing spin excitation spectroscopy in more detail in the upcoming chapter. There is one last type of spectroscopy which we briefly use in this thesis. We use field emission spectroscopy (FES) to differentiate between different layered MgO. FES tends to be performed at much higher voltages than the other measurements we performed and the feedback loop of the set point current is kept closed.

2.2 Electron Spin Resonance Scanning Tunneling Microscopy

There are some specific details to performing an ESR-STM experiment that we would like to outline in this subsection. We do this prior to the theoretical background that will be presented on the ESR mechanism in Chap 3, so for now we only have to consider the following to understand the aforementioned details. We perform ESR-STM measurements on a spin system, which in our case is TiH on two ML MgO/Ag(100), that effectively acts as a spin-½ system. The energy levels of this spin system can be separated, or split, with the application of a magnetic field, by a characteristic energy difference called the Zeeman energy (ZE). We drive the spin system with an external RF source that also has a characteristic energy that is proportional to its frequency. The resonance signal can be acquired when the ZE matches the energy of the driving RF radiation. Therefore, we can measure ESR signals either by sweeping the frequency of the radiation, or by sweeping the ZE energy of the spin system by changing the magnetic field.

2.2.1 Generating a Constant Amplitude in the Junction

To sweep the frequency we have to account for the frequency dependent change in the transmission of our HF cabling. This is because we have to keep a constant RF power applied in our junction during these frequency sweeps. The RF response of the tunneling current through the spin system in our experiments is amplitude dependent and therefore an inconsistent amplitude will create large deviations in the baseline of the measurement. An example of this is presented in Chap. 6. To account for this fact we measure a transfer function (TF) which tells us how to attenuate the RF source as a function of frequency. We define the TF in units of dB as follows [68]:

$$T = 20 \log_{10}(\frac{U_{RF}}{1\ mV}). \tag{2.4}$$

We measure the TF by applying RF driving with no attenuation at the junction and extract the RF amplitude by the change in STS. The details of this is dependent on the sample, but one example of how we can extract the RF voltage is presented in Chap. 4. For ESR-STM

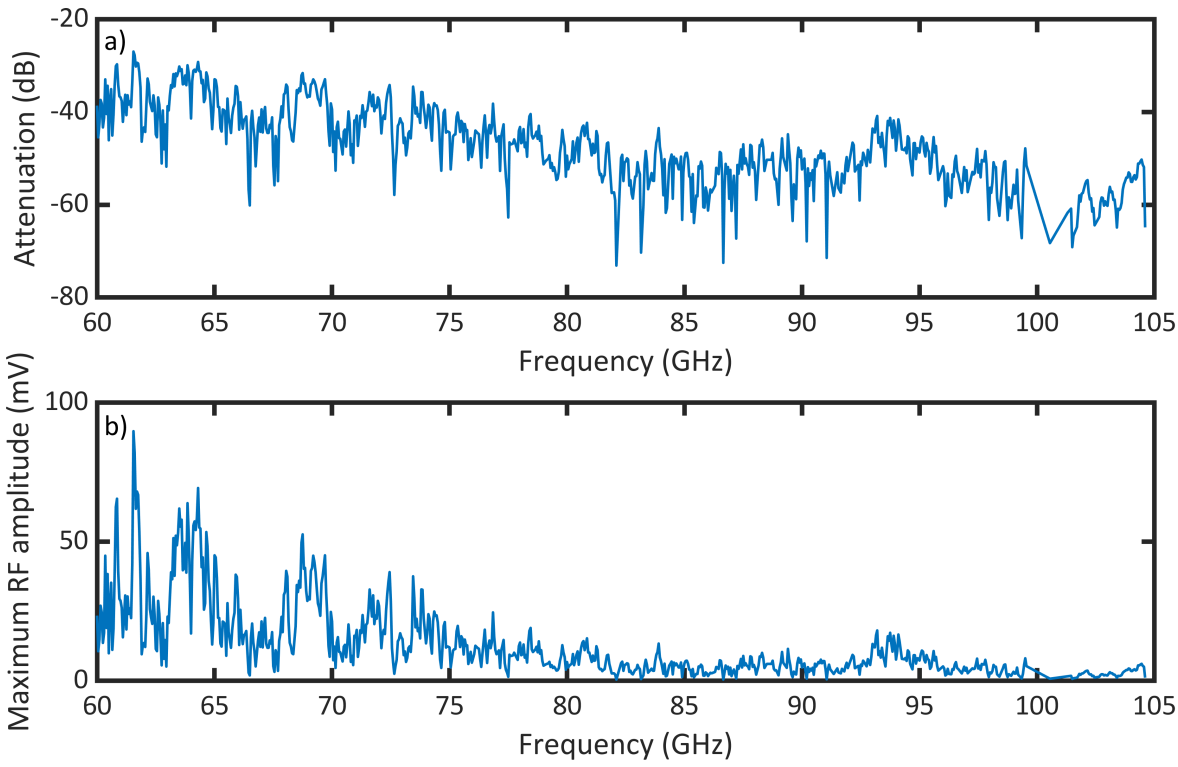

Figure 2.3: The TF of our HF cabling and antenna. a) TF in units of dB. b) TF in units of mV showing the maximum RF voltage we are able to produce in the junction.

experiments, we generally use the RF response of an IETS step found on one of the species of our sample. As the software for the TF acquisition and generation was mainly the work of my colleague, Maximilian Uhl, I refer everyone to his PhD thesis for more details on the development and details of the TF measurements for our ESR-STM experiments. For this dissertation it is important to know we can extract the RF amplitude in the junction based off STS. We do this at all the frequencies we are interested in and measure $T(f_{RF})$. If we then want to apply a constant RF voltage, we solve for how we wish to attenuate with respect to frequency in the following way:

$$A(f_{RF}) = -20 \log_{10}(\frac{U_{RF}}{1\ mV}) + T(f_{RF}). \tag{2.5}$$

Here, U_{RF} is kept constant and $T(f_{RF})$ will lead to defining how we have to attenuate the signal when changing f_{RF}, $A(f_{RF})$ (we apply $A(f_{RF})$ on our variable attenuator during our frequency sweeps). We like to convert the TF into units of voltage, which then ends up representing the maximum RF voltage that is possible at each frequency. This is often more useful for finding good frequencies and frequency ranges as we know the general RF voltage threshold for measuring a signal in our machine, which usually is around $U_{RF} = 10\,\text{mV}$. Both the TF in units of dB and mV is shown in Fig. 2.3. We see generally good transmission from 60 GHz to 80 GHz and from 93 GHz to 96 GHz, and sporadic transmission in all other regions. We find this TF to be more than capable of performing the ESR experiments we wish to complete.

2.2.2 Detection Scheme

The detection scheme for measuring ESR signals is also quite unique and specific to ESR-STM experiments. The full scheme is shown schematically in Fig. 2.4. We start by putting the tip in contact with the spin system of interest and tunneling through it. The set point and bias can be adjusted accordingly to change the position and amplitude of the ESR signal. We tend to start with a set point of 100 mV and 100 pA for the initial sweeps in a project, and we keep the tip in slower feedback parameters during ESR sweeps than during other experiments on the machine. The time constants of the proportional-integral controller parameters are 160 µs and 20 µs respectively, where the time constant here is a measure of how quickly the controller changes the feedback and is the ratio of the proportional gain and integral gain of the controller ($T(s) = P/I$). The tip is also kept in contact during the whole measurement with the exception of our bias dependent ESR sweeps we present in Chap. 7. We apply an

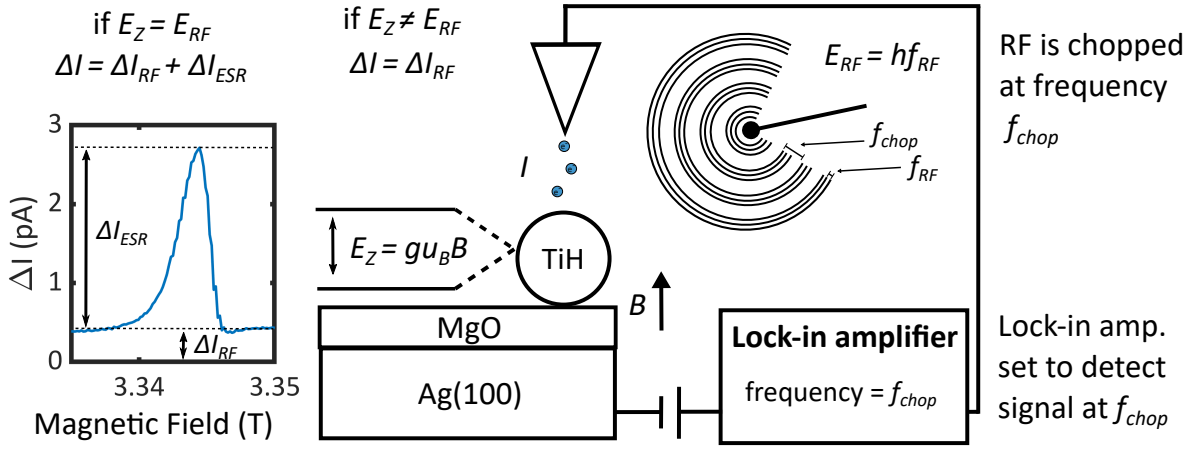

Figure 2.4: Schematic of the ESR signal detection scheme. In the middle we see the STM junction with a TiH molecule on top of the MgO/Ag(100) substrate. The spin states in the TiH can be split with an external magnetic field, B, and the difference in energy between the states is E_Z. On the right we see the RF driving from the antenna and the position of the lock-in amplifier in the circuit. The RF has two frequencies, the frequency of the radiation, f_{RF}, and the frequency at which it is chopped, f_{chop}. The lock-in amplifier is set to detect the change in current at f_{chop}, which is the result of the RF driving that is also set to f_{chop}. The lock-in amplifier here does not modulate the signal itself. On the left of the figure we see data of an ESR signal. When the ZE and RF energy are equal, we get an additional change in the current. When they are not equal we get the baseline change in the current driven by the RF.

external magnetic field to a magnitude where we expect the spin splitting to be close to our target ZE. This splitting is shown in the middle of Fig. 2.4. Next we send RF radiation towards our junction which confines and couples to the tip, driving the spin system at that frequency. We also chop this RF signal at a frequency f_{chop}, which is done to increase the signal to noise ratio. We pick up the resulting RF driving using the internal lock-in amplifier of our Nanonis which is set to pick up a signal at f_{chop} but set to not modulate the signal itself. The internal lock-in then acquires the change in current that is driven by the RF radiation which gives us a resonance signal when the conditions are correct. Off resonance we simply pick up the change in the DOS resulting from the chopped RF radiation. On the right of Fig. 2.4 we see the schematic representation of the RF chopping.

Finally, we can consider what happens when we sweep either the frequency or the magnetic field. As mentioned before, when the ZE and the energy of the radiation match, an additional

signal will appear and our lock-in amplifier picks this up. We start in a regime where the two energies do not match (we are now picking up the base signal with our lock-in amplifier) and we ramp either through magnetic fields or through frequencies. This is done sequentially with atom tracking performed between each data point acquired. We find that either when the RF driving changes or when the magnetic field is swept, the STM will drift from thermal stress that is a result of eddy currents or a change in the radiative heating. The atom tracking between each data point is there to counteract the effect of this drift. Eventually, when the resonance condition is met we measure the ESR signal. This is shown on the left of Fig. 2.4 where there is an ESR magnetic field sweep presented. We usually atom track in between each measurement point for around one second and we tend to acquire data points with 600 ms integration time.

2.3 Experimental Set-Up and Techniques

2.3.1 Laboratory 1E05

The STM we used in our experiments was a commercially manufactured Unisoku USM1300. The machine is kept in the 1E05 lab found in the basement of the Max Planck Institute in Stuttgart, Germany. A picture of our lab and the STM is shown in Fig. 2.5. We are able to bring the STM junction down to temperatures of 320 mK with a single shot He^3 refrigerator. The condensation can last from several days to several hours depending on the amount of microwave heating in the junction. Even when the refrigerator is fully operational we are able to heat the junction above 1 K using our RF radiation, so the change in the hold time of the He^3 can be considerable during ESR experiments. Our STM also has an out of plane magnetic field with a maximum field of 6 T, which we use to facilitate our ESR measurements and spectroscopic experiments on spins. The STM junction is also directly connected to a ultrahigh vacuum (UHV) chamber which allows us to prepare samples and tips in UHV. We assume that the junction is also constantly in UHV with the He^3 pot acting as a cryopump in the junction. In such conditions, we find excellent stability with tips lasting for months before breaking and our current sample staying functional in the junction for over eight months.

We eliminate noise in our experiments in three ways. First, we mechanically isolate the system from the environment putting the STM on a floating table that is on dampers, which is then put on a one-ton block floating foundation that is also on dampers. Both the one-ton

Figure 2.5: Picture of the ESR-STM lab in the Max Planck Institute in Stuttgart. We can see the one-ton block foundation and floating table that help eliminate mechanical vibrations from our system. On the left, we see a rack that contains our RF generator in the rack and our Nanonis on top of the rack. Inside the floating table, we see a green barrel that is the cryostat. On top of the table, we see the preparation and load lock UHV chambers.

block and table can be seen in Fig. 2.5. A tertiary form of mechanical damping is applied directly in the STM junction space where the junction hangs on a set of springs. Second, we eliminate electronic noise by floating all the electronics necessary for measurements with an isolation transformer, and then grounding them to a centralized copper plate on the STM. We then ground the copper plate to the institute ground. In this way we decrease 50 Hz noise in our system. The last procedure we have to follow is to finely adjust the cryostat by putting

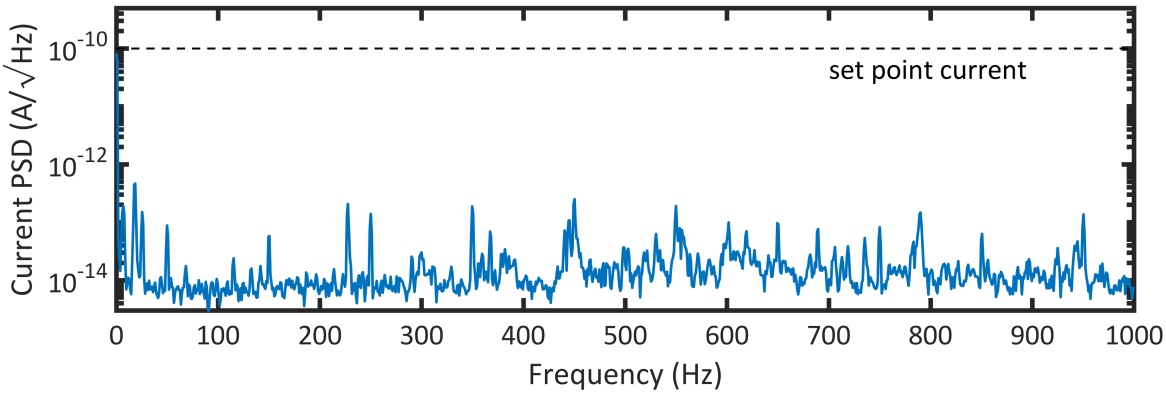

Figure 2.6: Noise spectrum of our STM in quiet measurement mode at $U_{DC} = 100\,\text{mV}$ and $I = 100\,\text{pA}$. We see that all the peaks are well below two orders of magnitude below our set point current.

it in an under pressure of 50 mbar and setting the 1 K pot needle valve to a precise value. If the needle valve is too far open, or without the under pressure in the cryostat, we find strong pinging noise in our current signal. If the needle valve is too far closed we tend to heat up overnight to 20 K, which ruins any samples made for measuring ESR signals. With all the appropriate noise elimination we can get a noise spectrum shown in Fig. 2.6 at a set point current of 100 pA. We see that all the noise peaks are below two orders of magnitude of our current, which is a foundation for quiet experiments.

2.3.2 High Frequency Delivery

To radiate our junction at frequencies from 60 GHz to 90 GHz we had to put great care and thought into designing the delivery system of the HF driving. The signal generation starts outside the STM inlet, as seen in Fig. 2.7, where a frequency generator (FG) starts by sending

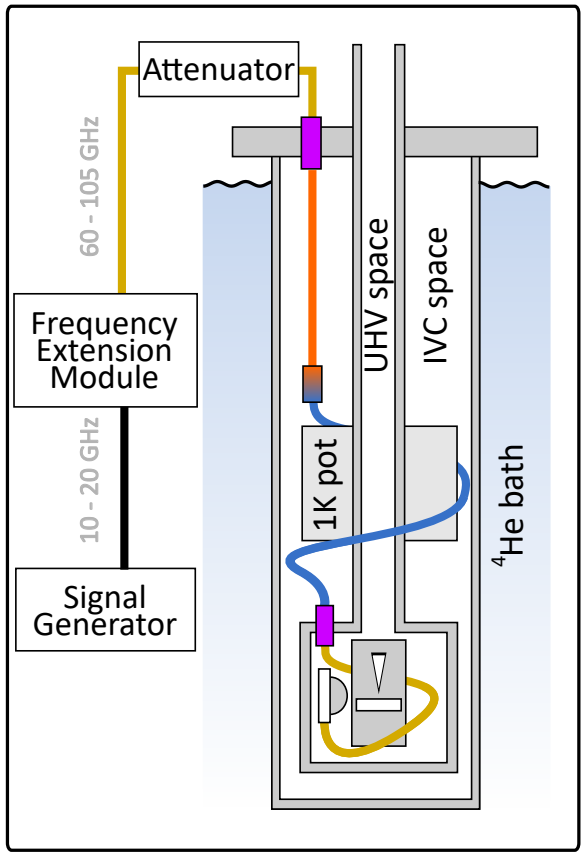

Figure 2.7: Schematic diagram of the STM insert highlighting the HF cabling. Yellow lines are commercial .047 semi-rigid coax cables, orange line is Cu/SPCW .047 cable and blue line is superconducting NBTi .047 cable. Purple blocks represent HF feedthroughs. HF line terminates at the HF antenna that faces the STM junction.

a chosen signal from 10 GHz to 20 GHz. The frequency of this signal is multiplied sixfold before reaching a variable attenuator, which we use to control the amplitude of the radiation hitting our junction. The cabling here is commercially available semi-rigid coax cables, rated to 110 GHz, which terminate at the first feedthrough connecting the inter vacuum chamber (IVC) and the space in the lab. This feedthrough is also commercially available with a rating up to 60 GHz, but as shown by our measurements we still get transmission up to 105 GHz. The cabling after the feedthrough is Cu/SPCW cabling, which then converts to a superconducting NbTi cable at the 1 K pot. We thermalize all the cabling down to the next feedthrough by sequentially connecting the cabling to the baffles in the IVC using Cu wires. This way we guarantee the superconducting cabling is superconducting during operation and this eliminates any attenuation in that line. The next feedthrough is found at the He^3 pot flange that connects the IVC to the STM junction space, and is a vacuum feedthrough made with a NbTi conductor sealed with indium. Finally, flexible semi-rigid coax cable is used again to connect the feedthrough to the antenna. Flexible cable has to be used because our junction is floating on springs and it has to be able to freely move.

For the antenna design we started by considering a bowtie geometry knowing that we sought out a broadband antenna capable of radiating at a range of 30 GHz. We optimized the antenna geometry by simulating the reflection response of the antenna over a range of 0 GHz to 120 GHz. The assumption here is that whatever is not being reflected back by the simulation would be the resulting radiation coming from the antenna. The final geometry and its simulated reflection is shown in Fig. 2.8 b) and c) [61]. Panel a) shows the chip carrier in which we put a silicon chip with our antenna design printed on top. The chip carrier has a silicon lens attached, which helps focus the radiation into the junction, and has a HF connector that we connect to the HF cabling

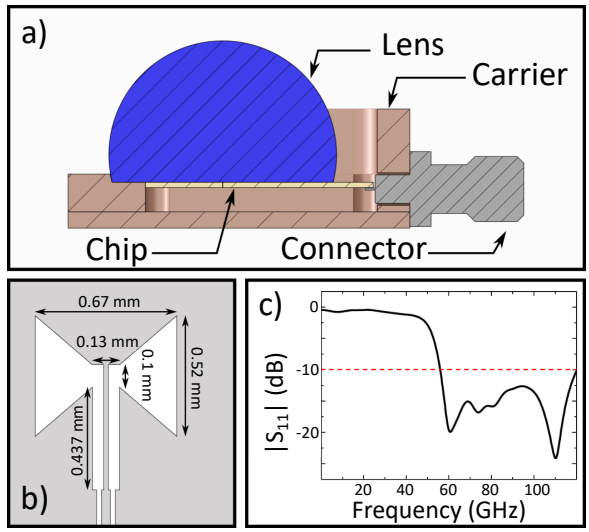

Figure 2.8: a) Schematic diagram of the antenna carrier with the lens and connector labelled. b) Geometry of the HF bowtie antenna. c) Simulated reflection response of the antenna. Shows power dissipation for frequencies above 60 GHz.

shown in Fig. 2.7.

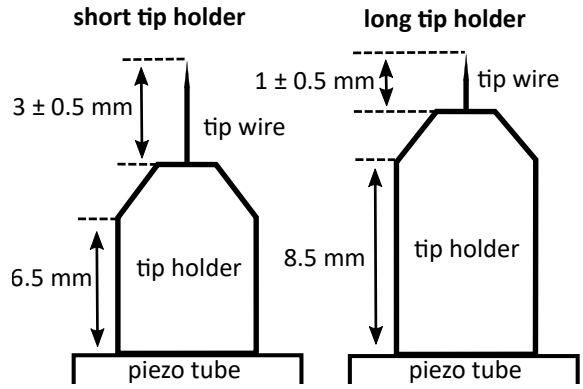

Figure 2.9: Schematic and dimensions of the short and long tip holder. Not to scale.

We would also like to take this opportunity to discuss another component of the STM that we consider to be related to the RF delivery, the tip holders. This is because the efficiency of the coupling from the RF radiation to the tip apex is directly related to the geometry of the tip holder and wire that the RF wave hits. With this in consideration, we asked our STM manufacturer to construct longer tip holders that would have a larger surface area and that would let us choose tip wire lengths designed to be $\Lambda/4$ resonators of our radiation. The geometries of our two tip holders are shown in Fig. 2.9 and their effect on the RF delivery is discussed in detail in Chap. 6. In short, we find that short tip holders with long tip wires give us the best RF driving in our junction, which we believe indicates that increasing the surface area on which the radation can hit the tip wire is the best way to optimize the transfer function.

2.3.3 Low Frequency Driving

With minor adjustments to our instrument we are also able to drive the junction at low frequencies (LF) of 100 kHz to 20 GHz. We do this by sending the RF signal through the same line with which we apply a bias on the STM junction. In practice this involves using a bias tee to combine our DC bias and our RF bias and then applying this combined bias on the tip. Several Unisoku STMs are used in this way around the world to perform ESR-STM experiments [104, 108]. We use the same FG as in our HF set-up, which is limited from 100 kHz to 20 GHz. We use this frequency range for spins whose states we cannot split strongly enough with our magnetic field to be able to probe with our HF regime. Specifically in this dissertation, we use it to measure ESR signals on O-site TiH molecules on MgO. It is important to note, that although the mechanism of the RF coupling to the junction for the HF set-up and LF set-up is different, the effect is the same. In both situations, we produce a bias in the junction at some RF with a defined voltage. In the case of the HF set-up this bias arrives from electromagnetic radiation from the antenna that couples into our tip and tip holder and

then geometrically confines itself onto the tip apex [34]. For the LF set-up the RF driving is an alternating bias that is applied directly on the bias cable.

2.3.4 Tip Shaping and Sample Preparation

In this subsection, we would like to summarize the preparation methods for all the samples and tips used during the experiments presented in this work. The V(100), Pb(111) and Ag(100) were all cleaned in UHV with repeated cycles of Ar^+ ion sputtering at 5 kV and annealing at 1030 K, 470 K and 820 K for V, Pb and Ag respectively. VOPc nanocrystals were deposited for 10 seconds by evaporating VOPcs out of a Knudsen cell heated to 360 K. The sample was cooled to 77 K during deposition and was inserted into the STM immediately after. MgO was grown on Ag(100) by simultaneous thermal evaporation of Mg onto the substrate, heating of the Ag substrate and leaking of O_2 into the UHV chamber. Deposition times ranged from fifteen to twenty minutes with the Mg Knudsen cell being heated to 500 K, the Ag being heated to 520 K and the O_2 being leaked to 10^{-6} mbar. Fe and Ti were deposited using e-beam evaporators by applying an emission voltage of 850 V for both cases and an emission current of 8.5 mA for Fe and 19 mA for Ti. We expect the evaporation temperatures to be approximately 1200 K for Fe and 1500 K for Ti. Deposition of Fe and Ti was done with a sample pre-cooled in the STM junction, which was then taken out for no longer than 40 seconds. Deposition time was between one and two seconds and the sample was cooled back down in the junction in a way as to not heat up above 16 K. Any over excessive heating will cause the Ti and Fe atoms to be mobile on the MgO, which causes them to cluster and ruins the procedure. Ti atoms naturally hydrate during deposition due to the residual H in the UHV chamber. TiH molecules on the MgO surface can be moved using atom manipulation in order to create dimers. They can be dragged under the tip with a constant current set point of $I = 7$ nA and $U_{DC} = 0.35$ V, which is used to move the molecules large distances [114]. Percise movement of a molecule, moving it from binding site to binding site, can be done by moving the tip to the target site, setting the junction resistance to 50 MΩ and then ramping the bias from 1 mV to 300 mV with the feedback loop off.

Tips presented in this thesis where all 0.5 mm in diameter. Both V and Pb tips were made by cutting pure (99.999%) polycrystalline wires, which were then installed into our tip holders and inserted into the STM. Field emission at 100 V and 10 µA was performed on V(100) for V tips and Pb(111) for Pb tips until the tips were stable. Once tips were stable, they would be inserted into the clean substrate by 1 nm to 10 nm to eliminate any Shiba states in the superconducting gap. If we wanted to enlarge the gap we would insert the tip at 10 V into

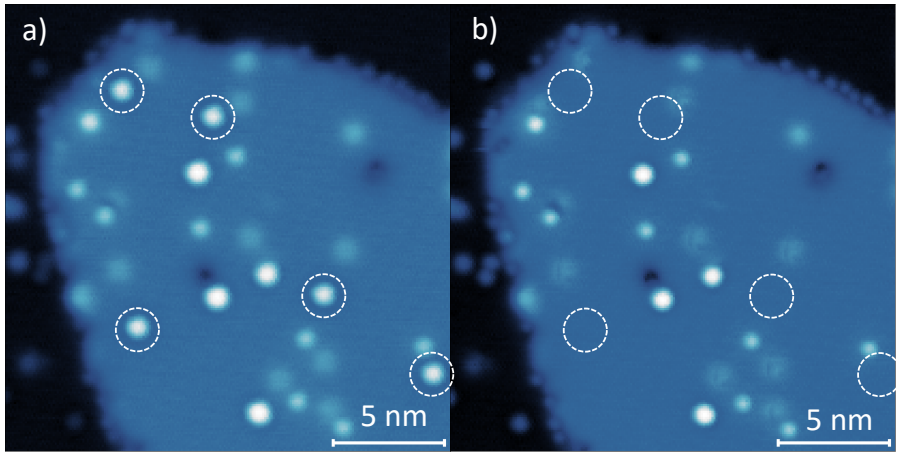

Figure 2.10: Demonstration of picking up Fe atoms for ESR tip creation (U_{DC} = 100 mV, I = 20 pA for both panels). In the left panel we see a scan of MgO/Ag(100) with Fe atoms circled on top of the MgO. On the right, we see the same MgO flake and no Fe atoms indicated by the circles that used to contain Fe atoms.

the substrate by 30 nm and repeat until we got the desired result. In both the case of V and Pb, we were looking for tips that produced large superconducting gaps (approx. 0.8 Δ) with no additional states in or around the gap. For ESR tips we used Pt/Ir tip wires which came with the commercial STM, which were machined by the manufacturer to have a macroscopically conical apex. Tips were inserted into the STM junction and field emission was performed on Ag(100) until the tip was stable (U_{em} = 100 V, I_{em} = 10 µA). We assume at this stage the tip was coated with Ag. Once the tip was stable and we had clean Ag(100), we would grow MgO and deposit Fe and Ti on the substrate. To eliminate any double tips we would insert the tip into clean Ag by 5 nm to 20 nm until the double tip was eliminated. To make a suitable tip for topography we would insert the tip by 1 nm into clean Ag(100) until we could acquire the desired topography. Good topography makes it possible to identify the various molecular and atomic species on the MgO without needing to do spectroscopy. Finally, ESR tips were made by picking up Fe atoms, which was done by lowering the tip by 300 pm and applying -550 mV for one second on top of the Fe atom. This recipe can reproducibly pick up atoms without disturbing any nearby species as seen in Fig. 2.10. More details on finding an ESR sensitive tip are presented in Chap. 6.

3 Theoretical Background

In the majority of this dissertation, we are performing experiments in which we are tunneling through something magnetic, which is obvious due to the nature of ESR, or through a superconducting junction. Therefore, a summary of the various tunneling processes through spins and between SIS junctions is necessary. Furthermore, our machine has an antenna that can apply a microwave voltage in our junction. The effect on the tunneling also has to be understood. Lastly, ESR-STM, which is the basis of this thesis, should be understood on a more fundamental level. This chapter serves as a general overview of these topics.

3.1 Tunneling Between Superconductors

3.1.1 Quasiparticles

In a simple model, the DOS of a SC can be considered to be consisting of two parts, the normal conducting part, where there is enough energy to break the superconducting behaviour by perturbing the electrons, and the superconducting part, which we call the superconducting gap [8, 17]. The Bardeen Cooper Schrieffer theory interprets this by explaining that within the superconducting gap the electrons condense into pairs that are called Cooper pairs (CPs), and this leads to the many properties of SCs. In the low temperature limits of our experiment, the transition from superconducting to normal conducting behaviour is a sharp transition occurring at the gap energy Δ, and results as a sharp peak in the DOS which is called the coherence peak [47, 106]. In the framework of SCs we consider the tunneling that results in these coherence peaks to be quasiparticle tunneling, where quasiparticle states are based on the superposition of the electron and hole states of the broken SC. What this means is that one elementary charge e is transferred during each tunneling event on the coherence peaks, which we will show we can probe with microwave-assisted tunneling. If we want to consider what to expect from STS, our discussion in the previous chapter showed that the measured

signal is based on the convolution of the DOS of the tip and sample. This tells us that in a SIS junction we will measure the convolution of the two superconducting gaps resulting in a gap size of,$e(\Delta_{tip} + \Delta_{sample})$, with coherence peaks positioned at those energies. We can measure this gap without any other states at low conductances, and we compare the size of our observed gaps with literature values to ensure we have good preparations; we know the sample gap should be what is reported in literature, and we optimize the magnitude of our tip gap, which is rarely as large as the sample gap.

3.1.2 Josephson Effect

If we increase the conductance between the two SCs we can get access to a new form of tunneling called the Josephson effect [41, 42]. This effect describes a form of CP tunneling in between the SCs at biases near zero. The Josephson relations that define the resulting current are as follows [9]:

$$I = I_c \sin(\phi), \tag{3.1a}$$

$$\frac{\partial \phi}{\partial t} = \frac{2eU(t)}{\hbar}. \tag{3.1b}$$

What this set of equations states is that if there is a voltage applied in the junction then we drive a changing phase difference between the CP wavefunctions in the two SCs. This phase difference can then result in a current with a maximum possible current of I_c, otherwise called the critical current. At zero bias these equations show that there is a constant phase difference between the two electrodes, which results in a constant current that can take any value between I_c and $-I_c$ depending on the value of the phase difference. If we now apply a fixed bias, the phase will change linearly with time resulting in an AC Josephson effect.

What has been stated in the previous paragraph stipulates a well defined phase in the Josephson junction and this condition is not necessarily met in the case of a STM junction. Due to the ultrasmall size of our STM junctions, the tunneling current is in the dynamical Coloumb regime [4, 39]. What this means is that the particles are sequentially tunneling, their interaction with the enviroment is not negligible and they are phase incoher-

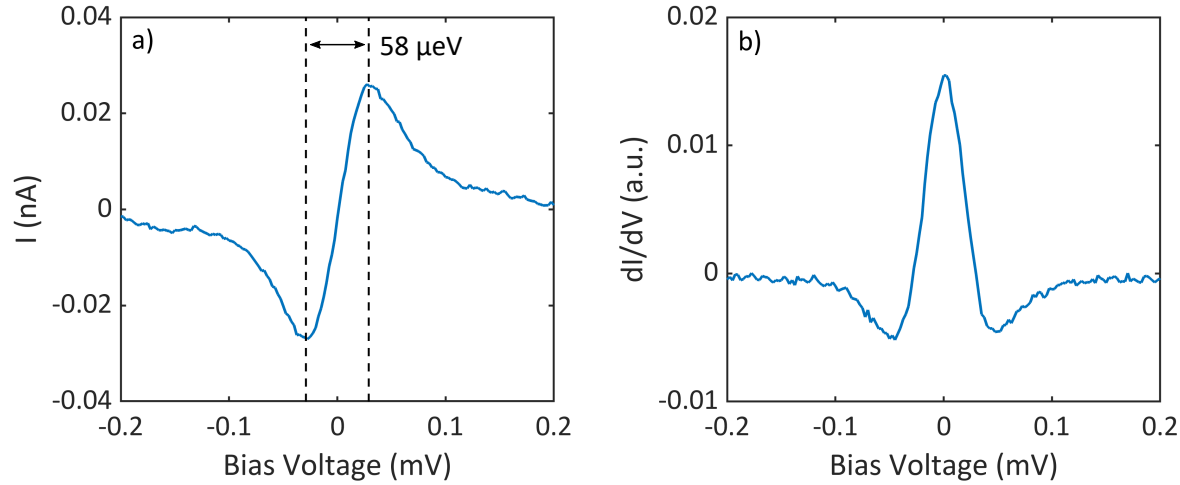

Figure 3.1: a) $I - U$ measurement showing the Josephson effect whose width is 58 µeV ($U_{DC} = 2.5$ mV, $I = 10$ nA). Width is measured as the distance between the current minima and maxima. b) Spectroscopy of the Josephson effect showing the peak at zero bias ($U_{DC} = 2.5$ mV, $I = 10$ nA).

ent. The Josephson current that is measured in STMs can then be defined as the following:

$$I(U) = \frac{4\pi e}{\hbar}(\frac{E_J}{2})^2[P(2eU) - P(-2eU)], \tag{3.2}$$

where E_J is proportional to the critical current. Here the $P(E)$ function defines the broadening of our Josephson effect and is mainly affected by the capacitance in the junction and the temperature. This broadening will also effect the other features in our superconducting gap so we always look to optimize the width of the Josephson effect in our experiments, which is currently around 58 µeV. The width is defined as the distance between the maximum current and mininum current of the Josephson effect as seen in Fig. 3.1 a). In our STS experiments, the Josephson effect is measured as a peak in the conductance at zero bias, as seen in Fig. 3.1 b), and we know that it is a result of two elementary charges tunneling.

3.1.3 Multiple Andreev Reflections

If we increase the conductance even further we can get access to a third type of tunneling called multiple Andreev reflections (MARs) [2, 67]. This is a complex form of tunneling that is the result of the tunneling quasiparticles being reflected back and forth in the junction. At

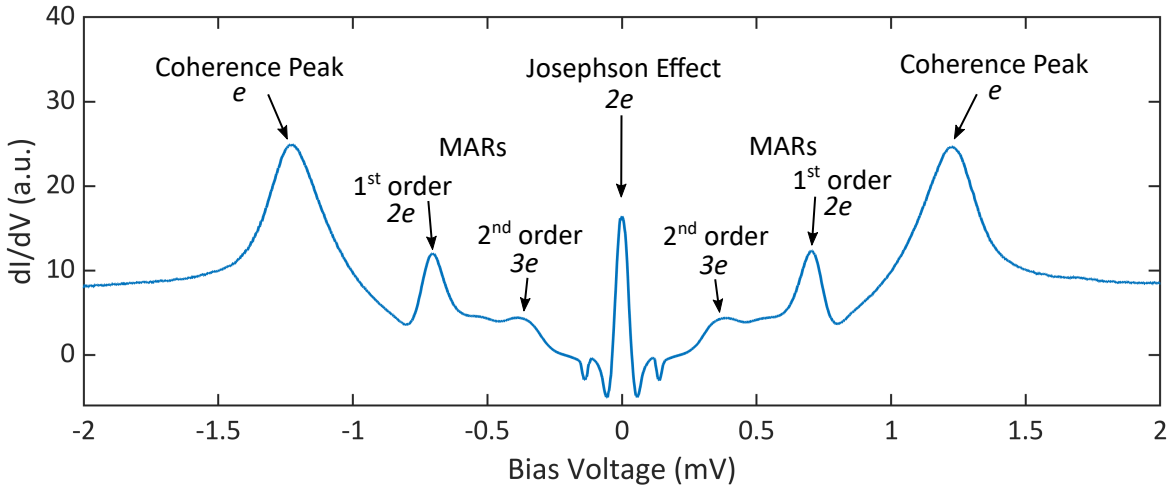

Figure 3.2: STS showing MARs ($U_{DC} = 2.5$ mV, $I = 220$ nA). Each reflection is labelled with its order and charge transfer per tunneling event. Josephson effect and coherence peaks are also labelled with the name and charges trasnferred per event.

each reflection, the particle will return with a charge reversal and to conserve charge a CP has to be injected into the superconducting gap. MARs show up as peaks in our superconducting gap at positions that are related to the number of reflections, or the number of charges transferred [20]. The number of reflections is typically called the order of the MAR, n, and the order will define the charge transferred as $(n+1)e$. Fig. 3.2 shows MARs measured in a SIS junction with each reflection being labelled with its order and charge transfer per tunneling event. Fig. 3.2 also shows and labels the coherence peaks and the Josephson effect along with the charge transferred during their tunneling events. As previously stated, the position of the MARs inside a superconducting gap can be used to determine the charges transferred during that process, but additionally the positions and amplitudes can also be used to study the charge contributions to the tunneling current using full counting statistics (FCS) [22]. In other words, we are able to seperate the different charge contributions to the tunneling current and view them individually. We take advantage of FCS and the amount of charge transfers in first and second order MARs in this dissertation.

3.2 Microwave-Assisted Tunneling

Microwave-assisted tunneling in STMs has been shown to be a useful way to study the properties of tunneling particles specifically by being able to probe their charge [27, 49, 79, 99]. In the simplest case the effect of the microwave on the unperturbed conductance is defined

by the Tien-Gordon (TG) model [99]:

$$G_{RF}(U_{DC}, U_{RF}) = \sum_{n=-\infty}^{\infty} J_n^2(\frac{eU_{RF}}{hf}) G_{DC}(U_{DC} - \frac{nhf}{e}). \tag{3.3}$$

Here U_{DC} and U_{RF} are the bias voltage and the RF voltage, G_{DC} is the unperturbed conductance, e is the elementary charge, f is the frequency of the microwave, h is the Planck's constant and J_n is the n^{th} order Bessel function of the first kind. What this equation describes in the first half is that as you increase U_{RF}, more and more Bessel functions of higher order will become non-zero. The second term then describes that the unperturbed conductance will be shifted by multiples of n, with a spacing related to the microwave energy, hf. These shifted conductances, or replicas as we colloquially call them in this dissertation, will change in amplitude depending on their order, n, as shown in the Bessel function term of the Eq. 3.3. In literature, n is considered to be the photon order but we prefer to use replica order as this effect is not the result of photon-assisted tunneling. We know this by considering the Keldysh parameter, $\gamma \ll 1$, and know that we are in the ionization regime rather than the multiphoton regime [44, 121]. This is due to our relatively low microwave amplitudes, which are 50 mV or less. This detail is discussed more thoroughly in Chap. 4. It is understandable though why this effect might be interpreted as photon-assisted tunneling due to the spacing of the replicas being directly related to hf, which makes it intuitive to assume absorption and emission of photons. To understand why this signature appears in the RF response of spectra, we can consider the voltage driving resulting from the microwave:

$$U(t) = U_{DC} + U_{RF} \sin(\omega t + \pi/2). \tag{3.4}$$

In the case of the Josephson effect we can insert Eq. 3.4 into Eq. 3.1b, integrate over time, and get the following result for the time depedent phase difference:

$$\phi(t) = \phi_0 + \frac{2eU_{DC}}{\hbar} t + \frac{2eU_{RF}}{\hbar\omega} \sin(\omega t). \tag{3.5}$$

Inserting this into Eq. 3.1a can lead to the expression [49]:

$$I_{RF} = I_{DC} \sum_n (-1)^n J_n(\frac{2eU_{RF}}{\hbar\omega}) \sin(\phi_0 + \frac{2eU_{DC}}{\hbar} t - n\omega t), \tag{3.6}$$

which is very similar to the original TG equation (Eq. 3.3). Whenever $2eU_{DC}t/\hbar$ and $n\omega t$ cancel out there is a large DC contribution (these are the famous Shapiro steps), which we call replicas [19, 87]. This previous line of reasoning relies on a on a well defined phase difference between the two electrodes in the junction which is not the case in STMs. As previously mentioned, STM junctions are ultrasmall which puts the tunneling processes in the dynamical Coloumb regime which is characterised by large fluctuations in the phase. Theoretical treatment of the Josephson effect under AC driving and in the dynamical Coloumb regime gives the following:

$$G_{RF}(U_{DC}, U_{RF}) = \sum_{n=-\infty}^{\infty} J_n^2(\frac{2eU_{RF}}{hf}) G_{DC}(U_{DC} - \frac{nhf}{2e}). \tag{3.7}$$

We see that the positions of replicas resulting from this equation are the same as in Eq. 3.6 but the dependency of the replicas on the driving amplitude differs. As our data is replicated by modelling defined by Eq. 3.7b this is a good indication that the tunneling events in our junction are indeed in the dynamical Coloumb regime. Furthermore, Eq. 3.7 now matches Eq. 3.3 almost exactly with one important difference, the charge term in both equations. In the case of the basic TG model, single charge tunneling is modelled. In the case of the Josephson effect, CPs tunnel with a charge of $2e$ so the charge term in Eq. 3.3 is multiplied by two. This is what allows microwave-assisted tunneling to probe the charge of the tunneling particle. Experimentally this is investigated by the spacing of the replicas and their dependency on U_{RF}. Comparing quasiparticle tunneling and CP tunneling, the spacings of the replicas are hf/e and $hf/2e$, respectively, and the dependency on the RF amplitude is twice as quick for CPs as it is for quasiparticles.

3.3 Electron Spin Resonance

3.3.1 Zeeman Splitting

Electron spin resonance relies on the lifting of the degeneracy of states in an unpaired electron via a magnetic field. If we want to understand the perturbation of a magnetic field on an atom we can consider the following Hamiltonian term:

$$H_{mag} = -\tilde{\mu} \cdot \tilde{B}, \tag{3.8}$$

where $\tilde{\mu}$ is the magnetic moment of the atom. If we consider only the electronic part of the magnetic moment we can expand the equation to:

$$H_{mag} = \frac{\mu_B(g_l\tilde{L} + g_s\tilde{S})}{\hbar} \cdot \tilde{B}, \tag{3.9}$$

where μ_B is the Bohr magneton, $\tilde{L}$ and $\tilde{S}$ are the orbital and spin angular momentum operators, and g_l and g_s are their respective gyromagnetic ratios. When the effect of the spin-orbit coupling is small, which is the case for our experiments due to our relatively large external magnetic fields, the energies resulting from this Hamiltonian term are simply:

$$E_{mag} = \mu_B(m_l + g_s m_s)B, \tag{3.10}$$

where m_l and m_s are the magnetic quantum numbers. This effect was first observed experimentally in 1896 by Pieter Zeeman, and we call the difference in energy between two states that are shifted by this effect to be the Zeeman energy (ZE). We also call the splitting of these states the Zeeman splitting. Generally, in ESR we consider the transition $\Delta m_s = 1$, which then leads to our mathematical description of the ZE:

$$E_Z = \Delta E_{mag} = \mu_B g_s \Delta m_s B = \mu_B g_s B. \tag{3.11}$$

The last thing we have to consider for our experiments is that the contribution to the magnetic field comes from two sources, the external magnetic field and the magnetic field that is projected by the Fe atom on the tip. The ZE is then defined as:

$$E_Z = g\mu_B(B_{ext} + B_{tip}). \tag{3.12}$$

Here the subscript on the g-factor is removed for brevity, and for the remainder of the thesis any g-factor that is mentioned is the dimensionless magnetic moment of the spin operator. Eq. 3.12 is a powerful tool for our analysis as it condenses many ESR sweeps into two parameters, the g-factor and the tip field. Here, the g-factor defines how strongly the magnetic field splits the states in the spin system and B_{tip} gives a quantity for the magnitude of the tip magnetic field felt by the spin. Mathematically they are related to the slope and the x-intercept of the linear fit using Eq. 3.12.

3.3.2 Potential Mechanisms for Electron Spin Resonance Scanning Tunneling Microscopy

In bulk ESR, the mechanism that drives the resonance is an absorption of a photon of the correct energy. The energy of this photon, hf, is of course defined by the fundamental Planck's law [73]. When this energy and the ZE match, we can detect less of our input radiation due to the absorption of this radiation and we call this absorption the ESR signal. In the case of ESR-STM the situation is more complicated as we are not in the photoionization regime, which we know from the Keldysh parameter, and we can not consider multiple photons being absorbed. As previously mentioned the Keldysh parameter defines the difference between the photoionization regime and tunnel ionization regime, and will be discussed more thoroughly in the context of our experiment in Chap. 4. This then leads to the question, what is the mechanism behind ESR-STM? Unfortunately, due to the youth of the technique there is no consensus in the community but we have been provided with several interpretations and models [12, 28, 33, 50, 86, 88]. As this thesis is not a theoretical work we do not want to comment too strongly on which model is more or less correct. Here we simply would like to present the different interpretations and their mechanisms along with their merits and setbacks when comparing them with experimental observations. We will be talking about spin-polarized (SP) current in the following discussions which will be more thoroughly introduced in the last subsection of this chapter. For now we should know that a SP current is one whose spin up and down portions are assymetric.

Piezoelectric Coupling of the Adatom to the Radio Frequency

In the very first publication where ESR-STM was demonstrated, the authors postulated that the ESR mechanism might be due to a z-movement of the Fe atom caused by the RF driving. This in turn would cause the Hamiltonian to be time dependant due to oscillating ligand fields [11]. This would then drive transitions between the two lowest energy levels in the Fe atom. This was expanded to a more general case by the authors of Ref. [50] who explain that any periodic change in the Hamiltionian could cause spin transitions. They base this off a Taylor expansion of a general spin Hamiltonian around $z = 0$:

$$H \approx H_0 + z(t)\frac{\partial H}{\partial z}\bigg|_{z=0}. \tag{3.13}$$

Here, H_0 is the time indpendent portion of the Hamiltonian that defines the splitting between the ESR states. When the second term is modulated at a frequency that matches the spin splitting of the first term, transitions between the ESR states are induced.

Now the immediate question is what could possibly create a relevant $\partial H/\partial z$ term. Ref. [50] proposes three possibilities, the exchange coupling between the tip and sample spins, the crystal field term being modulated and the dipole interaction between tip and sample. The first and third possibility are similar in that they are based on the interaction between the magnetic species on the tip and the sample spin, where the first considers the Heisenberg exchange interaction to be dependent on the z-position, $J(z(t))$. The latter is naturally dependent on z as the dipole interaction between two spins is dependent on the distance between them. The second possible way that the Hamiltonian is being modulated is via the crystal field where F denotes the crystal field term and $\partial F/\partial z \neq 0$. In fact this is nearly identical to the mechanism proposed in the original paper but is more general. DFT calculations estimate the crystal field to be modulated by 60 meV/nm in TiH molecules on MgO and our interpretation of our data in Chap. 7 is also based on a non-zero cystal field modulation [28].

The authors of Ref. [50] then explain that this type of driving will result in a population difference between the two spin states, which, as described by the Bloch equations, they define as:

$$P_\uparrow - P_\downarrow = \tanh\left(\frac{\hbar\omega_0}{2k_BT}\right)\left(1 - \frac{\Omega_0^2 T_1 T_2}{1 + (\omega - \omega_0)^2 T_2^2 + \Omega_0^2 T_1 T_2}\right) \tag{3.14}$$

Here, Ω_0 is a measure of the efficiency of the driving force and T_1 and T_2 are the relaxation and coherence times of the spin. This population imbalance can then be picked up by a magnetoresistive mechanism between the spin system and the magnetic tip.

Several forms of criticism are presented for this interpreation in literature. Firstly, the shape of the resonance provided by Eq. 3.14 is symmetric unlike the ESR signals that have been measured in experiment. Secondly, there are groups who claim the estimated driving force is too small [33]. Lastly, there is specific criticism towards the crystal field modulation not being a significant contribution to driving ESR on Fe atoms due to multiplet calculations [83]. Nevertheless, this interpretation also has many qualities that agree with experiment. As mentioned before, we personally observe an effect in this dissertation that we explain with crystal

field modulation. Furthermore, there is recent evidence that a nearby magnetic atom has to be situated near the ESR system for a signal to be measured. This indication was found when performing a remote detection of the ESR signal, where the tip apex is positioned on a different molecule than the one being driven by the RF [71]. What was found is that the signal of the remote species can only be detected when it is near an Fe atom. This finding suggests that either the exchange interaction or the dipole interaction drives the ESR signal. Lastly, the authors in Ref. [50] argue that this model is very general (although other groups argue otherwise). It mainly specifies that the spin system has two energy eigenstates where transitions are allowed. This is in agreement with the different spin species that ESR-STM has been measured on. Also, this model leaves the space for many dependencies of the rate of the spin transitions (otherwise known as the Rabi rate), which is found to be dependent on specific parameters (set point current, bias voltage, RF voltage and tip sample distance), and has been studied in-depth to gain further insight into the ESR-STM mechanism [83].

Modulation of the *g*-Factor

The same group that proposed the piezoelectric driving mechanism in the previous model also gave a complementary mechanism based on a piezoelectric modulation of the *g*-factor [28]. The idea here is that this modulation is different depending on the axis of the modulation and this anisotropy can cause transitions. The authors in Ref. [28] start by defining the Zeeman Hamiltonian and the time dependent perturbation as:

$$H_Z = g_x \mu_B B_x S_x + g_z \mu_B B_z S_z = \mu_B \tilde{b_0} \cdot \tilde{S}, \tag{3.15a}$$

$$U(t) = (\delta g_x \mu_B B_x S_x + \delta g_z \mu_B B_z S_z) \cos(2\pi f t) = \cos(2\pi f t) \mu_B \tilde{b_1} \cdot \tilde{S}, \tag{3.15b}$$

From here it is argued that the perturbation defined in Eq. 3.15b could drive transitions if $|\tilde{b_1} \times \tilde{b_0}| \neq 0$, or in other words if:

$$\frac{\delta g_x}{g_x} \neq \frac{\delta g_z}{g_z}. \tag{3.16}$$

This interpretation has merit to it as it could explain the change in the ESR signal when measured with magnetic fields at different directions, as Eq. 3.16 suggest a strong dependence on the orientation of the system [45]. Furthermore, for the case of TiH on MgO it is very likely that Eq. 3.16 holds true, as $g_x \approx 1.9$ for both binding sites and $g_z \approx 0.6$ for the O-site and $g_z \approx 2$ for the bridge-site [84, 92]. Unless δg_x and δg_z change accordingly, the differences in g_x and g_z will lead to Eq. 3.16 being fulfilled. The main criticism of this model is that it predicts a Rabi rate that changes monotonically with the tip sample distance which contradicts experimental observations [83].

Generalized Open Quantum System

The previous two interpretations looked into the mechanism behing the spin transition driving but did not look in detail on how this transition is picked up with a DC current. Ref. [88] investigates this based on an approach using a generalized open system. They start with the same two level system in a spin center as other groups, and then they show that the polarization of the two levels is predominantly in the z-direction (quantization access of the model). They relate this polarization to the tunneling current and find the following:

$$\langle I \rangle \approx \pi e^2 U T_0 J \rho_s \rho_t p \langle S_p \rangle, \tag{3.17}$$

where U is the bias voltage, T_0 is spin-independent tunneling amplitude, J is the exchange interaction between the spin on the tip and sample, ρ_s and ρ_t are the sample and tip DOS, p is the magnitude of the SP part of the current and $\langle S_p \rangle$ is the average spin in the direction of the tip SP. This shows the contribution to the ESR signal is proportional to the adatom steady-state polarization that is in the same direction as the tip polarization. From here it is argued that the tunneling current is a direct measure of the polarization of the two level system and this polarization only occurs when the system is driven at the correct frequency.

Ref. [88] continues then to explain the source of the assymetry of the ESR signal by considering a more general form of the Bloch equations. They disregard the usual assumption of a non-rotating frame and find that in a rotating frame the decay and excitation of the spin resonance is assymetric leading to an assymetric lineshape of the ESR signal. From here it is shown that this predicts a decay time much larger than the coherence time of the ESR system which is what has been presented in literature. Furthermore, a prediction is made about

how the ESR signal changes when measured at different tip sample distances at high voltages (when the bias voltage is a larger energy than the ZE). We can comment on this last prediction and the assymetry of the ESR signal based off of the results in Chap. 7. What we find is that the ESR signal changes amplitude and shape when changing tip sample distance but it does not follow the behaviour that is predicted in Ref [88]. In fact we see an additional contribution to the signal away from the ESR peak that we believe is related to the RF response of the DOS of the ESR system. We also see a changing assymetry of the ESR signal depending on the set-up of our experiment (LF vs. HF set-up) and a difference between varying TiH binding sites. This is again in contradiction with what is predicted for a generalized open quantum system which predicts a very specific assymetry as defined by the more generalized solution to the Bloch equations. Nevertheless, this interpretation does have its positives as it predicts some assymetry in the ESR signal and predicts the correct ratio between the decay and coherence times found in ESR experiments. This interpretation also has one huge bonus which is not often discussed in literature, and that is that this model shows that the ESR signal is dependent on the direction of the tip polarization. This would be in agreement with tip shaping procedures of ESR-STM tips, as tips are found to be ESR sensitive more rarely than generally. This suggests that the Fe atom on the tip has to be orientated in some specific way for ESR signals to be measured which would be in agreement with the dependency of the ESR signal on the direction of the tip polarization.

Spin-Torque Transfer

The next model eliminates any time dependency in the Hamiltonian by using a time dependent density matrix of the spin system [86]. The interpretation then is that the SP current induces a spin-torque on the system which can drive an ESR signal. The considered Hamiltonian is very similar to other groups, $H = H_S + H_E + H_C$, where H_S is the spin system Hamiltonian, H_E is the environment Hamiltonian and H_C is the coupling of the spin to the environment. H_S is the Zeeman term, $H_S = g\mu_B \tilde{B} \cdot \tilde{S}$, and the coupling term is defined as:

$$H_C = \sum_{a\nu\nu'} \sqrt{J^a_\nu J^a_{\nu'}} S_a \otimes s_a^{\nu\nu'}, \tag{3.18}$$

where $a = 0, x, y, z$ and z is the direction of the tip polarization, $\nu = s, t$ labels the tip and sample leads respectively, J^a_ν and $J^a_{\nu'}$ are exchange interaction terms, S_a is the spin operator of the system and $s_a^{\nu\nu'}$ is related to annihilation and creation operators of electrons in the tip and

sample. To account for the RF driving a costanst shift to the energy of the tip lead is applied with a magnitude that is the amplitude of the driving. From here a master equation is derived using the density matrix of the atomic system and a current is derived by introducing a counting field in the master equation. The resulting current is then:

$$I(t) = -\mathrm{tr}\sum_{aa'}[J_{aa'}(t)\rho(t)S_a + S_a\rho(t)J^{\dagger}_{aa'}(t)], \tag{3.19}$$

where $\rho(t)$ are the density matrices and $J_{aa'}(t)$ is defined as:

$$J_{aa'}(t) = \sum_{\nu\nu' aa'} u^{\nu\nu'}_{aa'}\kappa^{t}_{\nu\nu'}(\omega_\alpha - \omega_{\alpha'}) \times (\delta_{\nu t} - \delta_{\nu' t})|\alpha\rangle\langle\alpha|S_{a'}|\alpha'\rangle\langle\alpha'|. \tag{3.20}$$

Here, $|\alpha\rangle$ are the eigenstates of the spin system with an energy ω_α, and $u^{\nu\nu'}_{aa'}$ and $\kappa^{t}_{\nu\nu'}$ are further defined as:

$$u^{\nu\nu'}_{aa'} = \frac{\sqrt{\Gamma^a_\nu \Gamma^a_{\nu'}\Gamma^{a'}_\nu \Gamma^a_{\nu'}}}{4\pi}\mathrm{tr}[(1 + p_\nu\sigma^z)\sigma^a(1 + p_{\nu'}\sigma^z)\sigma^{a'}], \tag{3.21}$$

$$\kappa^{t}_{\nu\nu'} = \sum_{m=-\infty}^{\infty} i^m e^{im\Omega t}e^{i\frac{\Delta_\nu - \Delta_{\nu'}}{\Omega}\cos(\Omega t)} \times J_m\left(-\frac{\Delta_\nu - \Delta_{\nu'}}{\Omega}\right)\kappa(\omega + m\Omega - \mu_\nu + \mu_{\nu'}). \tag{3.22}$$

Here, the Γs are dimensionless coupling parameters, the ps are the magnitudes of the spin-polarizations of the lead, the σs are spin-½ Pauli matrices, Ω is the frequency of the RF driving, the Δs are the energies of the lead states, the μs are the chemical potentials of the tip and sample and $J_m(x)$ are Bessel functions. Lastly, κ is defined as:

$$\kappa(\omega) = \frac{g(\beta\omega) + if(\beta\omega)}{\beta} - \frac{i}{\pi}\omega\ln\frac{|\omega|}{cW}, \tag{3.23}$$

where c is a constant of order 1, W is the bandwidth of the leads, β is the inverse temperature of the system, $g(x) = x/(e^x - 1)$ and $f(x) = \frac{1}{\pi}P\int dy[g(y) + y\Theta(-y)]/(x - y)$.

The main advantage of this interpretation is how general it is compared to piezoelectric coupling or the g-factor anisotropy, which both rely on the specificity of local environments that could make it difficult to explain the ubiquitous experiments. Furthermore, this model takes

into account the SP tip which is needed for ESR measurements, and it can be used to estimate T_2 times similarily to Eq. 3.14. Ref. [86] also shows an estimated change in the T_2 with respect to temperature which could be measured experimentally and compared to the theory.

On the other hand, there are several misgivings that should be addressed. The predicted signal shape is symmetric so we can make a similar argument as before and therefore state that this model has to be more detailed to explain the observed behaviours. Furthermore, in the spin-torque mediated picture the tip sample distance should have no effect on the ESR signal and the Rabi rate of the system which is in contradiction with experiments [83]. Lastly, this model predicts different behaviours depending on wether the bias voltage is lower, equal to, or above the ZE. For the case of TiH it is difficult to resolve a signal below the ZE but during our experiments we have not observed any significant change where we would have expected one based on the model. We believe for the case when the bias voltage is the same as the ZE we would have observed a slope in the baseline as expected in Ref. [86]. For the case of Fe, and other ESR-STM candidates, we have not found any comparison in literature.

Cotunneling Mechanism

A cotunneling mechanism was proposed in Ref. [33] that considers an oscillating tunnel barrier as the contribution of the RF driving. This is motivated by the argument that the piezoelectric driving mechanism is too specific to account for the ubiquitous nature of ESR-STM spin systems. An oscillating tunnel barrier will affect the hopping amplitudes between tip and sample which results in time dependent off diagonal terms in the two level system that describes the spin:

$$H(t) = \begin{pmatrix} \epsilon_\uparrow & \hbar\Omega\cos(\omega t) \\ \hbar\Omega\cos(\omega t) & \epsilon_\downarrow \end{pmatrix}. \tag{3.24}$$

Here Ω is the Rabi rate and $H(t)$ is effective Hamiltonian as described by the Bloch equations. This leads to the same population imbalance as in Eq. 3.14 (althought the authors of the cotunneling mechanism do not consider the thermal contribution) and it is argued that a magnetoresistive detection mechanism can be used to pick up this population difference similarily to Ref. [50]. The authors also propose a cotunneling mechanism to explain the observed Rabi rates, and decay and coherence times in experiments. The main idea is that the

tunneling through the spin system is in the Coloumb blockade regime where it costs energy to charge the system. This allows the tunneling of the Hamiltonian to be described in charge space which simplifies the calculation.

The resulting Rabi rates for spin-½ systems is found to be system independent which is in agreement with finding similar Rabi rates for different atomic species. Furthermore, by accounting for the orbital degrees of freedom in Fe/MgO, the cotunneling model can also describe the current independent Rabi rates that have been meaured. This model accounts for most of the experimental observations but is difficult to confirm experimentally. The main advantage over other models is its general nature compared to the specific piezoelectric model which needs specific symmetry arguments. On the other hand, ESR-STM has only been measured on MgO so it could be argued that those symmetry arguments are always realistic and perhaps this suggests why ESR-STM has not yet been measured off MgO. Furthermore, the piezoelectric mechanism would explain the need for an additional Fe atom when driving an ESR signal remotely, while the cotunneling model does not predict this need. Lastly, this model has similar shortgivings that other models have in that the detection scheme is simply magnetoresistive, which does not explain the assymetric ESR signals that are measured in experiment.

Disproven Mechanisms

There are also many interpretations of the ESR-STM mechanism that have been disproven experimentally or have been discredited by the community. For the sake of consistency we will also summarize them here. Firstly, spin transitions driven by an alternating magnetic field originating from the RF tunneling current have been estimated to be too small to drive a resonance [84, 112]. Furthermore, the predicted behaviour of the ESR signals with respect to the tip sample distance and driving frequency do not agree with experiment [83]. Secondly, a proposal that interprets the RF SP current creating a field that can facilitate transitions [12]. This interpretation strived to explain why originally ESR signals were measured on integer spins such as in Fe (S = 2), as the spin current does not provide spin angular momentum to drive transitions between states whose spin angular momentums are different such as in Cu (S = 3/2). Lastly, several years prior to the experimental demonstration a proposal was put down of an ESR-STM mechanism based on a change in the DOS caused by the precessing spin in the ESR system [7]. This effect would be able to be picked up with a non-SP tunneling current which is inconsistent with current experiments.

Summary and Outlook

In this subsection we see many interpretations on the ESR-STM mechanism. These interpretations can now be more thoroughly compared to experimental findings. The experimental findings that we would like to compare them to are the following. First, the ESR signal has to be measured with a SP tip which needs some specific yet unknown quality at the tip apex [11]. We know this from the tip shaping we have to perform to make an ESR tip. Second, the ESR signal can only be driven in a system which is near an Fe atom [71]. Third, ESR-STM measurements have all been performed on TiH, Fe, Cu or FePc on multilayer MgO/Ag(100) [11, 111, 115, 119]. Fourth, the ESR signal shape is not consistent between setups, is usually assymetric and there is an off resonance background signal, which we show later in this thesis. Lastly, the Rabi rates have a dependency on the tip sample distance and the RF driving amplitude [83]. This last point has been thoroughly discussed in Ref. [83] and the authors find that spin transitions being mediated by the exchange and/or dipole coupling from the tip being piezoelectrically modulated by the RF driving is the best model to describe their data. This interpretation also explains the measurements in Ref. [71] needing an Fe atom near the remotely driven spin. On the other hand the other models presented in this subsection do not explicitly disclude this neccesity but they do not predict it either. The specificity of the Fe atom on the tip is also not discussed and predicted by every model. In this case only the spin-torque mechanism and the generalized open quantum system predict specific conditions on the SP of the tip. On the other hand, all of the mechanisms are able to explain that ESR signals can be measured on various species on the MgO/Ag(100) substrate. Interestingly, some groups in the community argue that the piezoelectric mechanism is too specific and that a more general model has to be formulated. We find that as ESR-STM has only been measured on MgO/Ag(100) the conditions for a piezoelectric mechanism may hold true. Lastly, the assymetry of the ESR signal is rarely discussed along with the specific shape of the ESR signal. The generalized open quantum system predicts an assymetry based on their modified Bloch equations but they do not match our experimental findings in Chap. 7. We also find few predictions on the RF background signal off resonance that we have measured.

We find that the models in this subsection provide a good start to understanding the ESR mechanism but there are some misgivings that we would like to address and provide as an outlook. Our first point is the lack of specificity on how the current is being affected by the immediate environment and driving mechanism. Most groups interpret a two level system with a population imbalance that is being driven which is in the spirit of the Bloch equations. They then argue that a magnetoresistive mechanism can pick up this population difference.

This explanation does not consider the asymmetric signals that are often measured and the signal that can be measured off the ESR resonace. We speculate that this latter point is a signal derived from the RF driving of the DOS of the molecular/atomic species underneath the tip, but we have not successfully modelled this signal ourselves. Our second piece of outlook is regarding the tip as only two groups mention the polarization of the SP current coming from the tip. As we find that the tip has to have some specific orientation of the Fe atoms on the tip apex, this point should also be looked into more closely. In short, we believe the specificity of the tip, and a pick up mechanism of the current describing the assymetric ESR signals and the off background signal have to included into the models that have been formulated.

3.4 Tunneling Through Spins

3.4.1 Spin Excitation Spectroscopy

If we want to study a spin's physics it is ideal to isolate the spin from the environment. In an STM, this can be done with an addition of a decoupling layer between the spin and the conducting substrate. In practice this decoupling layer is often a thin insulating layer (in all our

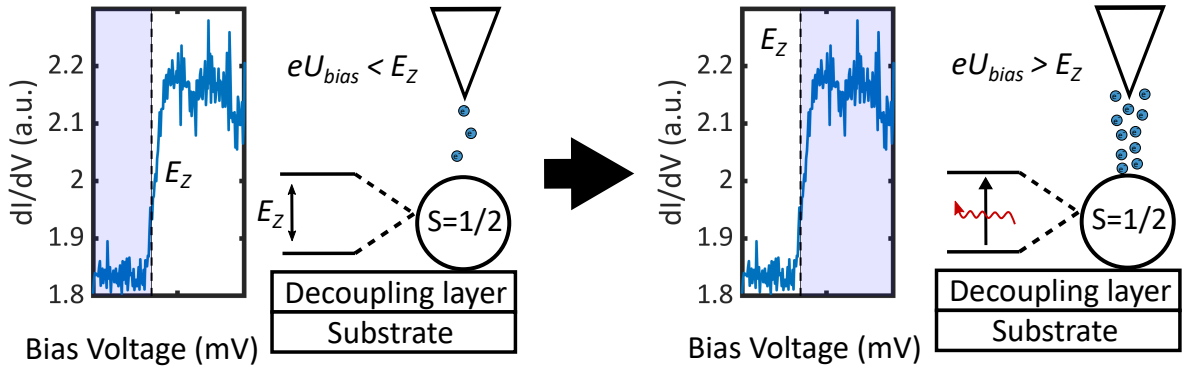

Figure 3.3: Schematic representation of spin excitation spectroscopy. On the left, we have tunneling through a spin-½ in a magnetic field with the bias energy below the ZE. We can measure some base conductance as shown by the data. On the right, we see the inelastic process that occurs when the energy of the electrons is larger than the ZE. In this regime, they can emit a photon to excite the spin and we measure an additional conductance in our experiment. Data is measured on TiH on MgO/Ag(100) ($U_{DC} = 10\,\text{mV}$, $I = 500\,\text{pA}$, $B = 6\,\text{T}$).

cases two ML MgO), which then allows us to consider the tunneling junction as having two potential wells, one from the vacuum in our junction and one from the insulator. The spin sits in between these two wells so apart from tunneling electrons there is no interaction with the tip and substrate. When this condition is achieved we can probe the excitations of spin states in atomic and molecular spins using spin excitation spectroscopy [37]. This is shown in Fig. 3.3 where we show data of a spin excitation measured on TiH on MgO/Ag(100). This is a spin-½ system on which we applied a field of 6 T and measured spectroscopy at a set point of $U_{DC} = 10\,\text{mV}$ and $I = 500\,\text{pA}$. What we see is that if the energy of the tunneling electrons is lower than the ZE then we measure a base conductance with no discernible effect from the spin. When at a bias above the ZE we measure an additional conductance that is a result of the tunneling electrons interacting with the spin. This is a form of IETS as now there is enough energy in the tunneling electrons to excite the spin and emit a photon. This interaction with the spin system leads to an additional channel for the electrons to tunnel through in addition to the normal transmission measured below the ZE. This is represented on the right side of Fig. 3.3 where the split spin states show the emission of a photon (red wavy line) when the spin is excited. We also see additional electrons tunneling resulting from this interaction. It is important to note that for the case of the experiment presented in Fig. 3.3 we are probing an excitation that is made accessible by the Zeeman effect. Spin excitation spectroscopy can be measured for any accessible transition between spin states in an atom/molecule. For example, we measure the spin excitation step in Fe on MgO/Ag(100) throughout this dissertation, and this step can be measured at zero field and is not strongly affected by an out of plane magnetic field. This is an intrinsic property of the system which is explained by the interaction of the Fe atom with the ligand field near its adsorption site [10].

3.4.2 Kondo Effect

When there is no decoupling layer between the spin and the conducting substrate, the spin is screened by the conducting electrons in the substrate and we get the well known Kondo effect [48]. In bulk experiments this is generally indicated by a resistance minimum in temperature dependent experiments where the resistance increases as the temperature approaches 0 K [82]. This is due to a stronger coupling between the impurity spins and the conducting electrons at lower temperatures, which results in larger scattering rates. This in turn is picked up as a decrease in conductance. When the temperature increases the coupling and the scattering weakens, leading to an increase in conductance. Eventually the temperature will rise and we get back phonon-mediated resistance expected for a conducting material. The

characteristic temperature at which the resistance is minimum has been aptly named by the community, the Kondo temperature.

In the case of STM and STS we can locally probe the impurities that cause the Kondo effect. In this case the impurity will give a specific signature called the Kondo peak, dip or resonance at zero bias [14, 74, 97]. This is indicative of the coupling between the spin impurity and the conduction bath. When a magnetic field is applied on this system, we can start to induce a Zeeman splitting in the impurity. In contrast to other types of Zeeman effects we've considered, in this system we have to add enough energy to overcome the coupling of the conduction electrons to the spin. In other words the spin splitting does not start right away at 0 T and only starts at some finite field. We can use this fact to differentiate between a Kondo effect and a free spin with zero field splitting, which we do in Chap. 5. We perform the following analysis. We first measure the spin splitting as a function of magnetic field and then extract the splitting energy with respect to field. We fit a line to the splitting energies, and the intersection of this line will indicate what effect is being measured. If the intersection of the line is through the x-axis then we know we have measured a Kondo effect as the spin splitting starts to occur at some finite magnetic field. If we find that the fit intersects through the y-axis we know that we have measured a free spin with zero field splitting. In other words, we have observed a finite spin splitting at zero field which is exactly the case for Fe on MgO/Ag(100).

3.4.3 Yu-Shiba Rusinov States

We should also consider the case when the magnetic impurity is not on top of a conducting substrate but rather a superconducting substrate. In this case we get the well studied Yu-Shiba Rusinov states which we shorten to Shiba states in this thesis [80, 89, 117]. Here the bath of CPs in the substrate couples to the spin impurity rather than the conducting electrons. At a specific energy, related to the exchange coupling of the spin, the impurity can break a CP and lead to electron or hole tunneling in the superconducting gap. This tunneling will also be dominated by either electrons or holes depending on the specific Coloumb repulsion of the impurity. This will result in the Shiba state to have different transmissions at negative and positive bias. In our STM experiments we measure peaks within the superconducting gap and the position of these peaks will be representative of their Shiba energies. To not confuse them with MARs we always compare the Shiba states at positive and negative bias as they should be asymmetric, due to the Coloumb repulsion of the impurity as mentioned previously, which is not relevant for the case of MARs.

3.5 Tedrow-Meservey Effect

Combining both Zeeman splitting and superconductivity leads to a new effect, the Tedrow-Meservey (TM) effect. The TM effect is what occurs when a SC is put in the presence of a magnetic field that is not strong enough to break superconductivity (i.e. the magnetic field is below the critical field) [62]. In STM tips the critical field can be quite high due to the geometric confinement of the CPs at the tip apex. For a SC to repel a magnetic field that is applied on it (the Meissner effect), the CPs have to create a compensation current at the surface of the SC that counter acts the magnetic field. When the CPs are confined, as is the case in an STP tip, they are unable to create this compensation current as easily and the superconductivity is quenched at a larger field. This small compensation current results in the magnetic field being able to penetrate the SC, which in turn causes the Zeeman effect to take effect. Due to this, the TM effect measured in our experiments exists in our tips while the superconductivity of the sample is fully quenched. When we apply a large enough magnetic field we can quench both the tip and sample. When a magnetic field is applied that does not quench the TM effect, the electrons in the conducting part of the DOS feel the magnetic field and the degeneracy of their spin up and spin down states lifts as explained by the Zeeman effect. This effect is shown in Fig. 3.4 where the blue plot is the TM effect measured on a V tip at a field of 2 T, and the yellow and orange plots represent the spin up and spin down DOS of the tip shifted in energy by the magnetic field. The combination of these two DOS makes up the DOS measured by the experiment. One more effect is implied by this representation; there are bias ranges where the spin up DOS is larger than the spin down and vice versa. When there is an asymmetry between spin up electrons and spin down electrons in a current, we call this a spin-polarized (SP)

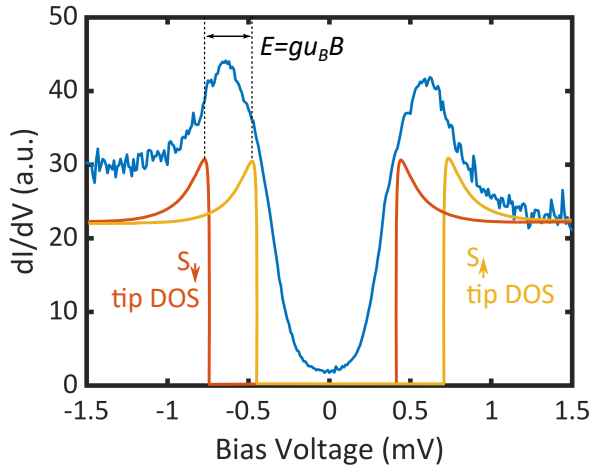

Figure 3.4: The TM effect measured on a V tip shown in blue, and the representations of the spin up and spin down DOS (in yellow and orange respectively) split by the magnetic field. Distance of splitting is the ZE. Data was measured at $U_{DC} = 2{,}5\,\text{mV}$, $I = 8\,\text{nA}$ and $B = 2\,\text{T}$.

current. In the case of tunneling we call this SP tunneling [64].

3.5.1 Spin-Polarized Tunneling

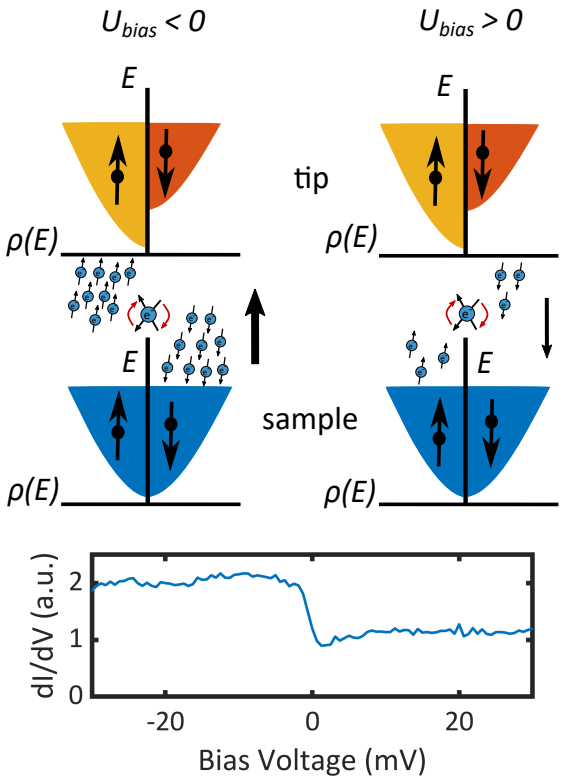

Figure 3.5: Schematic representation of SP tunneling and a SP signature measured in experiment. Schematic shows that tunneling from a non SP DOS to a SP DOS will result in more current than the reverse. Data is measured with a SP tip made by picking up Fe atoms. Measured with a SP tip on TiH on MgO/Ag(100) at $U_{DC} = 100\,\text{mV}$ and $I = 500\,\text{pA}$.

SP tunneling, as previously mentioned, is the resulting tunneling from a DOS whose spin up and spin down components are asymmetric. SP-STM is a very powerful experimental technique that can be used to understand nanoscopic magnetic phenomena from skyrmions to magnetic domains [77, 107]. On a fundamental level what this type of tunneling does is it provides us contrast between spin behaviours on the sample which otherwise would not be picked up with a normal conducting current. This contrast is a result of the alignment or antialignment of the tunneling electrons with the spin of the substrate. If the two spins align then we get a larger current than when the two spins do not align. In our ESR-STM experiments we have to use a SP current to pick up the difference between a driven state (whose population is 50/50 spin up and down) to one which is not driven (fully spin down if at base temperature), which would not be accessible with a normal current. We make SP tips by picking up Fe atoms as shown in the previous chapter.

Fig. 3.5 shows the signature we use to identify a SP tip and the physics behind this signature. On the bottom we see experimental data of a TiH molecule on MgO/Ag(100) measured with

a SP tip. We see a step at zero bias, which is our indication of spin-polarization. We can understand this by considering the schematic at the top. Here we see the case for tunneling that has to switch alignment from tip to sample and vice versa. The contribution to the tunneling where the spins do not have to change alignment is the same for both negative and positive bias. When we tunnel from the sample to the tip, which in the case shown on the left of Fig. 3.5, there are many states for spin down electrons from the sample to align into by flipping spins. When the bias is reversed this current is lessened, as there are not so many spin down electrons that can come from the small DOS of the tip. In practice, the size of the step at zero bias is also an indication of the strength of spin-polarization or the size of the asymmetry between the spin up and spin down DOS.

4 Microwave-Assisted Tunneling in Superconducting Junctions[1]

Tunneling spectroscopy performed between superconductors provides a plethora of processes that can be studied, especially with the assistance of microwave driving [15, 27, 79, 87, 99]. Importantly, the amount of charges transferred in a tunneling event can be probed with microwave-assisted tunneling [79]. Coherence peaks, which are a characteristic signature found when tunneling between two SCs, are a particularly sharp and large state in the DOS, which makes them an excellent candidate to measure the amplitude and frequency of a RF signal sent into the junction. Therefore, the coherence peaks could be used to measure the transfer function of our RF cabling and antenna. With the intention to measure a transfer function and to study microwave-assisted tunneling, we prepared a SIS junction consisting of a V(100) crystal sample and a polycrystalline V tip. A constant current scan on this system can be seen Fig. 4.1 a) showing square terraces expected for a V(100) surface. All measurements were performed on flat parts of terraces, and off terrace edges and impurities.

4.1 Tien-Gordon Effect on Coherence Peaks

Fig. 4.1 b) shows a typical spectrum measured on our sample system showing the superconducting gap expected for a SIS junction along with the RF response of this gap at two amplitudes [4, 38]. We see that the magnitude of the gap corresponds to what would be expected for such a junction ($\Delta_V = 0.76\,\mathrm{meV}$ [46]). When applying microwave radiation, the coherence peaks of this gap "replicate" besides the original coherence peak with a spacing related to the radiation energy, hf/e. This is shown with dashed white lines in Fig. 4.1 c). Intuitively one could assume that this is a photon-assisted process where the photons from the radiation are absorbed and emitted by the junction and therefore the DOS results in these

[1] This chapter is based on publication #4 on the publication list

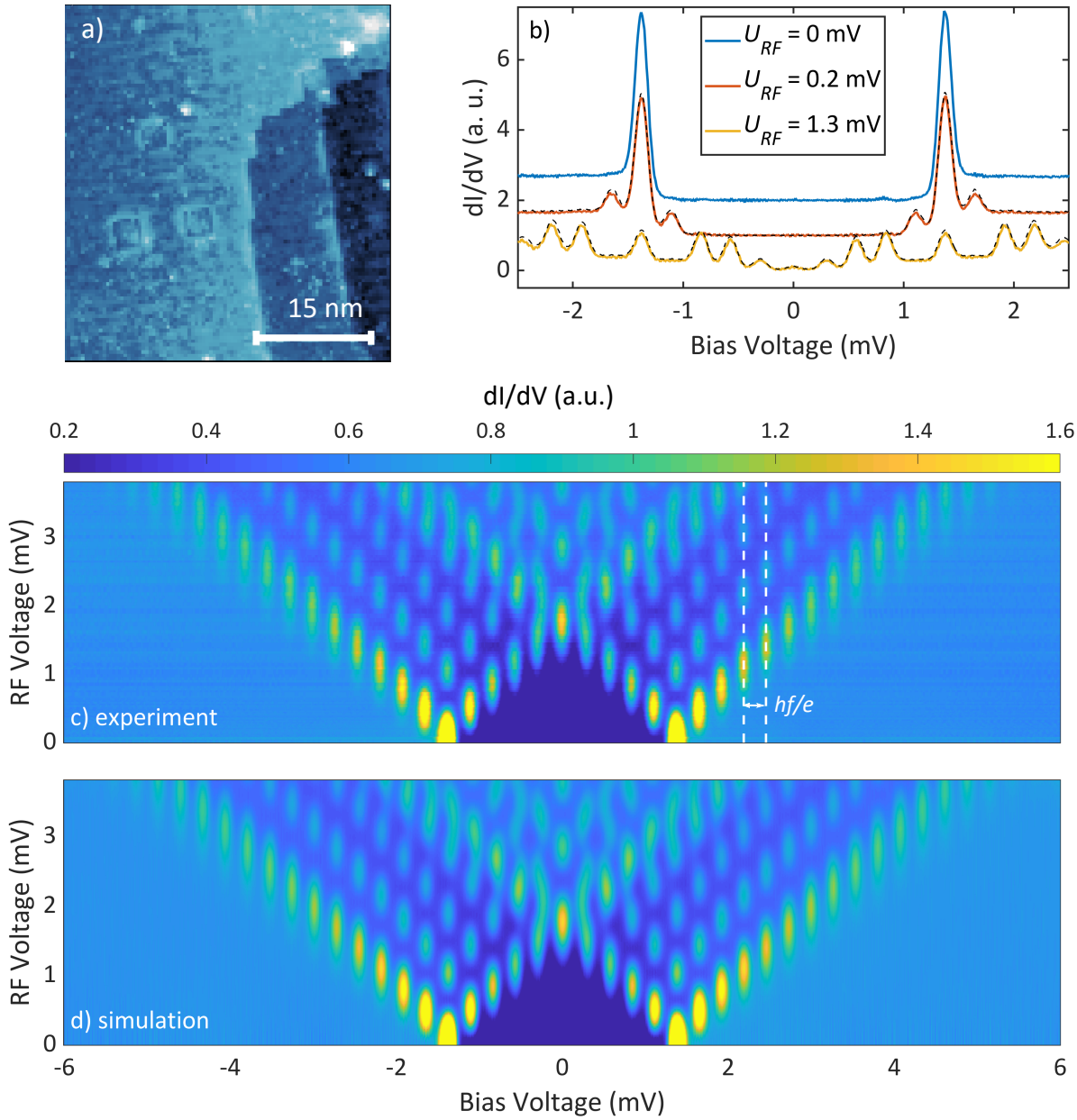

Figure 4.1: a) Topography of the V(100) surface ($U_{DC} = 100$ mV, $I = 100$ pA). b) Spectroscopy of the superconducting gap along with the RF response at two amplitudes ($U_{DC} = 10$ mV, $I = 65$ pA, $f = 65$ GHz). Data is offset for clarity. c) Spectra of the RF response of the superconducting at varying RF amplitudes ($U_{DC} = 10$ mV, $I = 65$ pA, $f = 65$ GHz). White dashed lines show the spacing of the replicas, $\Delta U_{DC} = hf/e$. d) Simulation of the RF response of the superconducting gap based on the TG model.

shifted replicas. However, if one considers the Keldysh parameter, which our case $\gamma \ll 1$, we can see that in our case the radiation power is far too small for more than one photon to arrive at the junction, therefore making this a microwave-assisted process [44, 121]. The Keldysh parameter, γ, defines two photoionization regimes, the multiphoton and the tunneling regimes. When $\gamma \gg 1$, which occurs when the amplitude of the radiation is large enough, photon-assisted tunneling can be observed where photons can emit and/or absorb packets of energy. In our case the Keldysh parameter is relatively small due to our low RF amplitudes, which puts our experiment in the tunneling ionization regime. This leads to the processes in our tunneling junction to be driven by the microwave field rather than individual photons.

4.1.1 Transfer Function Measurement

We can use the replicas shown in Fig. 4.1 b) to measure the power of the radiation that is coupling to the tip. This is done using the TG model, which describes that the amplitude of the replicas and the amount of replicas will change depending on the radiation amplitude. To demonstrate this, a full continuous range of spectra at different radiation voltages were measured and are shown in Fig. 4.1 c). Fig. 4.1 d) are the simulated spectra which are made by applying the TG model onto the spectrum at $U_{RF} = 0\,\text{mV}$. Comparing the two panels we see a remarkable resemblance. Due to the fact that each unique RF amplitude will result in a unique spectrum, we can calculate the power arriving at the junction based solely on a spectrum. Along with the power applied at the source, we can calculate the transmission of the cabling and antenna at any given frequency. Repeating this over many frequencies gives us a transfer function. For more details please refer to Subsec. 2.2.1 in Chap. 3 of this dissertation.

4.1.2 The High Amplitude Limit

It is interesting to note that the TG model gives a description past $eU_{RF} > 2\Delta$, which in our case is around 3.2 meV. Specifically, the model posits that replicas can continue to appear far above the energy of the superconducting gap. We wanted to test the limit of this model by applying highly intense RF radiation, at $f = 70.02\,\text{GHz}$ and $U_{RF} = 13.62\,\text{mV}$. Fig. 4.2 shows the resulting data with the TG response and fit scaled up to the normal SC gap. We can see that the TG model still works well to fit the data and most of the deviations can likely be

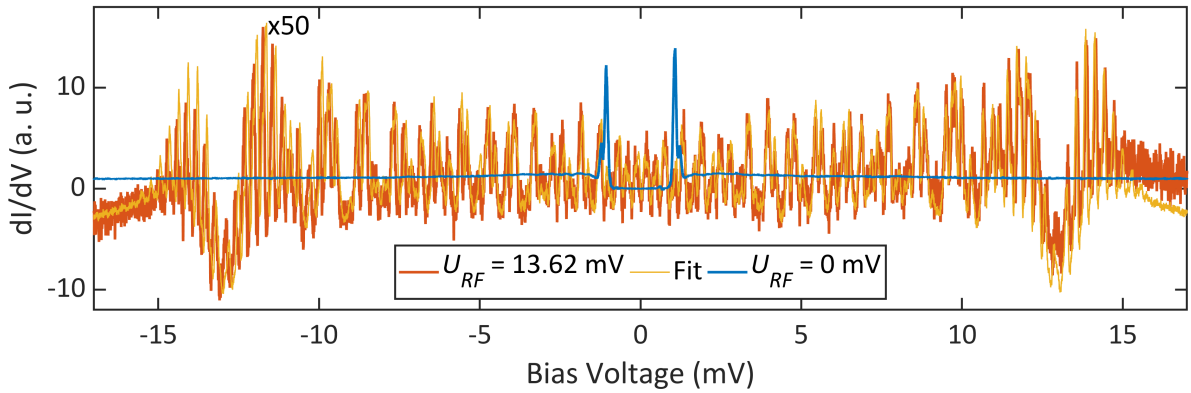

Figure 4.2: RF response of the superconducting gap under high power radiation along with the normal gap and the fit ($U_{DC} = 17.5$ mV, $I = 8$ nA, $f = 70.02$ GHz). Fit and RF response are enlarged fifty times for easier comparison with the SC gap.

accounted to STM drift. This data suggests that the SC is not strongly affected by the microwave radiation. The junction is heated up to 1.1 K during the measurement with the RF applied, while the measurement without the RF was performed at a base temperature of 320 mK. As the TG modelling, which is done with the reference measured at 320 mK, shows good agreement with the measured data at 1.1 K, we surmise that the SC is transparent to the microwave radiation and does not heat up strongly. That is to say, an increase in temperature of the SC would broaden the coherence peaks significantly enough for the model to not replicate the data due to having an incorrect low temperature reference. As we do not observe this, we conclude that thermal broadening does not affect our SC during this measurement.

4.2 Interference Effects between Tunneling Processes

4.2.1 Tien-Gordon Effect on the Josephson Effect

$$G_{RF}(U_{DC}, U_{RF}) = \sum_{n=-\infty}^{\infty} J_n^2\left(\frac{2eU_{RF}}{hf}\right) G_{DC}\left(U_{DC} - \frac{nhf}{2e}\right) \tag{4.1}$$

In the previous section we saw how the microwave response of coherence peaks can be modelled using the TG theory. In the case of coherence peaks an individual tunneling process has one charge transferring from one side of the junction to the other. This is important as the charge is considered in the TG model, specifically in the numerator of the Bessel function

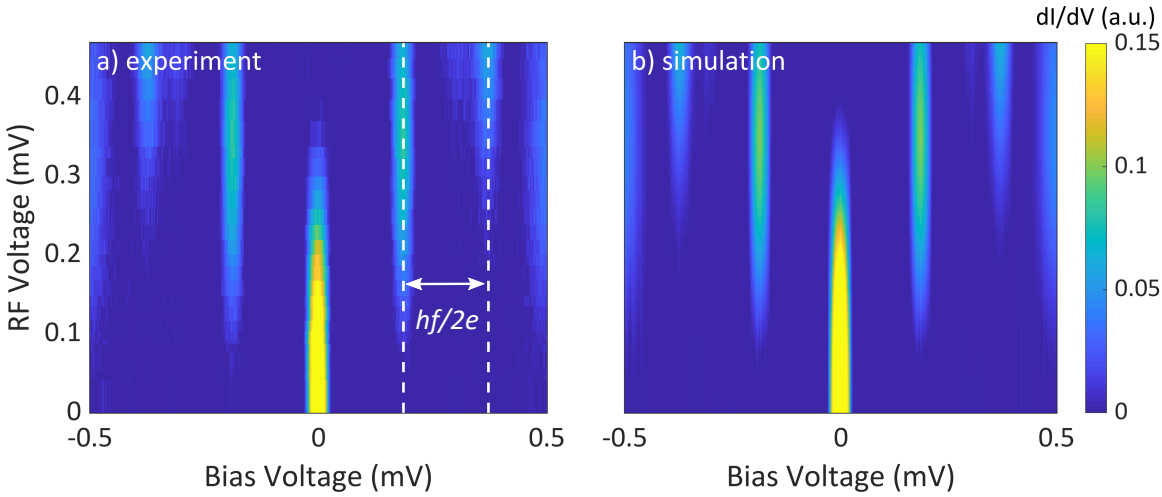

Figure 4.3: a) RF response of the Josephson effect at varying RF amplitudes ($U_{DC} = 2.5$ mV, $I = 1$ nA, $f = 90$ GHz). White dashed lines show spacing of the replicas, $\Delta U_{DC} = hf/2e$. b) Simulation of the RF response of the Josephson effect based on the TG model.

term and in the term that defines the energy shift of the "replicas". A doubling of the tunneling charge can in principle be modelled by changing these two terms and redefining the TG equation to Eq. 4.1. This can be confirmed experimentally by measuring the RF response of a higher charge tunneling process, namely Josephson tunneling. As previously discussed in Chap. 3, the Josephson effect is the result of CPs tunneling which means there are two charges transferring during each tunneling event. Fig. 4.3 shows the experimentally measured RF response of the Josephson effect in panel a), along with the modelled response in panel b). We can see that the model and experiment match remarkably well. Furthermore, the spacing of the replicas in Fig. 4.3 is half to that of the replicas in Fig. 4.1 b-d) (this will become more clearly presented in Fig. 4.4). This is indicative of the different amount of charges tunneling in the Josephson effect versus the coherence peaks.

4.2.2 Tien-Gordon Effect on Multiple Andreev Reflections

We continued studying the effect of charges on microwave-assisted tunneling by also considering MARs, which are tunneling processes that transfer two charges or more. Specifically, we studied a junction that showed MARs with two and three charge transfer processes. Fig. 4.4 shows the experimental data with and without RF driving. The positions of the tunneling processes are labelled with dashed lines and the replicas of these processes are labelled with solid lines. Similarily to the comparison between Fig. 4.1 and Fig. 4.3, we see that the energy

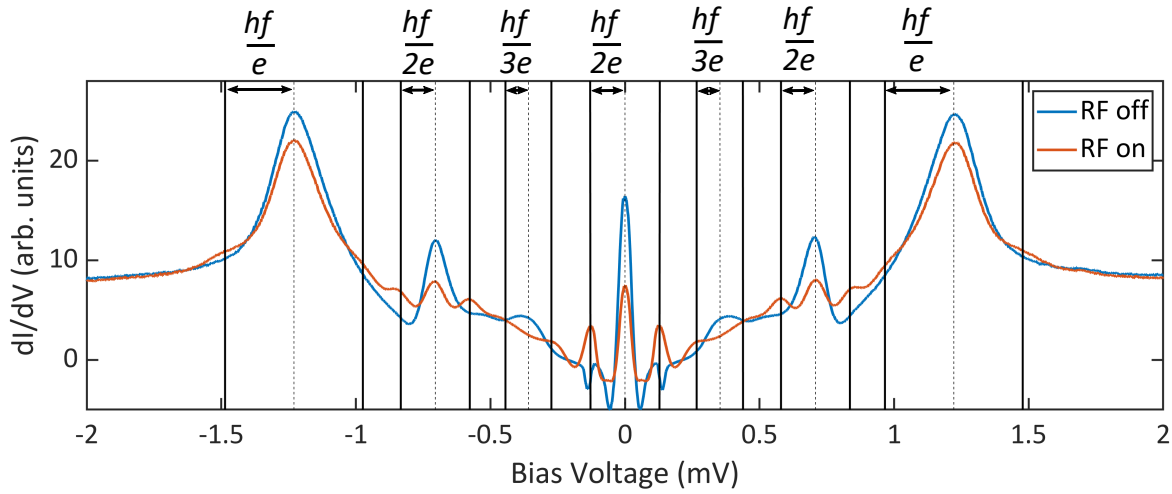

Figure 4.4: RF response of the superconducting gap at a high conductance ($U_{DC} = 2.5\,\text{mV}$, $I = 220\,\text{nA}$, $f = 60\,\text{GHz}$). Positions of various tunneling processes are shown using dashed lines. Positions of their replicas are shown using solid lines.

shifts of the tunneling process replicas depend on the charge of the process. In other words, we see a shift of hf/e on the coherence peaks, a shift of $hf/2e$ on the first order MAR and the Josephson effect, and a shift of $hf/3e$ on the second order MAR. If we take a closer look at the three charge process we can see that the replicas form in some way but there is an indication that they deviate from the TG model based on their width and amplitudes. We wanted to investigate this further and have done so by modelling the microwave response of MARs with FCS.

Modelling Microwave-Assisted Tunneling in MARs

Looking at the previous data sets, one could conclude that the current is carried by individual tunneling processes and the RF response can simply be modelled by considering the charge of the separated processes and then adjusting Eq. 4.1 accordingly. In fact this interpretation can be found in literature [79]. One can test this interpretation by dissecting MARs which naturally consist of various higher order charge processes.

There are potentially two ways to model and interpret the RF response of MARs. The first is by adjusting the tunneling Hamiltonian of the system so that the driving voltage is oscillatory and then calculating the conductance based on the new Hamiltonian. This modelling philosophy considers all various tunneling process to be interfering and inseparable. This is the approach proposed in Ref. [19] and will be referred to as the full MAR model in the following

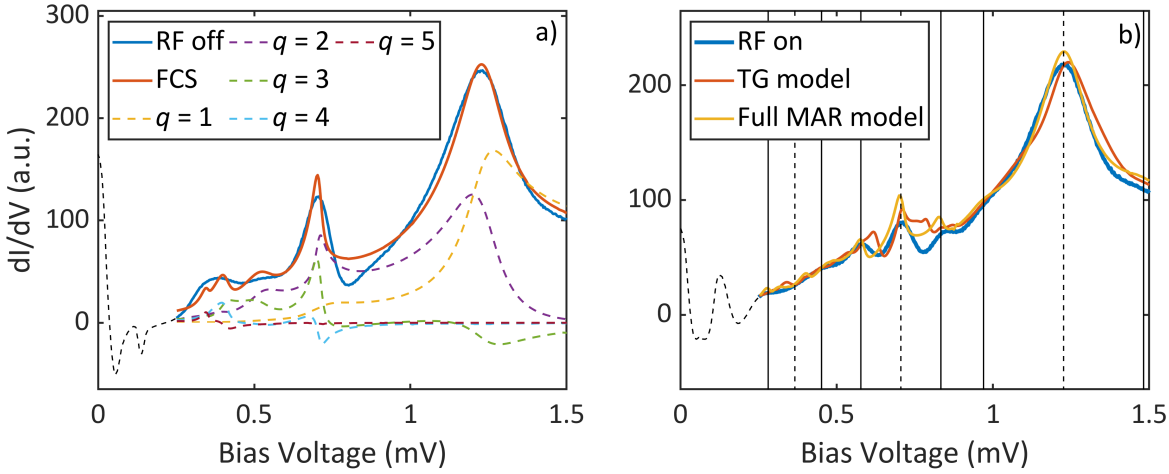

Figure 4.5: a) Experimental data along with the FCS (solid lines) and the different charge contributions (dashed lines) ($U_{DC} = 2.5$ mV, $I = 220$ nA, $f = 60$ GHz). b) Comparison of the data to the TG model and the phase model. Dashed lines show the positions of the varying tunneling processes and the solid lines label the expected positions of the replicas.

discussion. The second possibility is by separating the various charge contributions in our superconducting spectrum and applying the TG theory on each charge contribution individually. One can separate the various charge contributions in the superconducting gap by first analyzing the subgap features and using standard MAR theory and fitting routines [5, 20, 21, 85]. We find that our junction consists of five transmission channels with conductances defined by τi = [0.416, 0.293, 0.115, 0.114, 0.112] [49]. After this step one can calculate the FCS of the channel and find the contribution to the current from each charge process (this calculation was done with the support of our theory collaborators). Fig. 4.5 a) shows the data along with the FCS and the contribution of each charge. Finally, the TG model can be applied individually on each charge process and then compared with the original data and the full MAR model, as shown in Fig. 4.5 b). We see that modelling the RF response by adjusting the driving in the tunneling Halmiltonian, as suggested in Ref. [19], gives a closer agreement to the data than applying the adjusted TG theory on each charge contribution.

4.2.3 Conclusions

Considering the relative good agreement between the full MAR model and the data, and the poor agreement between the TG model and the data, we conclude that the full interpretation has to consider the interference between various tunneling processes to fully describe

the RF response. Ultimately, the difference between the TG ansatz and the full MAR model is how the DC transport interacts with the microwave signal. Both models show that when a particle tunnels through the junction, the particle will either absorb or emit integer multiples of the microwave energy. The TG interpretation posits that the particle will tunnel and then in a separated incidence either emit or absorb the right energy. At low conductances, specifically in the tunneling regime, this interpretation is sufficient and the TG model works well in describing the experimental results as we see in Fig. 4.1 and Fig. 4.3. On the other hand, at higher conductances the quasiparticles tunneling in the junction can be reflected between the electrodes several times before the tunneling process is complete. Therefore, there are many opportunities for the tunneling electrons to interact with the microwave and that is when the TG interpretation starts to fail. In this case, the full model is a more detailed interpretation that can consider MARs, and therefore the interaction of the microwave with the quasiparticles bouncing around in the tunnel junction.

4.3 Multiple Cooper Pair Tunneling

4.3.1 Observation of a Potential Two Cooper Pair Tunneling Process

As it is necessary to go to relatively high conductances to be able to resolve MARs, we also had the opportunity to measure the RF driving of the Josephson effect at high conductances. We found that there is another peak in between the original Josephson peak and its first replica (Fig. 4.6 a)). This additional and unexpected peak should be characteristic of a tunneling process with four charges or two CPs. This would of course be very exciting as multi-CP tunneling has not been directly observed before, and it would also open a way to study the energy-phase relations of tunneling electrons using only one junction [85]. We measured spectra at varying RF amplitudes to see if this peak would follow the TG description (Fig. 4.6 b)). We see that the peak seems to appear and dissapear at around the correct RF voltages and the position of the peak is around the correct bias position. One immediate deviation from what we expect is that this peak does not stay exactly at the same position when we vary the RF voltage. As this could arise from the relative intensity of the zeroth and first order replica interfering with this peak, we continued to investigate this effect at other frequencies.

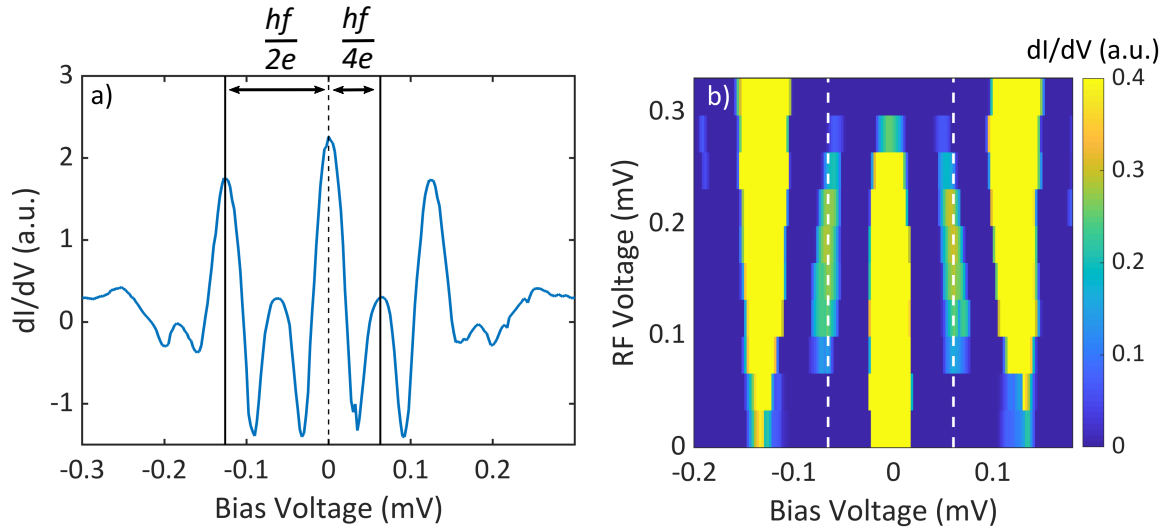

Figure 4.6: a) Spectroscopy of the Josephson effect under radiation of $U_{RF} = 0.13$ mV ($U_{DC} = 2.5$ mV, $I = 220$ nA). Positions of a two charge tunneling process replica and a four charge tunneling process replica are marked with a black line. b) Spectra of the Josephson effect under radiation of varying voltages ($U_{DC} = 2.5$ mV, $I = 220$ nA). White dashed line shows were we would expect replica of a two CP tunneling process.

Unfortunately, we immediately find a deviation from the hypothesis when measuring this effect at varying frequencies (Fig. 4.7 a)). The dashed black lines show the positions of where we would expect a two CP replica, and we can see the replica of what was thought to be the two CP tunneling process only appears at $f = 60$ GHz. This dissproves the notion that the additional peak measured in Fig. 4.6 a) is the result of a multi-CP process. If this additional peak is not a result of a multi-CP tunneling process, then the question arises where might this peak come from. Although we only speculate, we think it has to do with irregularities in the Josephson effect. This irregular Josephson effect is shown in Fig. 4.7 b) and has been observed in other systems but not consistently in each set-up [95]. We can see that at $I = 150$ nA and 200 nA that there is an additional signal left and right of the Josephson peak. This additional signal seems to disappear as a sharp step, at around $U_{DC} = 0.12$ mV for the 150 nA data and around $U_{DC} = 0.18$ mV for the 200 nA data as indicated by the black arrows in Fig.4.7 b). This additional current under external driving may create this additional peak which we misinterpreted as a multi-CP process.

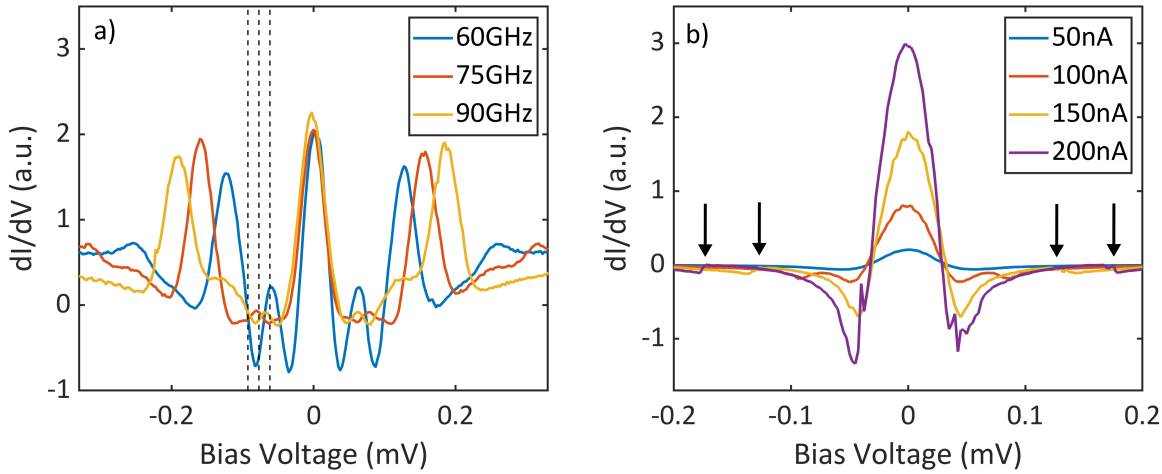

Figure 4.7: a) Spectroscopy of Josephson effect under RF radiation ($U_{DC} = 2.5\,\text{mV}$, $I = 220\,\text{nA}$). RF amplitude chosen so that we would expect to see two CP tunneling ($U_{RF} \approx .13\,\text{mV}$). Dashed lines show were we would expect the two CP tunneling for $f = 60\,\text{GHz}$, 75 GHz and 90 GHz. b) Spectra of the Josephson effect measured at different currents ($U_{DC} = 2.5\,\text{mV}$). The larger the current the more irregular the Josephson effect becomes. Black arrows indicate unexpected steps in the conductance.

4.4 Outlook

The results in this chapter provide a good start in the study of microwave-assisted tunneling in STMs, but there are still many interesting projects that were either briefly mentioned or not mentioned in this chapter. Firstly, the breaking of the superconducting gap with the use of microwave radiation could be attempted if $hf \geq 2\Delta$. In fact, a good candidate would be an Al-Al junction as $2\Delta_{Al}$ would be around 0.36 meV [46]. From there one could also perform pump-probe experiments to measure the lifetime of the superconducting states and one could also measure the transition between a TG response and microwave breaking of the superconducting gap. Secondly, the idea to observe multi-CP tunneling could be reviewed and attempted again. Namely, this tunneling process could be more evident on a Shiba state or in a different superconducting material, and therefore, the experiments performed in the previous section should be repeated either on Shiba states or in another superconducting junction. Lastly, Shiba states themselves could be of interest to study under microwave driving [70]. In fact with our high radiation energy we could even match the energy of a Shiba state. This could in principle excite the Shiba state and the resulting experiment would deviate from the TG model. In fact, these ideas are so promising that a machine has been developed at the Max

Planck Institute in Stuttgart that will focus on these projects.

5 VOPcs on Pb(111) as a Potential System for Single Molecule Electron Spin Resonance

There are two components that a sample system has to provide for the realization of an ESR-STM experiment. First, there has to be a decoupled spin system that has a Zeeman splitting in an energy range corresponding to the driving frequency. Second, there has to be way to form a SP current. Phthalocyanines with a spin center on a superconducting substrate should provide both necessities. The first criterion is satisfied as phthalocyanines lying on a substrate are naturally decoupled [31, 54, 90, 105]. Specifically, VOPc (Fig. 5.1) is a good candidate for our system as it has been observed to be a spin-½ system in recent years [58]. The second criterion can be satisfied by taking advantage of the TM effect which provides a source of SP current in a superconducting junction. Naturally, the TM effect only occurs when a magnetic field is applied and this happens to also be the condition to lift the degeneracy of the spin states in an ESR experiment. With all this in mind, we proposed Vanadyl Oxide Pthalocyanines on Pb(111) probed with a polycrystalline Pb tip as a potential system for ESR-STM.

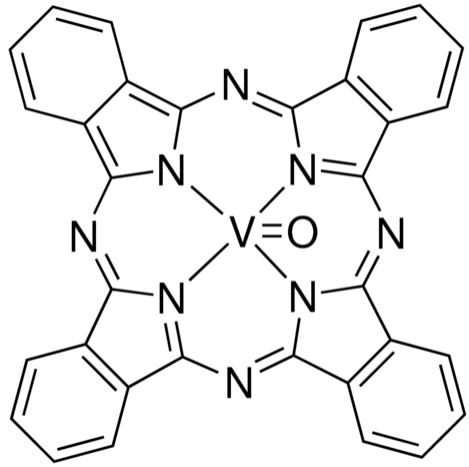

Figure 5.1: Schematic diagram of a VOPc molecule. Taken from Ref. [1]

5.1 Tedrow-Meservey Effect in Pb Tips

One of the main goals of this project was to study the feasibility of using the TM effect as a SP current source for ESR measurements. Fig. 5.2 a) shows an example of the TM effect in Pb tips made by tip shaping the Pb on the Pb substrate. For more details on the tip shaping procedure please refer to the Chap. 2 of this dissertation. We see that the TM effect forms in the presence of a magnetic field and quenches at 2 T (this quenching field changes depending on the tip). At zero field we measure the full superconducting gap that we can then break when we apply a magnetic field. Below the critical field of the TM effect, the superconductivity in the sample is quenched, but the tip remains superconducting due to the confinement effect discussed in Chap. 3. This leaves a tip gap at zero bias as seen for 0.5 T, 1 T and 1.5 T in Fig. 5.2 a). When a large enough field is applied this gap is also broken as seen at 2 T.

The shape of the tip gap and its spin-polarization in a magnetic field can be modelled by plotting two superconducting gaps shifted relative to each other by the Zeeman splitting given for a free electron ($E_Z = g\mu_B B$). In Fig. 5.2 b) we see the TM effect at 1.5 T along with the two SP DOS that make up the full DOS. We get an indication that there is large spin-polarization in the bias range from -0.5 mV to 0.5 mV. In order to understand how the RF driving will cause the TM effect to mix, we simulate the RF response of the data in Fig. 5.2 b) at $U_{RF} = 0.7$ mV using the TG model. We choose this amplitude as it leaves large first order replicas, which gives a region with good spin-polarization. We can see why this is a challenge as already see different replicas overlapping each other mixing the different SP regions. In Fig. 5.2 d) we compare two simulations at different RF amplitudes with the data. We see that even at a relatively small amplitude of 0.7 mV the strength of the TM effect is decreased due to the strongest replica only contributing half of the conductance as the original data. If the driving voltage increases then the replicas mix even more, and the effectiveness of the TM effect also continues to decrease as regions with positive spin-polarization start to mix with regions with negative spin-polarization. We can make two conclusions based off the data and the simulations. First, the voltage of the RF driving has to be carefully chosen to minimize regions of opposing SP DOS combining. In the case of this tip's TM effect, $U_{RF} = 0.7$ mV seems to be an amplitude where the first order replicas are most prominent and therefore making it relatively clear where we would expect SP. Second, the amplitude of the RF radiation cannot be too large as the TM effect will become to spread out which makes it difficult to distinguish between regions of SP and lowers their strength. Based off these simulations, we attempted ESR sweeps by applying $U_{RF} = 0.7$ mV on the junction and probing $U_{DC} = 173$ µeV during the sweep, which is where

we find the strongest spin-polarization. These sweeps were never succesfully realized, which we partially attribute to low RF amplitudes, and weakening of the spin-polarization caused by the replication and mixing of the TM effect.

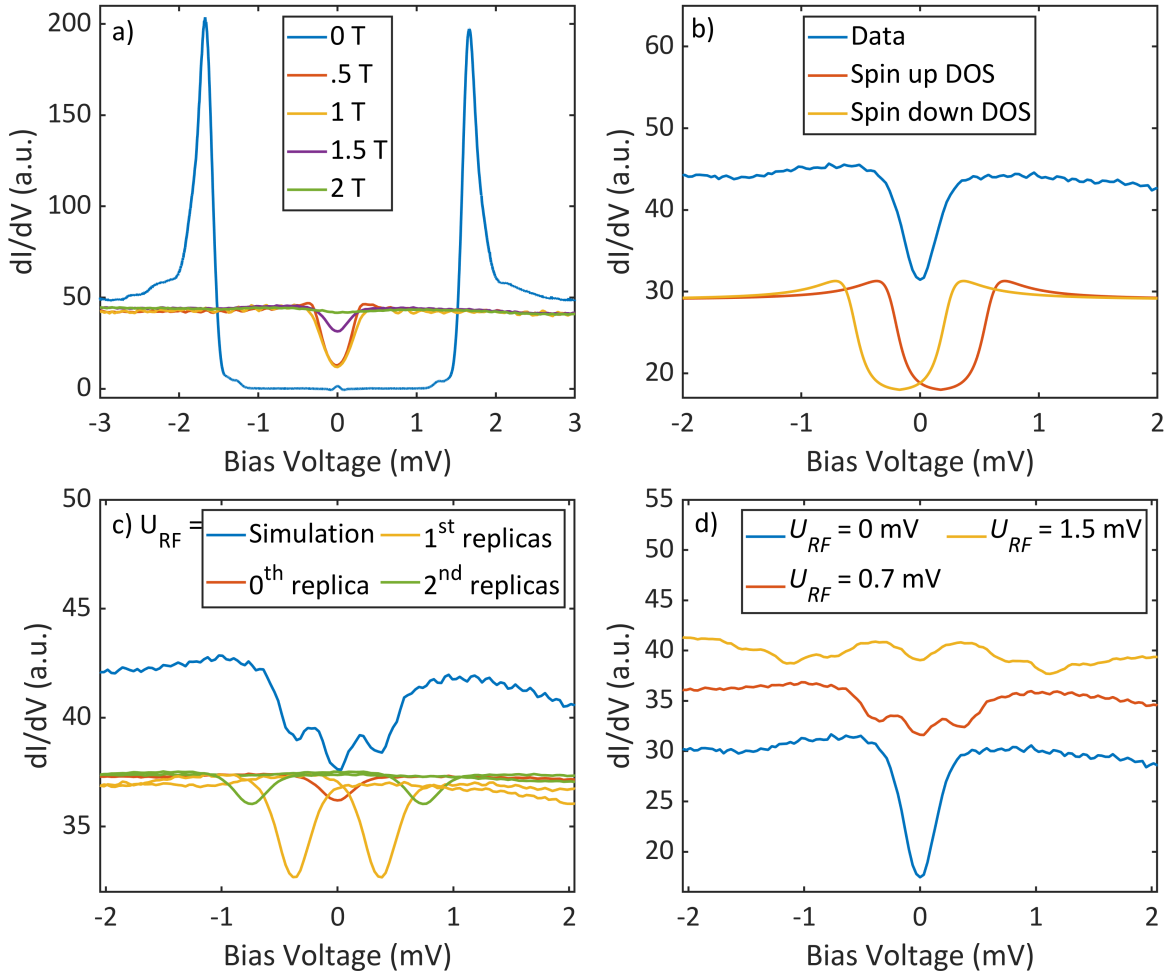

Figure 5.2: a) Superconducting gap and TM effect measured in a Pb-Pb junction (U_{DC} = 5 mV, $I = 5$ nA). b) TM effect at 1.5 T from panel a) along with the estimated SP contributions to the DOS. c) Simulated TG response of the data in panel b) ($U_{RF} = 0.7$ mV, $f = 90$ GHz). The different replicas that make up the TG response are also plotted. d) The TG response of the data in panel b) at different RF voltages. Plots in panel b), c) and d) are offset for clarity.

5.2 Characterization of VOPc Nanocrystals

5.2.1 Topographical Characterization

Although the initial idea was to measure ESR on individual VOPc molecules, the recipe for single atom/molecule deposition was not yet developed and instead VOPc nanocrystals were formed due to the relatively large sample temperature during deposition. An example of such a nanocrystal can be seen in Fig. 5.3 a). We can see that the first layer of the nanocrystal forms in a square lattice crystal structure which is to be expected for a fourfold symmetric molecule such as VOPc, and has been observed for other phthalocyanines deposited on surfaces [90, 105]. We see that the second layer is sparsely populated with two varieties, a typical orientation and a rare orientation (Fig. 5.3 c) and d)). The first layer molecules also have two varieties which is to be expected due to the out of plane O atom connected to the VPc (i.e. the molecule can land with the O down or O up). Previous studies show that the molecules with the large DOS in the middle are O up molecules [58]. By putting markers on

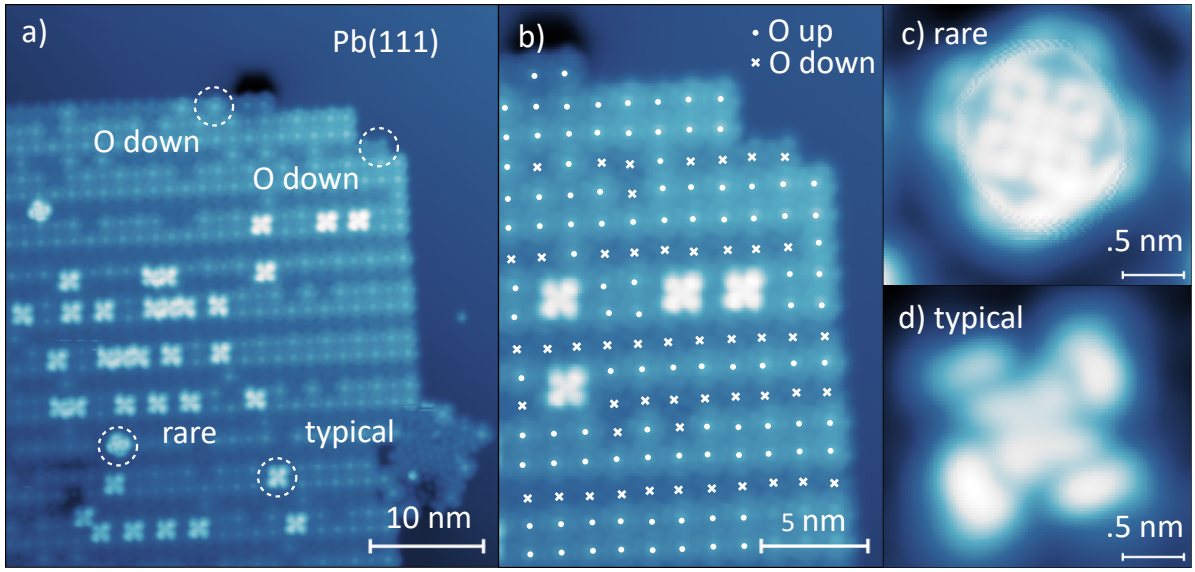

Figure 5.3: a) Topography of a VOPc nanocrystal grown on top of Pb(111) ($U_{DC} = 100$ mV, $I = 100$ pA). One layer of VOPc is formed with the some molecules on the second layer. The four types of molecules are circled and labelled. b) Zoomed in topography of the scan in panel a) ($U_{DC} = 100$ mV, $I = 100$ pA). First layer molecules are marked as dots (for O up molecules) and xs (for O down molecules). Four molecules on the second layer are also visible but not marked. c) Topography of a rare orientation molecule (U_{DC} = 100 mV, $I = 100$ pA). d) Topography of a typical orientation molecule ($U_{DC} = 100$ mV, $I = 100$ pA).

the first layer molecules, as seen in Fig. 5.3 b), one can see that the preferred structure in the first layer is two rows O up and one row O down. Although this is not a strict rule one can get an idea that this is the most energetically favorable formation for this crystal. Furthermore, one can also get some idea of how the typical orientation molecules land on the first layer. It seems that the preferred deposition for these molecules is to land in the corners of four first layer molecules. Similar observations can be done on the the rare orientation molecules, which are usually deposited either on top of a first layer molecule or in between two.

5.2.2 Zero Field Spectroscopy

When measuring spectroscopy on the centers of the molecules we can see two types of behaviours. For the O up and the typical orientation molecules, the superconducting gap is slightly shrunk relative to measurments on clean Pb(111), as shown by the dashed lines on the coherence peaks in Fig. 5.4 a), and we see an asymmetric DOS. On the O down and the rare orientation molecules, we observe Shiba states which shows that the spin living in the vanadium of the VOPc couples to the superconducting surface. Similar observations were made on individual VOPcs deposited on Pb nanoislands [58]. Although there are minor differences between our sample system and the one in Ref. [58], we believe the physics is ultimately the same. It is due to this study we are confident which molecules on the first layer are O up and O down. We do not make a similar conclusion on the second layer molecules as their topographies have not been modelled as in the case of the first layer molecules. In the following we simply refer to them as rare and typical orientation molecules.

5.2.3 Magnetic Field Dependent Measurements

To gain more information on the behaviour of the spin centers, we also measured magnetic field dependent spectroscopy above the critical field. We see an asymmetric DOS on the O up and the typical orientation molecules (Fig. 5.5 a) and b)) and no magnetic dependent response. In the case of the O down and the rare orientation molecules we see two different spin behaviours. The first is a Kondo effect seen on the first layer which is confirmed by plotting the spin splitting energy as a function of field (Fig. 5.5 c) and e)). As the spin splitting intersects the x-axis this confirms a Kondo interaction (refer to Chap. 3 for more info). We estimate a Kondo temperature of 2 K based on a critical field of 0.76 mT and a coupling constant

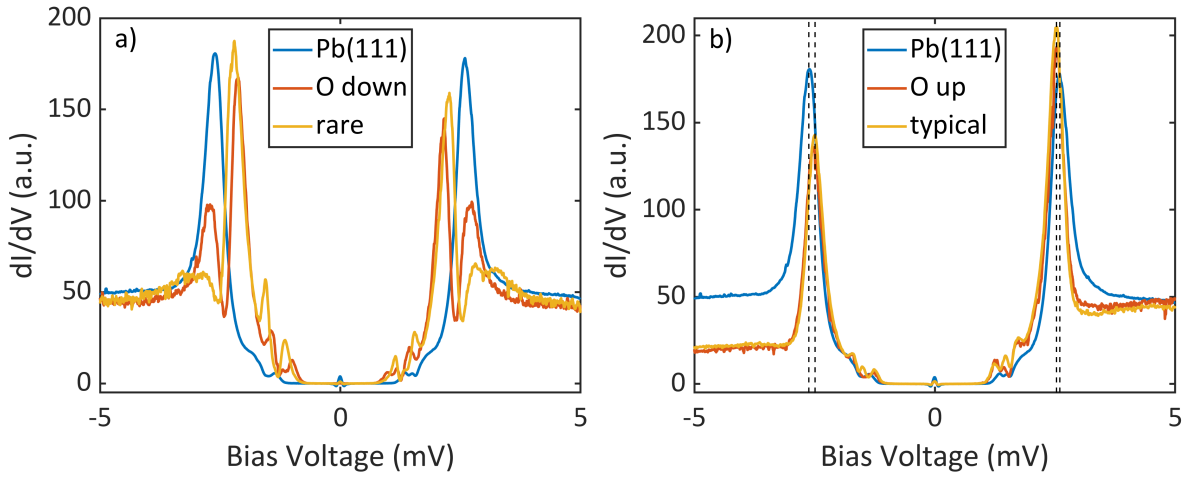

Figure 5.4: a) Spectroscopy on bare Pb(111), showing the superconducting gap, and on the molecule varieties that show Shiba states ($U_{DC} = 5$ mV, $I = 5$ nA). b) Spectroscopy on bare Pb(111) and on the molecule varieties that do not show Shiba states ($U_{DC} = 5$ mV, $I = 5$ nA). Dashed lines show positions of coherence peaks.

of 0.5. This approximation comes from equating the energy of the spin system at the critical field to the energy of the thermal bath [120]:

$$g\mu_B B_K = \kappa k_B T_K \tag{5.1}$$

Here, κ is a coupling constant defining the strength of the interaction between the impurity and conducting electrons, B_K is the critical field where the splitting of the Kondo resonances starts, and T_K is the Kondo temperature. On the other hand, the rare orientation molecules show spectroscopy indicating a higher level spin, which is concluded from the spin splitting intersecting with the y-axis (Fig. 5.5 d) and f)). This shows that the system is not a spin-½ system as there is a zero field spin splitting. Furthermore, this is indicative of the molecules on the second layer being more strongly decoupled from the enviroment than the molecules on the first layer.

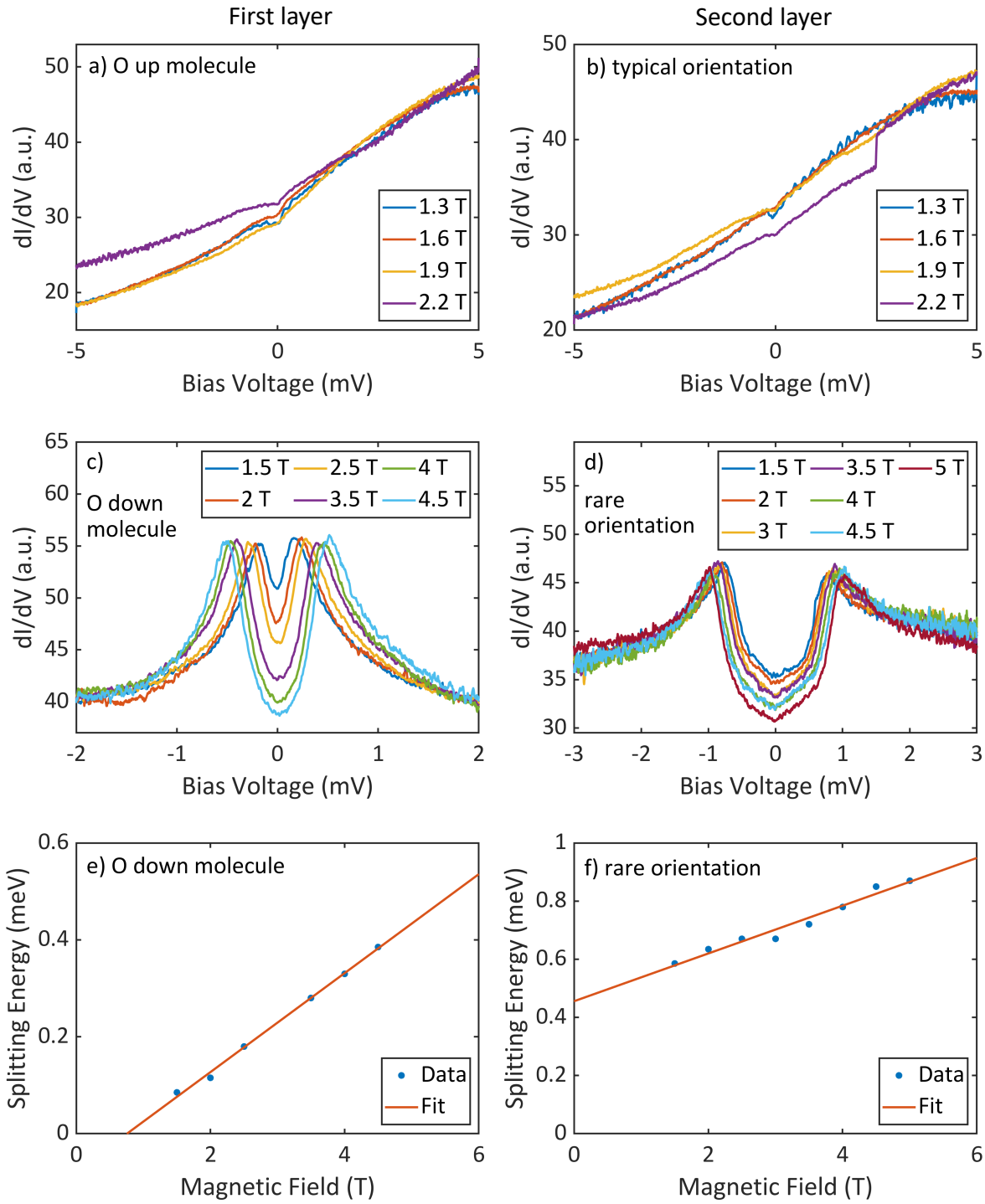

Figure 5.5: a,b) Magnetic field dependent measurements on the magnetically dead molecular types ($U_{DC} = 5\,\text{mV}$, $I = 5\,\text{nA}$). Step in the 2.2 T data of the typical orientation molecule is due to a tip change. c) Magnetic field dependent spectroscopy on a first layer O down molecule ($U_{DC} = 5\,\text{mV}$, $I = 5\,\text{nA}$). d) Magnetic field dependent spectroscopy on a second layer rare molecule ($U_{DC} = 5\,\text{mV}$, $I = 5\,\text{nA}$). e) Spin splitting behaviour extracted from the data in panel c). Shows that the effect measured in panel c) is a Kondo effect. f) Spin splitting behaviour extracted from the data in panel d). Shows that the spin system measured in panel d) is larger than a spin-½.

5.2.4 TM effect on VOPcs

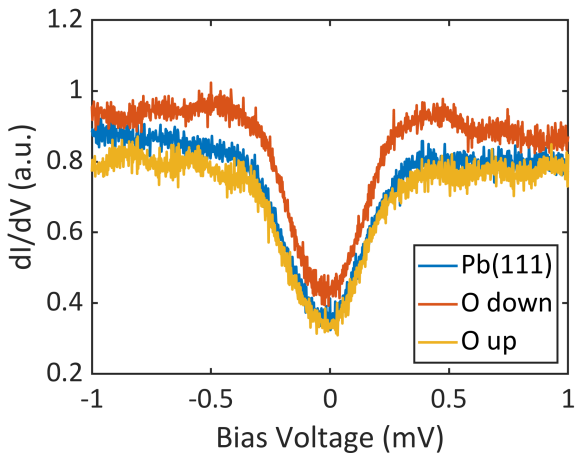

Figure 5.6: Comparison of the TM effect measured on Pb(111) and both varieties of molecules on the first layer ($U_{DC} = 5$ mV, $I = 100$ pA, $B = 1$ T).

As a prerequisite to ESR measurements, we measured the TM effect on first layer VOPcs. We were expecting an assymetric TM DOS which would be indicative of the SP current being sensitive to the spin in the VOPc (what is expected can be seen in Ref. [26]). Unfortunately, as seen in Fig. 5.6 there is very little difference in the TM effect between measurements on clean Pb(111) and on the molecules. This is very likely due to a combination of the TM effect not being sensitive enough and the VOPcs not being decoupled strongly enough. The lack of sensitivity of the TM effect might be due to Pb's relatively high spin-orbit coupling, and the weak decoupling of the VOPcs to the environment would be due to their proximity with conducting electrons in the molecule and substrate. ESR measurements were attempted on this sample system but were never successfully realized. We attest this to the apparent lack of spin sensitivity as seen in Fig. 5.6, and to the small RF amplitudes this measurement has to be performed at as seen in Fig. 5.2 c).

5.3 Discussion and Conclusion

In this chapter we see that there are still two challenges in measuring ESR signals on VOPcs with the use of the TM effect. The first apparent challenge is that relatively small RF voltages need to be used. The second challenge is that the TM effect does not seem to respond to the spin of the VOPc molecules. Ultimately, the sensitivity of the detection scheme has to be improved to overcome these obstacles. This could be done in two ways, either optimizing the tip or by optimizing the spin system. In the former example, we would have to develop a new recipe for creating optimal TM tips which could involve macroscopic machining/etching

of the tip. We could also forgo the TM effect and use the same SP tip that other ESR-STM experiments use (Fe atoms picked up off MgO), and simply use VOPcs as potential spin systems. To optimize the spin system, the decoupling of the spin from the sorroundings would have to be maximized. In the case of VOPc nanocrystals, we could grow crystals with more layers and try to measure ESR signals on molecules on the top most layers as these should be most strongly decoupled. If we wanted to be more certain of our decoupling, we could use a thin insulating film such as MgO. In fact FePc on MgO has been shown to be ESR sensitive making it likely that VOPcs on MgO are also ESR sensitive [119]. Therefore, depositing VOPcs and Fe on MgO grown on Ag(111) might be the most effective way to realize an ESR experiment as it both increases the strength of the SP current and the decoupling of the spin system.

Although there are still several obstacles that have to be overcome before ESR measurements on VOPcs are possible, VOPc multilayers on Pb(111) are shown to be an interesting system to study pthalocynanines, interactions between spins, and interactions between spins and SCs. What was found is that VOPc molecules can form nanocrystals similar to what has been found with other pthalocyanines [90, 105]. What is new in our system is the introduction of an out of plane atom in the molecule, in the form of an O atom bonded to the central V atom. This new component adds a new orientation of the molecule at each layer of the nanocrystal, one orientation that is O up and the other O down. By observing the topography, we can see that the first layer grows roughly in a two O up rows and one O down row pattern, while the second layer has two orientations for molecules which we called typical and rare. We observe Shiba states for both the first layer O down molecules and the second layer rare orientation molecules, along with spin behaviour when measuring magnetic field dependent spectroscopy. In contrast, the first layer O up and the typical orientation molecules show no Shiba states and no magnetic behaviour. Based on these two observations, it is very likely that the typical orientation molecules are O up molecules in the second layer and the rare orientation molecules are O down molecules in the second layer. To confirm this interpretation we would have to simulate the STM images of the typical and rare orientation molecules as it has been done for individual molecules in Ref. [58].

The spin physics in this system is also unique and unexpected as we would expect the VOPc spins to behave as spin-½ systems [58]. We can see from Fig. 5.5 that this not the case as either a Kondo interaction or a free spin with a spin greater than ½ is observed. We know that the free spin is greater than ½ because the spin splitting in Fig. 5.5 f) is still finite in zero field. This would suggest that the individual spins in the VOPcs interact with each other and their enviroments, and therefore the system cannot be described individually and has to be

described as a whole. Furthermore, it is interesting that we can see two different spin behaviours depending on the layer of the nanocrystal. This clearly points to a different decoupling of the spin to the conducting Pb(111) surface. As the first layer is more strongly coupled to the Pb(111), a Kondo effect is observed due to the conduction electrons screening the spin. As one puts distance between the spin and the surface, spin excitation spectroscopy can be measured which indicates that the spin is now more strongly decoupled. This works in a similar way to how spins can be decoupled from a conducting substrate with the use of a thin insulator (i.e. adatoms on MgO). What is also of interest, is that at zero field both the second layer and first layer show Shiba states, suggesting that the proximity effect caused by the superconducting surface is on a longer length scale than the coupling of the spin to the conducting surface.

In summary, we see that two layer VOPc nanocrystals on Pb(111) are a system with many features that interact in a unique way. Namely, there are four different molecular types which all show different behaviours depending on their O up/down orientation and the layer they exist in. We see that there are two types of molecules that are magnetically active and two that are not. We speculate that the magnetically active molecules have an O down orientation and the non magnetic molecules have an O up orientation. We also see that the magnetic activity of the second layer molecules cannot but described by considering the spins individually but rather by considering them as a whole. Lastly, we directly probe the different length scales between the proximity effect of the Pb SC and the length scale on which the molecular spins decouple from the substrate. In summary, this type of system leads to a new understanding of how spins can interact with each other and with SCs, firstly by showing that individual spins in VOPcs form a higher spin system, and secondly by showing that the length scale of the interaction with the superconducting and normal conducting substrate is different.

6 Electron Spin Resonance Scanning Tunneling Microscopy Measured at High Magnetic Fields[1]

The HF cabling and the specially designed antenna in our STM allow for ESR-STM measurements at double and even triple the Zeeman energies that have been previously reported [11, 84, 103, 104, 108]. To realize these measurements we used a sample system consisting of TiH molecules and Fe atoms on thin insulating MgO grown on Ag(100), and a Pt/Ir tip. This sample system was chosen as it has been shown to be an effective system for measuring ESR signals by various groups [83, 92, 104, 111]. In this chapter we present the proof of principle that our STM is capable of measuring ESR signals from 60 GHz up to 98 GHz.

6.1 Topography and Sample Characterization

Figure 6.1 a) shows the topography of the sample system mentioned in the previous paragraph. A two ML MgO flake is shown on the Ag(100) crystal where there are TiH molecules and Fe atoms on top the MgO, labelled and circled for clarity. There are two binding sites for the TiH molecules, on top of an O atom or on-site, TiH_O, and in between two O atoms or bridge-site, TiH_{OO}. Fe atoms land only on-site. The amount of the layers of MgO can be probed either topographically or with FES. Fig. 6.1 b) shows the different FES signatures between one ML and two ML MgO, and is in agreement with what has been previously reported [69]. Furthermore, single layer and multilayer MgO have different topographical heights relative to the Ag(100) substrate when scanned at $U_{DC} = 100\,\text{mV}$, $I = 20\,\text{pA}$ [69]. Generally this is the preferred way to find two ML (or more) MgO as FES tends to sweep

[1] This chapter is based on publication #3 on the publication list

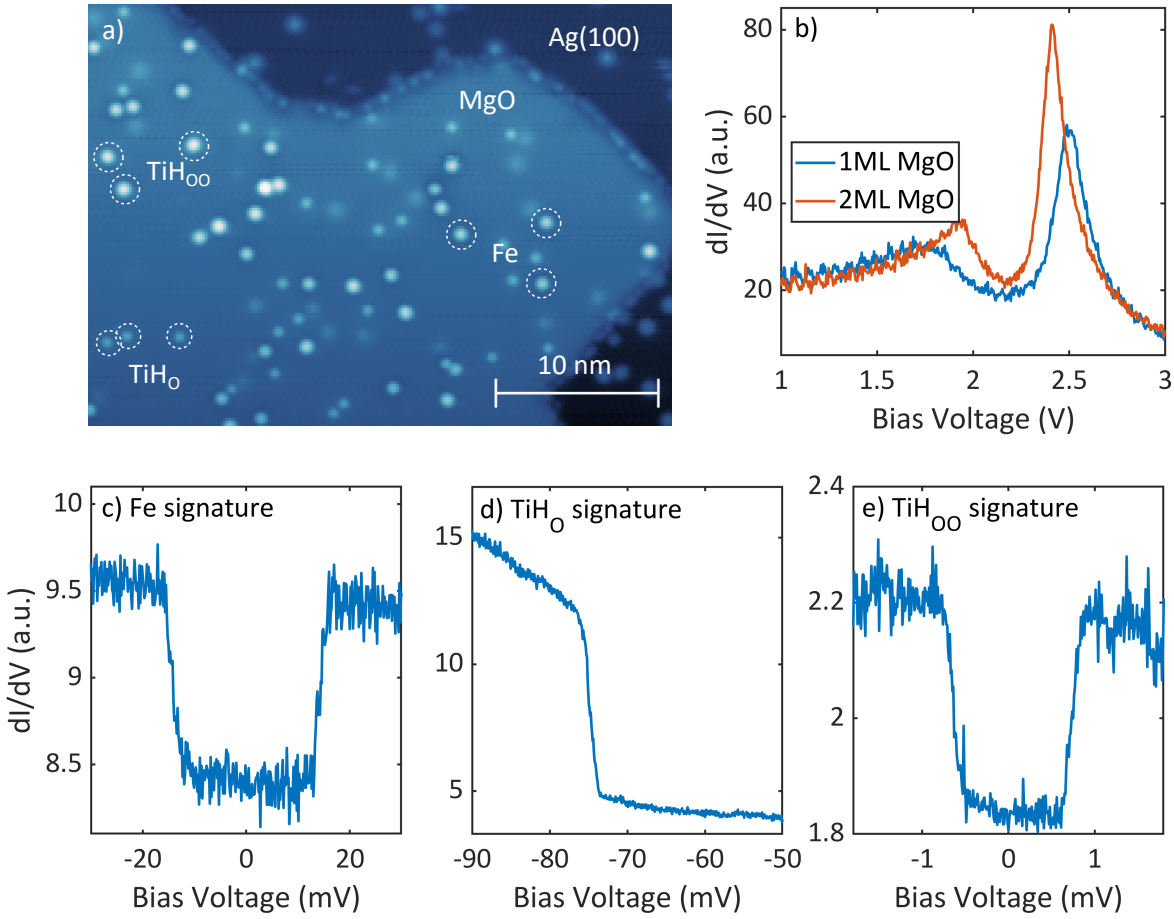

Figure 6.1: a) Topography of the sample system used to measure ESR-STM ($U_{DC} = 100$ mV, $I = 20$ pA). A two ML MgO growth is shown on the Ag(100) substrate. On top of the MgO are various atomic and molecular species circled and labelled. b) FES on one ML and two ML MgO (U_{DC} = 100 mV, $I = 100$ pA). c) Spectroscopic signature used to identify Fe ($U_{DC} = 100$ mV, $I = 500$ pA) showing steps at ± 14 mV. d) Spectroscopic signature used to identify on-site TiH molecules $U_{DC} = 100$ mV, $I =$ 500 pA) showing an IETS step at -75 mV . e) Spin excitation spectroscopy on TiH$_{OO}$ ($U_{DC} = 10$ mV, $I = 500$ pA, $B = 6$ T) showing steps at 0.69 mV. At finite magnetic fields this signature is used to identify these molecules.

all the atoms and molecules off the MgO. It is important to be able to find MgO with more than one layer, as ESR sweeps on single layer MgO have not been demonstrated in literature. With this in mind, all measurements presented in this dissertation were done on two ML MgO.

Fig. 6.1 c-e) show the spectroscopic signatures that are used to identify the various atomic and

molecular species on the MgO. For both Fe and TiH_{OO} spin excitation spectroscopy is used. TiH_{OO} shows these excitation steps while in an external magnetic field, and they behave as one would expect for a spin-½ system. That is to say, the energy of the step will be linearly related to the external field ($eU_{step} = 2\mu_B B$). Spectroscopy on Fe shows excitation steps at $\pm$14 mV and these are not shifted in an out of plane magnetic field [10]. Spin excitation spectroscopy can also be used to identify TiH_O molecules, but they also show an IETS step around -80 mV that is easier to measure than the spin excitations. The origin of this step is speculated to be from an inelastic process related to the vibration of the molecule [93]. The TG response of this step at -80 mV is used to measure the transfer function, similarily to how the coherence peaks were used to measure the transfer function in Chap. 4 (please refer to Subsec. 2.2.1 for more information on the purpose of the TF and its acquisition process). These spectra and their features are in agreement with what has been previously reported [76, 84, 111]. Furthermore, all three of these atomic/molecular species have different topographical heights and shapes when scanning at $U_{DC} = 100$ mV and $I = 20$ pA, and using the topography is the fastest way of identifying the different species. Ultimately, this is very useful for tip shaping as it cuts down the necessary time to find Fe atoms to pick up from minutes down to seconds.

ESR-STM experiments in our set-up are primarily performed on TiH_{OO} molecules due to our magnetic field direction. With our magnetic field pointing out of plane of the sample we have vastly differing *g*-factors for the TiH_{OO} ($g \approx 2$) and the TiH_O ($g \approx 0.6$). This anisotropic *g*-factor has been observed previously and is due to a large orbital angular momentum of the electronic ground state [92]. The differing *g*-factor is relevant in our experiment as we are not able to Zeeman split the states in the TiH_O strongly enough ($E_Z(g = 0.6, B_{ext} = 6\,\text{T}) = 208.38\,\mu\text{eV}$) to probe them with our HF radiation ($h\cdot 60\,\text{GHz} = 248\,\mu\text{eV}$). Therefore, we take advantage of the large *g*-factor in TiH_{OO} molecules and all the data presented on this dissertation has been measured on bridge-site molecules unless otherwise specified.

6.2 Characteristics of Good Electron Spin Resonance Tips

As mentioned in Chap. 2, tips for ESR-STM measurements are made by picking up Fe atoms. Picking up Fe atoms is done by bring the tip close to the atom and applying a bias pulse as previously explained. Fig. 6.2 shows spectroscopy on Fe, TiH_{OO} and TiH_O with varying tips. It

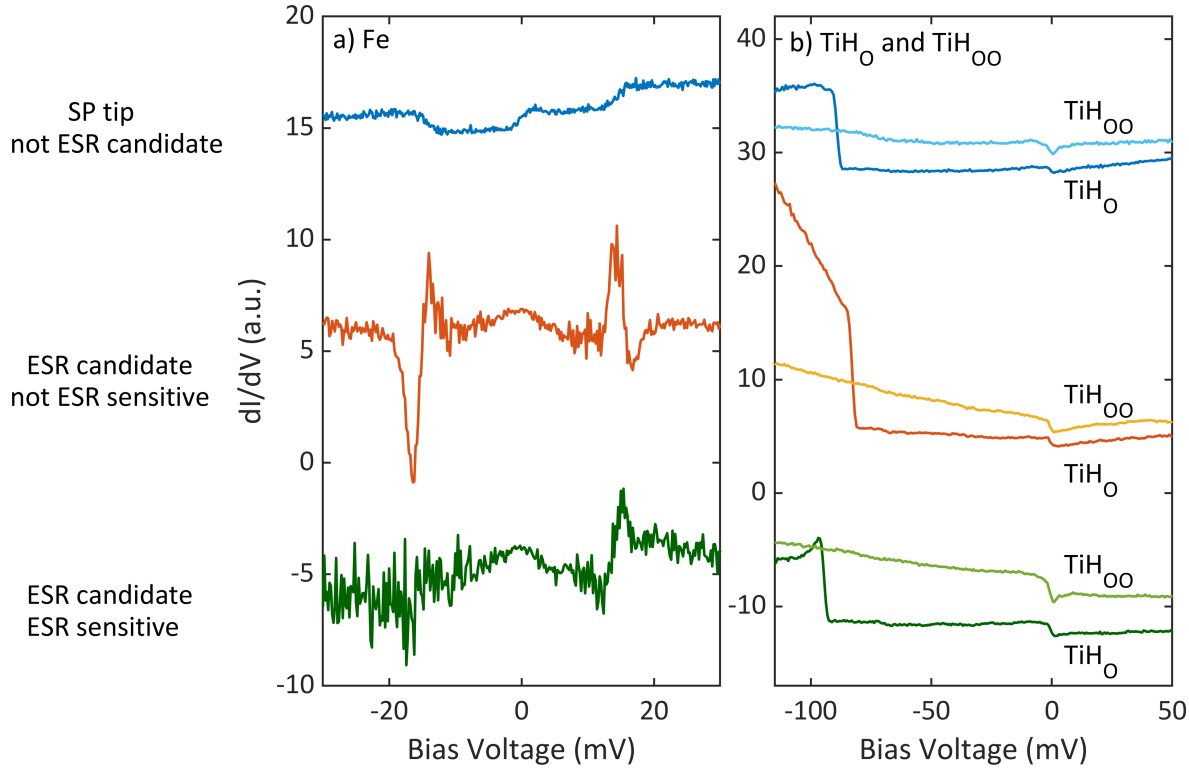

Figure 6.2: a) Spectroscopy on Fe performed with different tip types ($U_{DC} = 100\,\text{mV}$, $I = 500\,\text{pA}$). Tip types from top to bottom: a SP tip that is not a candidate to be an ESR tip, a tip that is an ESR tip candidate but is not able to measure ESR signals and a tip that is both an ESR tip candidate and able to measure ESR signals. ESR tip candidates show peaks or dips around $\pm 14\,\text{mV}$. b) Spectroscopy on TiH_{OO} and TiH_O performed with different tip types ($U_{DC} = 100\,\text{mV}$, $I = 500\,\text{pA}$). Tip types and order are same as in panel a). TiH_{OO} data are plotted in a lighter color than the TiH_O data. Data is offset in both panels for clarity.

demonstrates the spectroscopic signatures needed to make a tip capable of measuring ESR signals. All spectra were taken with tips that had some Fe atoms on the apex. The top most spectra in Fig. 6.2 a) and b) show what is expected from a basic SP tip as we see a change in conductance over zero bias for all three spectra [111]. Even though we see spin-polarization, this tip would not be considered a candidate and is very likely not able to measure an ESR signal. We sequentially pick up Fe atoms and check their candidacy by measuring spectroscopy on Fe. Tips that are ESR tip candidates display peaks or dips located at $\pm 14\,\text{mV}$ when measuring spectroscopy on Fe, as shown in the middle or bottom of Fig. 6.2 a). The observation that the peak/dip feature in spectroscopy on Fe makes good ESR tip candidates has been previously reported but is not currently fully understood [103]. After finding a candidate tip, we also check the strength of its spin-polarization on either TiH species. The larger the step at

zero bias, the more likely it is that the tip will be able to measure ESR signals. A comparison between two ESR tip candidates can be seen in the middle and bottom of Fig. 6.2. On the left we see that they both show peaks or dips at ± 14 mV indicating they are candidates. On the right we see that the spin-polarization for the bottom tip is stronger than for the middle tip. This suggests that the bottom tip is more likely to be able to measure an ESR signal which is the case, as the bottom tip was ESR sensitive while the middle tip was not ESR sensitive. ESR sensitivity is checked by doing tip field sweeps which we discuss in the following section. It is important to note that the bottom data in both panels were measured with the same tip and the middle data in both panels were measured with the same tip, but top data for both panels were measured with different tips. Even though this is the case, the data at the top of the panels is still a good representation of what is to be expected from a basic SP tip.

6.3 Electron Spin Resonance Sweeps

Once we find an ESR tip candidate the easiest way to check if it is ESR sensitive is by doing tip field sweeps as shown in Fig. 6.3. Here the external magnetic field and RF are kept constant (which is why this measurement is ”easy”) and the tip height is adjusted. As adjusting the tip height changes the magnetic tip field felt by the spin system, this experiment effectively sweeps the ZE to find the resonance signal. If we vary the driving energy by changing the RF, the z-displacement at which the ESR signal will be measured at will also change as seen in Fig. 6.3. This type of behaviour is the best indicator that a tip is ESR sensitive.

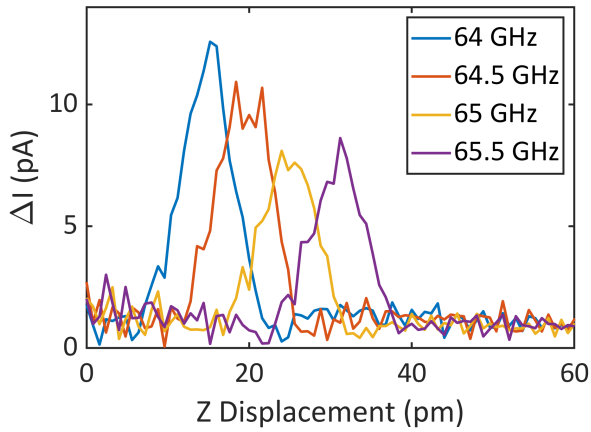

Figure 6.3: ESR peaks measured by sweeping the tip field ($U_{DC} = 100$ mV, $I_{init} = 1$ nA, $B_{ext} = 2.44$ T). RF amplitude varies between measurements. Peak position changes depending on the RF as the resonance conditions change. Direction of the displacement is away from the sample.

The most common method for measuring ESR-STM signals is by sweeping the frequency of the driving radiation at a constant amplitude. As our transfer function lacks the necessary transmission across the whole frequency range of 60 to 100 GHz, we are only able to measure ESR signals in specific bands in this frequency range. Panels a) and b) of Fig. 6.4 show examples of ESR frequency sweeps at two current set points. It is shown that we can measure ESR signals over a large range of frequencies and we see that smaller currents result in smaller narrower ESR signals which is in agreement with literature [108].

The less common, but for us the more favorable, method of measuring ESR signals involves sweeping the magnetic field. This is more favorable for us due to the many individual frequencies we find in our TF. Although our transfer function does not have continous transmission from 75 to 90 GHz, it does have a plethora of single frequencies which can radiate at the necessary powers into the junction. We can take advantage of these frequencies by using magnetic field sweeps. In this way we can cover a far larger range of ZEs that we could not do with frequency sweeps. In fact, Fig. 6.4 c) shows that we can cover a range from 60 GHz to 98 GHz. One other advantage that field sweeps provide is that it removes the necessity to measure transfer functions which ultimately speeds up data acquisition.

With the demonstration of ESR sweeps, the first and main analysis that can be down is the extraction of the *g*-factor of the spin system and the tip magnetic field. Fig. 6.4 d) shows the ESR peak energies as a function of the external magnetic field along with the linear fits to these data points. We can see that the data quality is excellent with the experimental data almost perfectly placed on the linear fit. From the linear fits we can extract the *g*-factors for the various measurements and find that it is around 2 ($g = 2.005 \pm 0.003$, 2008 ± 0.009 and 1.988 ± 0.008) which is to be expected from a spin-½ system. Lastly, we can extract the tip field values of 95.7 mT and 95.1 mT for the magnetic field and frequency sweeps at $I =$ 175 pA respectively, and a tip field value of 46.1 mT for the frequency sweep at I = 50 pA. The difference in the tip fields between these two set points is of course due to the different tip sample distances in these two experiments.

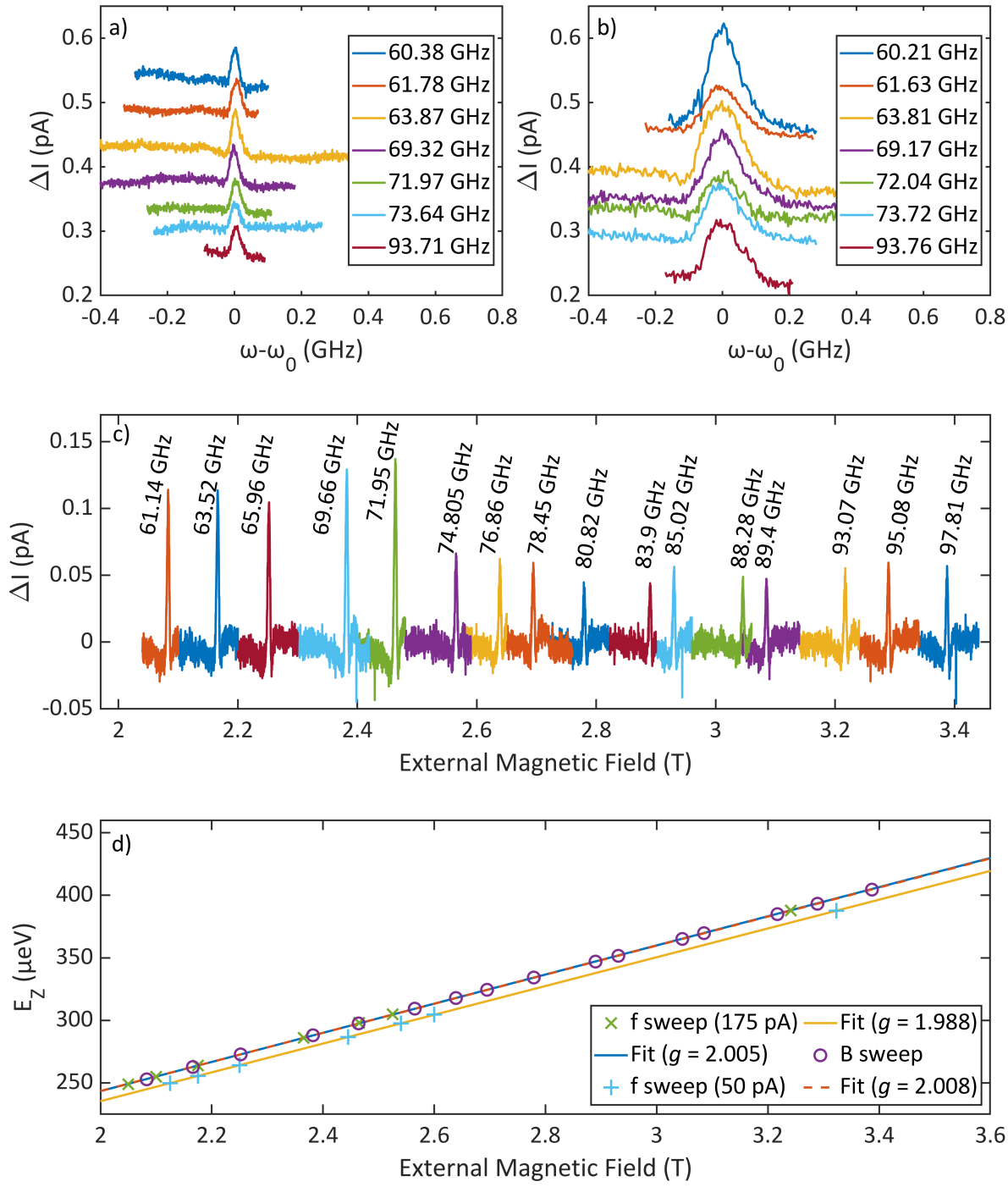

Figure 6.4: a) ESR signals measured by sweeping the driving frequency ($U_{DC} = 100$ mV, $I = 50$ pA, $U_{RF} = 20$ mV). Data is offset for clarity. b) ESR signals measured by sweeping the driving frequency (U_{DC} = 100 mV, $I = 175$ pA, $U_{RF} = 20$ mV). Data is offset for clarity. c) ESR signals measured by sweeping the external magnetic field ($U_{DC} = 100$ mV, $I = 175$ pA, $U_{RF} = 20$ mV). d) Linear fits to data presented in the previous three panels.

6.4 Transfer Function Deviations

With the new development in the HF cabling and delivery for ESR-STMs, we also wanted to see how stable and robust the resulting transfer function is. For other machines the transfer function changes every couple of days and is effected most strongly during LHe filling [68]. In our case the transfer function changes significantly from day to day as shown in Fig. 6.5 a) and b). Fig. 6.5 a) shows the changes in the transfer function after 24 hours and Fig. 6.5 b) shows how the ESR signal can not be measured with the 24 hour old transfer function. These changes seem to happen more frequently than with other machines which indicates that at higher frequencies the transmission mechanism becomes more sensitive to external factors. To overcome this we have to measure the necessary transfer function daily, which is another reason why we prefer performing magnetic field sweeps during our ESR-STM experiments. It is also important to note that there were no major operations performed on the STM (LHe filling, He^3 condensing, magnetic field ramping, etc.) in between the two transfer function measurements in Fig. 6.5 a) which further punctuates the sensitivity of our HF line.

There can also be large changes in the TF when replacing the tip and when heating up and cooling the STM (Fig. 6.5 c) and d)). The latter is caused by movement of the inner conductor relative to the dielectric shielding of the HF cable. The HF cable is not rated down to the experiment temperatures, and a shift of the inner conductor occurs during tip and sample transfer as the junction is moved up and down bending the HF cabling. The movement of the inner conductor in turn moves the pin in the HF to SC connector below the He^3 flange. The pin movement can then cause large changes in the transfer function. We find that replacing the connector along with the HF cabling any time the machine is heated to room temperature is an effective way of eliminating this problem. The TF can also be largely effected by the tip holder and tip wire length as shown in Fig. 6.5 d). As the coupling of the RF field is due to radiation hitting the tip and tip holder, the geometry of the tip and tip holder will effect the efficiency of this coupling (which is unlikely the case when the RF signal is directly sent through the tip wire). Fig. 6.5 d) shows that if the tip holder is too long then the external radiation does not couple effectively to the tip. This is likely due to the radiation not being able to hit the tip wire effectively as the tip holder is in the way. The purpose of this long tip holder was to allow us to choose a tip wire length that would resonate as a $\lambda/4$ resonator (i.e. we wanted to match the length of the tip wire to a 1/4 of the wavelength of the radiation). It is clear from the data that the long tip holders give a worse transfer function, which we believe is due to them casting a larger shadow on the tip wire than the short tip holders. We also

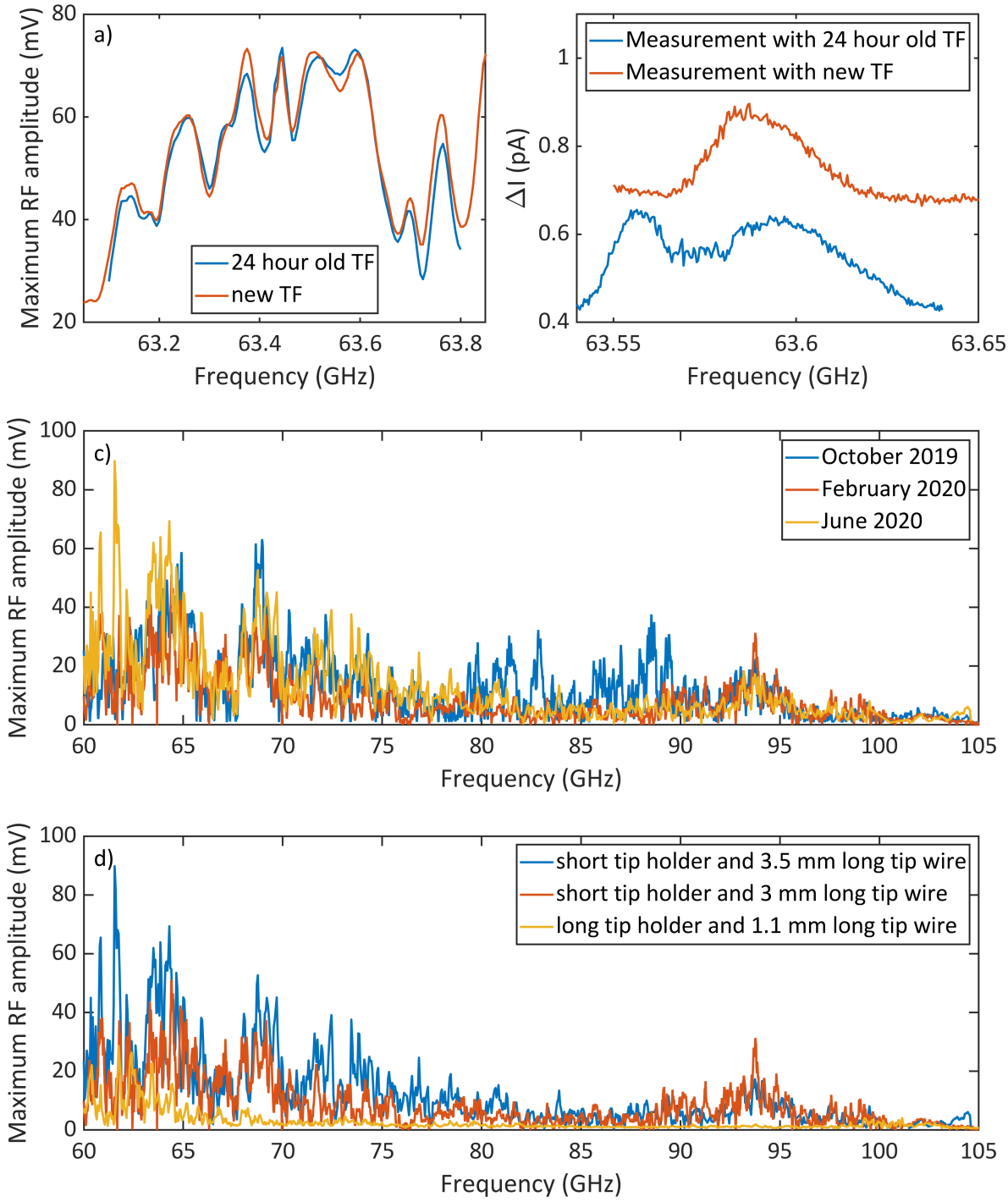

Figure 6.5: Transfer functions are represented by plotting the maximum available RF voltage in the junction. a) Change in the transfer function over the course of 24 hours. No LHe filling, He^3 condensation or magnetic field ramping between measurements. b) ESR sweep with a 24 hour old transfer function and with a new transfer function ($U_{DC} = 100$ mV, $I_{SP} = 50$ pA, $U_{RF} = 20$ mV). Data is offset for clarity. c) Deviations in the transfer function caused, in part, by heat ups (i.e. there was a heat up to room temperature in between each data set plotted). d) Deviations in the transfer function caused by different tips and tip holders.

tested the tip wire length with short tip holders and we see that the wire length has a strong effect on the transfer function (Fig. 6.5 d)). There are several possible reasons why this might be. Firstly, the differing apexes of these tips may lead to different field enhancement effects that are frequency dependent. Secondly, the radiation might resonate better at frequencies that match the tip wire length and therefore create a stronger transmission. Thirdly, there are different surface areas for both tips and therefore the RF coupling should differ (although this effect is probably not frequency dependent). For more details on the geometry of the tip holders and tip wires please refer to Chap. 2.

6.5 Outlook

Now that we have demonstrated that our ESR-STM functions as we expect there are many experiments that could be done. Firstly, temperature dependent measurements were performed and are presented in Chap. 8 of this dissertation. The goal here was to probe the transition from an initialized ground state to a mixed state measurement. Secondly, a pump-probe scheme could be implemented and then the excitation and coherence times of ESR signals could be measured as a function of the ZE. This would be taking advantage of the initialized ground state of our ESR measurements and our HF range. This is also scientifically significant as it is not clear whether excitation/coherence times are related to spin splitting. If they are indeed related this could lead to ways to increasing excitation/coherence times which is relevant for the field of quantum information processing. This could be integrated with the temperature dependent measurements, which would lead to understanding how population dynamics of a spin system effect the excitation and coherence times. Furthermore, there are plenty of ESR-STM experiments that would still be of interest but do not use the unique capabilities of our set-up. Pump-probe functionality would pave a way for coherently controlling several coupled spins which would let us study their dynamics and creates a possibility for quantum computing on the atomic scale. Secondly, new insulating substrates could be tested to see what can and cannot be used to measure ESR-STM signals. Currently, MgO is the only insulator on which ESR has been successfully measured and the question arises as to what makes MgO so special. Also, new spin systems should be found and tested as only four have been found to produce an ESR signal [11, 111, 115, 119]. Lastly, the use of ESR-STM has been used almost exclusively to study electron spins and could in principle be used to measure nuclear spins. This is also a direction in which ESR-STM experiments could develop.

7 Atomic Scale Electric Field Control of Spin Transitions[1]

During our initial characterization of the ESR signal we found that the position and amplitude of the ESR signal changed when changing the bias voltage applied in the junction as seen in Fig. 7.1. This figure shows the ESR signal (indicated by black arrows) measured at several biases being positioned at different field values for magnetic sweeps performed at the same driving frequency ($f = 61.545$ GHz). All data presented in this chapter was measured with the feed back loop open so we indicate the set point current and bias at which the feedback loop was opened as U_{SP} and I_{SP}, which in the case for Fig. 7.1 U_{SP} = 100 mV and I_{SP} = 250 pA. We use this convention for the rest of the chapter. We strived to study and understand this bias dependent phenomenon as it could lead to new pathways for electrical control of spins which is of great interest to the scientific community, and because in the short time that ESR-STMs have existed this phenomenon has not been reported in literature [52, 53, 65, 75, 81, 100, 110]. What we found is that the ESR signal shifts on the order of several FWHMs when varying the electric field between the tip and sample. We also found this effect to be

[1]This chapter is based on publication #1 on the publication list

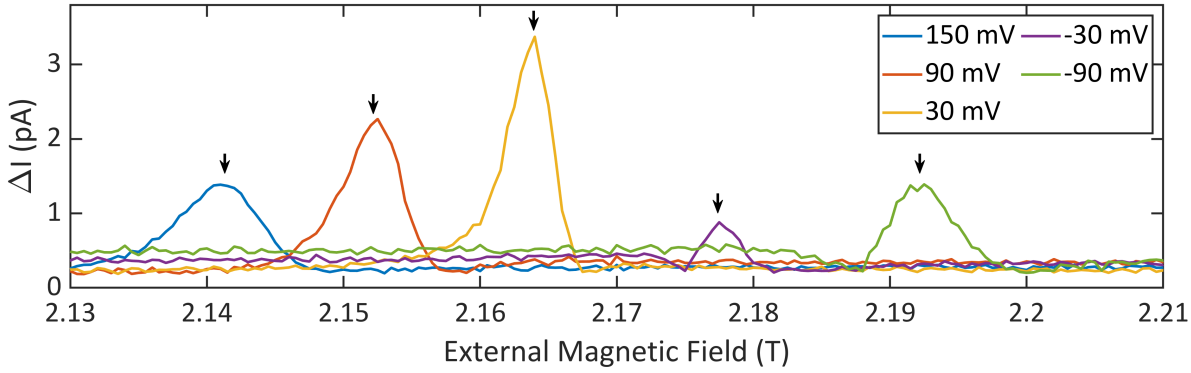

Figure 7.1: ESR signals measured at fives biases (U_{SP} = 100 mV, I_{SP} = 250 pA, U_{RF} = 20 mV, f = 61.545 GHz). Arrows indicate ESR signals.

reproducible among many tips and TiH molecules. Furthermore, we measured this effect on different binding sites, different set points, different ZEs and at varying RF amplitudes. By taking a full data set at various ZEs and current set points, we extract bias dependencies of the *g*-factor and tip fields and conclude that the bias dependency of ESR signals is the result of *g*-factor modulation. The following chapter is a summary of the experiments performed and insight into the bias dependent ESR-STM mechanism.

7.1 Experimental Results

7.1.1 Bias Dependent Electron Spin Resonance on Ti_{OO} at High Frequencies

The basic experiment that we performed during this project consisted of measuring the ESR response as a function of both bias voltage and magnetic field where the magnetic field is the slow direction (which we shorten to bias-magnetic sweeps for the remainder of this thesis). This is done by radiating the junction at one frequency, and then at each magnetic field value bias spectroscopy is performed while the internal lockin records the change in the current at the RF chopping frequency (please refer to Sec. 2.2 for more info on the RF chopping). Fig. 7.2 shows examples of the resulting data from this experiment scheme. Immediately several things are apparent. First, the position of the ESR signal seems to be linearly dependent on bias at positive bias. Second, the magnitude and shape of the ESR signal seems to change depending on the bias voltage and there is a large change when transitioning over zero bias. Third, there is a background signal off resonance that seems to stay relatively constant over magnetic field and seems to interact with the ESR signal. In this dissertation we primarily strive to understand the most apparent and experimentally exciting feature, the linear dependency of the ESR signal with respect to bias. We find this feature to be exciting as it is a direct way of controlling spin transitions with an electric field, which builds on the field of spintronics. Knowing that a shift in the ESR signal is either due to a change in the *g*-factor or the tip field, we can start understanding the bias dependent ESR-STM mechanism by extracting bias dependencies of the *g*-factor and tip field. We can do this by measuring bias dependent sweeps at various ZEs and then performing linear fits akin to Fig. 6.4 d). Sweeps measured at several ZEs are shown in the panels of Fig. 7.2. Changing the ZE seems to slightly affect the flavor of the ESR bias-magnetic sweeps but this is likely due to the tip and will be explored further in the next chapter. Other than this, changing the ZE does not strongly affect the dependency

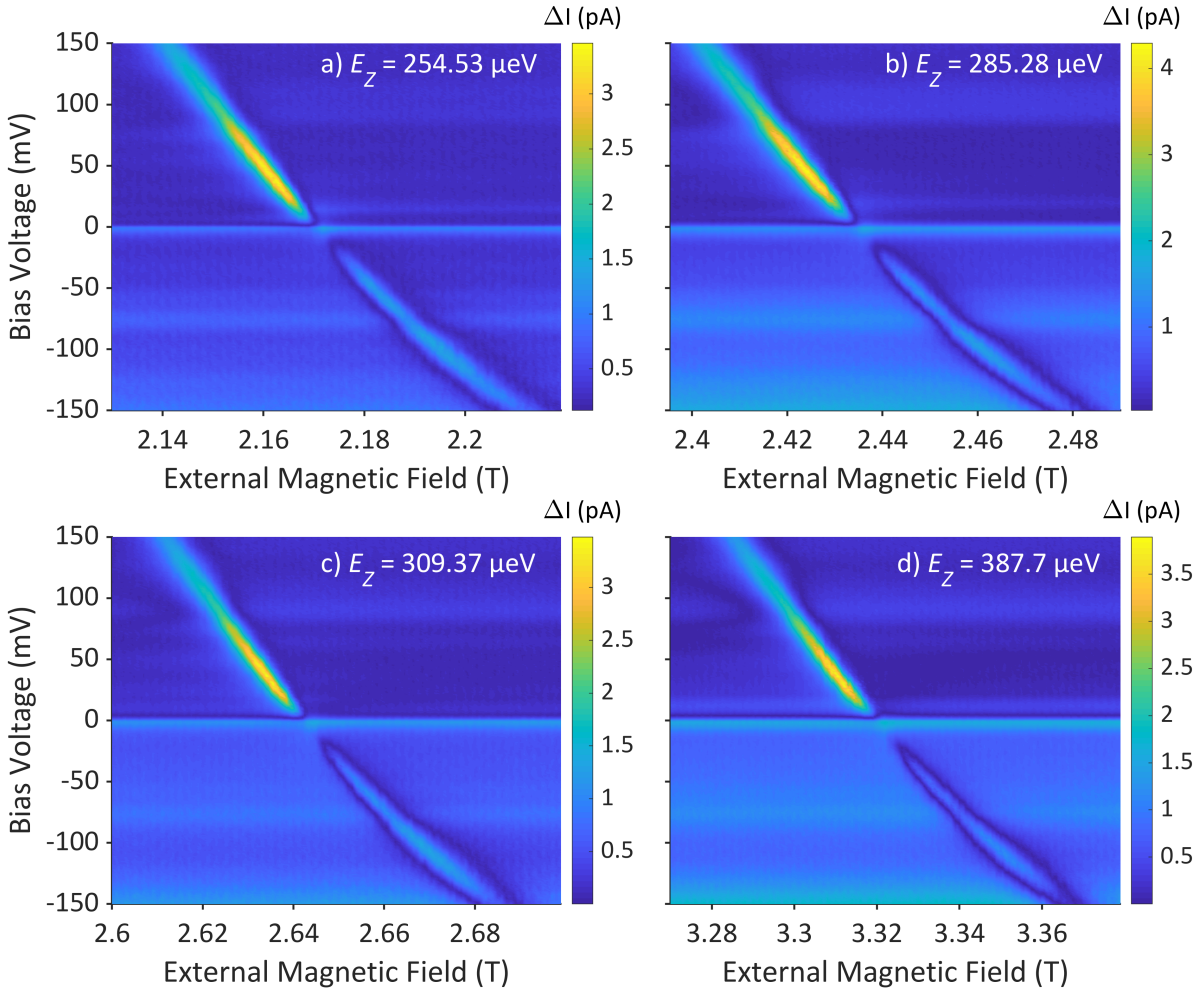

Figure 7.2: a-d) Bias dependent ESR sweeps measured at four ZEs (U_{SP} = 100 mV, I_{SP} = 250 pA, U_{RF} = 20 mV, E_{Z1} = 254.53 µeV, E_{Z2} = 285.28 µeV, E_{Z3} = 309.37 µeV, E_{Z4} = 387.7 µeV).

of the ESR signal versus bias nor does it change the background. We extract the *g*-factors and tip fields and interpret the data in the following subsection.

In the next set of experiments we changed the distance between the tip and sample, as this directly changes the electric forces acting in the junction. In this way we continue to build on the understanding of bias dependent ESR-STM. An example of these sweeps, at one ZE, can be seen in Fig. 7.3. We can see that increasing the tip sample distance decreases the effect of the bias voltage on the shift of the ESR signal. We can also see that the point where the ESR signal crosses zero bias changes due to the different tip fields. To extract the dependencies of the *g*-factor and the tip field on the bias and tip sample distance, we also measured at these four current set points at four ZEs. The analysis of that will be shown in the next section (Sec. 7.2).

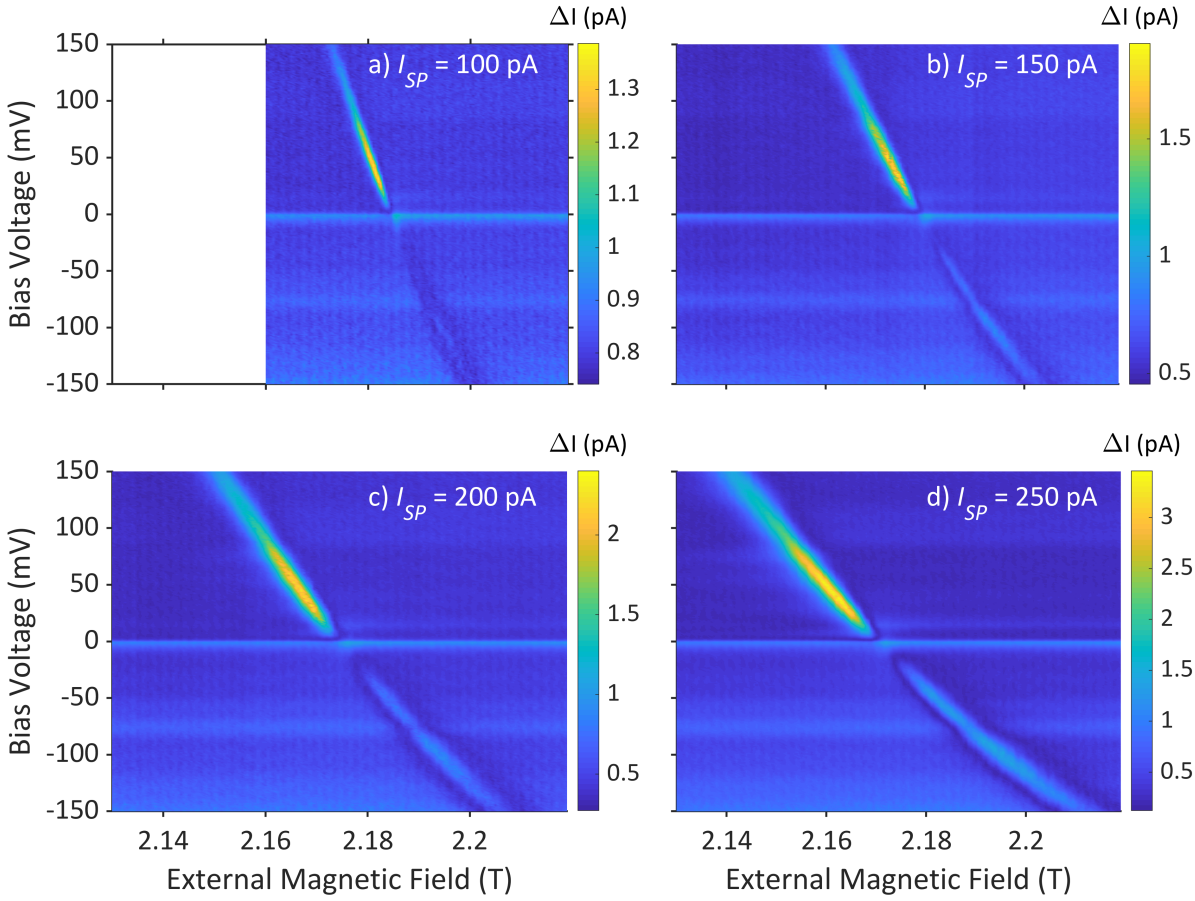

Figure 7.3: a-d) Bias dependent ESR sweeps measured at four current set points (U_{SP} = 100 mV, U_{RF} = 20 mV, f = 61.545 GHz)

To further investigate these bias-magnetic sweeps we also performed them at varying RF amplitudes. Although the RF voltage should not have a direct effect on the DC field, studying it may lead to an understanding of the RF background and ESR signal shape and magnitude found in our sweeps. Fig. 7.4 shows the complete set of measurements. It seems that increasing the RF amplitude increases the signal of the ESR response as expected but also has some unexpected consequences. First, at some point the background signal seems to more strongly interact with the ESR signal and causes it to deviate from being linearly dependent on bias above U_{DC} = 0 mV. This is most clearly seen at U_{RF} = 40 mV and U_{RF} = 50 mV, but starts to happen even at U_{RF} = 20 mV. Second, At U_{RF} = 50 mV the background signal is even stronger than the ESR signal at biases in the -150 mV to -130 mV range. As the background signal is significantly smaller than the ESR signal at lower RF amplitudes, this suggests that there are two different RF amplitude dependencies acting on the ESR signal and the RF background. Third, the position of the maximum ESR signal on the bias axis seems to increase with increasing RF amplitude which is important to consider when trying to maximize the signal from an ESR signal.

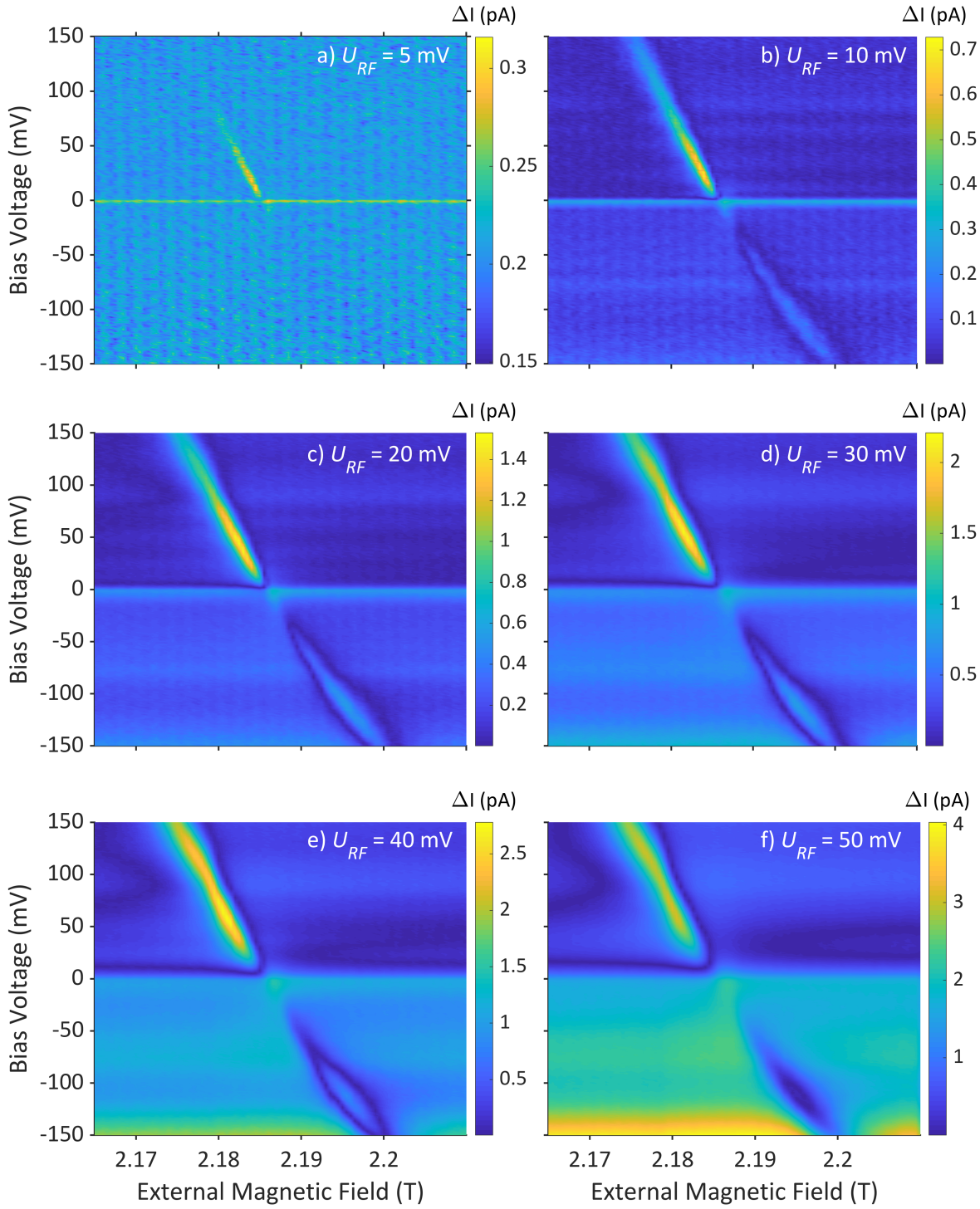

Figure 7.4: a-d) Bias dependent ESR sweeps measured at six RF voltages ($U_{SP} = 100$ mV, $I_{SP} = 100$ pA, $f = 61.545$ GHz)

7.1.2 Bias Dependent Electron Spin Resonance on Ti_O

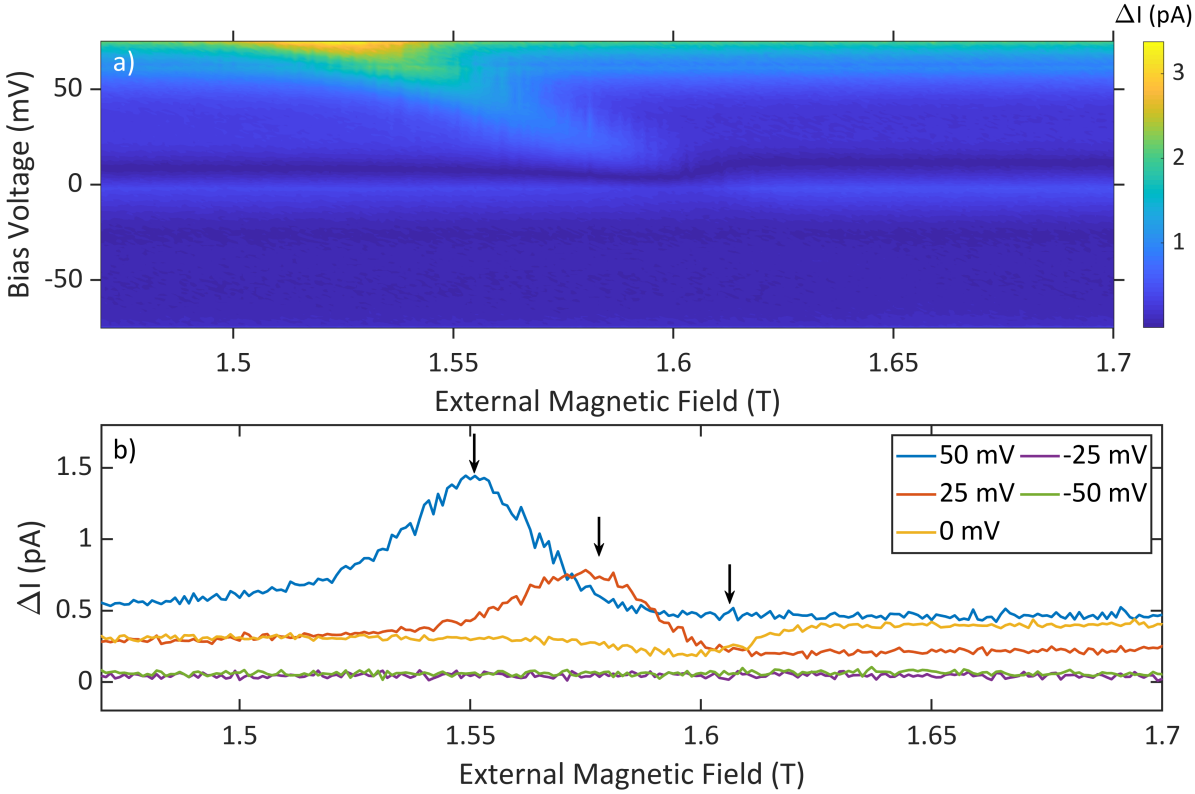

Figure 7.5: a) Bias dependent ESR sweeps measured in our LF set-up on TiH_O ($U_{SP} = 100$ mV, $I_{SP} = 100$ pA, U_{RF} = 20 mV, $f = 19$ GHz). b) ESR sweeps at three biases in our LF set-up on TiH_O (same parameters and data as panel a)). Arrows indicate positions of ESR signals.

After the initial measurements performed on TiH_{OO} at $f > 60$ GHz, we also wanted to study TiH_O molecules whose ESR signal is not accesible with our HF and magnetic field range. We changed our set-up to one that allows us to send RFs between 10 GHz and 20 GHz as described in Sec. 2.3.3. This allows us to measure ESR signals on TiH_O molecules. Similarily to the TiH_{OO} measurements, four tip sample distances were measured at four ZEs each. Fig. 7.5 shows a bias-magnetic sweep performed at $f = 19$ GHz along with individual ESR sweeps at specific biases (ESR signals are indicated with black arrows). We can see a similar linear bias dependency of the ESR signal when comparing with the TiH_{OO} species, but there are also differences in the background and at negative bias. As the background is likely some RF response of the DOS of the molecular species, we attest these differences to the differences in the DOS of TiH_{OO} and TiH_O species. Furthermore, the shift of the ESR signal seems to be much stronger in TiH_O than in the case of TiH_{OO} as the ESR shift in TiH_{OO} is on the order of tens of mT while the shift in TiH_O is on the order of hundreds of mT. Lastly, we see that unlike on TiH_{OO}, there

is no signal in the negative bias range on TiH_O which we account to differences in the DOS between the two species.

7.1.3 Bias Dependent Electron Spin Resonance on Ti_{OO} at Low Frequencies

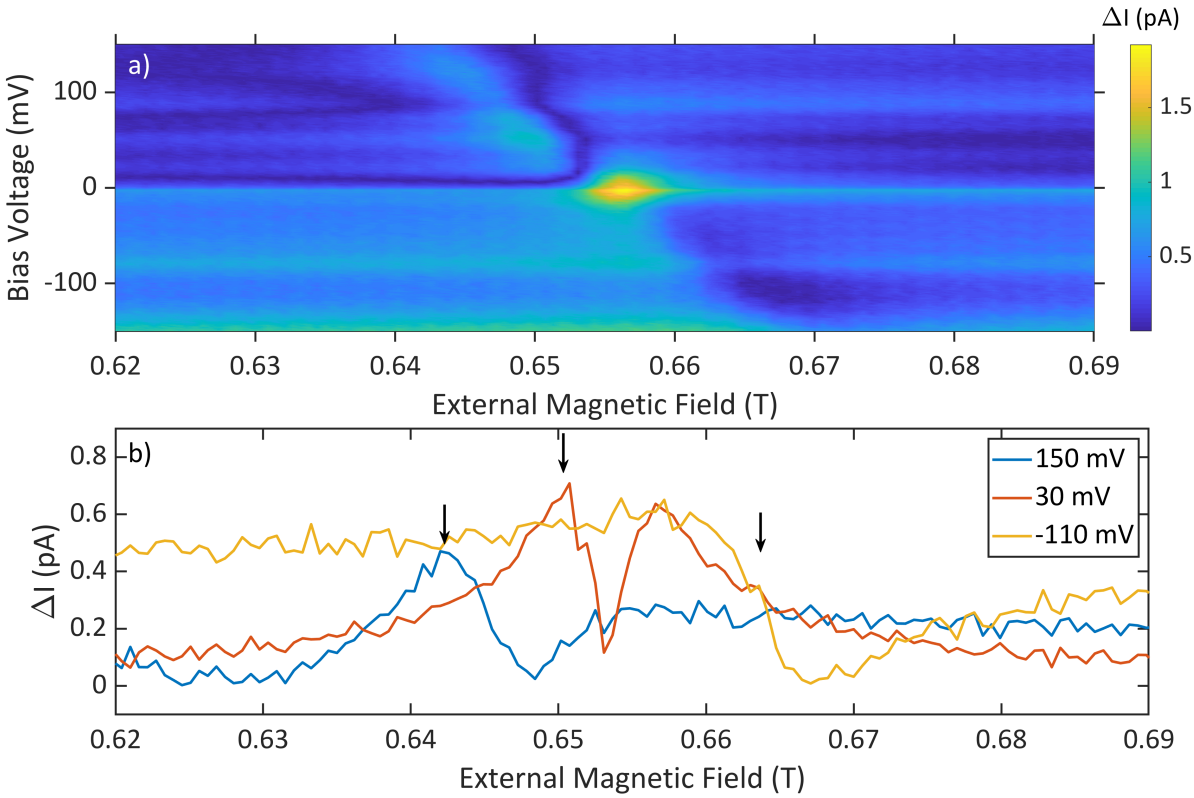

Figure 7.6: a) Bias dependent ESR sweeps measured in our LF set-up on TiH_{OO} ($U_{SP} = 100$ mV, $I_{SP} = 250$ pA, $U_{RF} = 20$ mV, $f = 19$ GHz). b) ESR sweeps at three biases in our LF set-up on TiH_{OO} (same parameters and data as panel a)). Arrows indicate positions of ESR signals.

While our machine was set-up to probe low frequencies (LFs) we took the oppurtunity to check bias-magnetic sweeps on TiH_{OO} in the low ZE regime. Fig. 7.6 shows a bias-magnetic sweep done at $f = 19$ GHz along with individual ESR sweeps at specific biases. Looking at Fig. 7.6 a) and b) we can see that the shape of the ESR signal and the RF background has changed but the linear dependency of the ESR signal with respect to to the bias voltage remains the same. The individual ESR sweeps in Fig. 7.6 b) show that the ESR signal has changed from an asymmetric lorentzian to an asymmetric fano-like resonance. It is difficult to be certain of why this change occurs, as the full ESR-STM mechanism is not currently understood,

but it is likely due to an unintended change in the detection scheme caused by switching the machine between HF and LF regime. This is something that we will study in the future by adding the frequency range from 20 GHz to 60 GHz into our machine. This way we will be able to study the behaviour of the ESR signal continuously from the HF to LF regime and see where the transition from a peak to an fano-like resonance occurs. Measurements on TiH_{OO} in the LF regime were only performed at two ZEs and two set points so a full *g*-factor and tip field analysis is not performed due to the large error we would expect. Changing the ZE did not change the behaviour of the bias-magnetic sweep significantly and increasing the set point caused a larger shift in the ESR signal similar to the behaviour we see in Fig. 7.2 and Fig. 7.3. As these two behaviours are similar to the HF regime and because the ESR signal is still linearly dependent on the bias, we assume the fundamental physics that causes this linear shift is the same in the HF and LF regime. Any changes in the RF background and shape of the resonances are attested to the change in the measurement set-up. This change in the RF background and shape of the ESR signal brings about an interesting notion about the difference between our HF and LF driving. In principle they result in the same thing, an alternating bias applied in our junction. The change in our ESR signals between the two set-ups suggests that these two are not equivalent. To confirm this hypothesis, a more in depth understanding of the ESR-STM mechanism has to be formulated that can explain the shapes of ESR signals that have been measured by us and by other groups, and can explain the background RF signal that can be picked up off resonance. If we can understand the reason why certain resonances are shaped the way they are, we can then possibly understand the differences between our HF and LF set-ups based on the shapes of the ESR signals they provide.

7.1.4 Bias Dependent Electron Spin Resonance on Dimers

After observing this direct control of ESR transitions we wanted to investigate the possibilities of using this phenomenon to control spins in a meaningful way. To do this we measured bias-magnetic sweeps on TiH dimers. The goal was to tune two ESR transitions from a regime where their Zeeman splittings were equal to a regime where they are not. Fig. 7.7 shows a bias-magnetic sweep on a TiH_{OO}-TiH_{OO} dimer and ESR sweeps at 50 mV and 190 mV. We see three transitions, indicated by the white dashed lines in Fig. 7.7 a) and the black arrows in Fig. 7.7 b) and c), which are indicative of the singlet-triplet ($S \rightarrow T_0$) transition and the two triplet-triplet ($T_0 \rightarrow T_+$, $T_0 \rightarrow T_-$) transitions for strongly coupled dimers ($r = .674$ nm, $J \approx$ 45 GHz) [6]. Comparing Fig. 7.7 b) and c) we can already see a change in behaviour of the ESR sweep at different biases and an indication of different spacing between ESR peaks but this

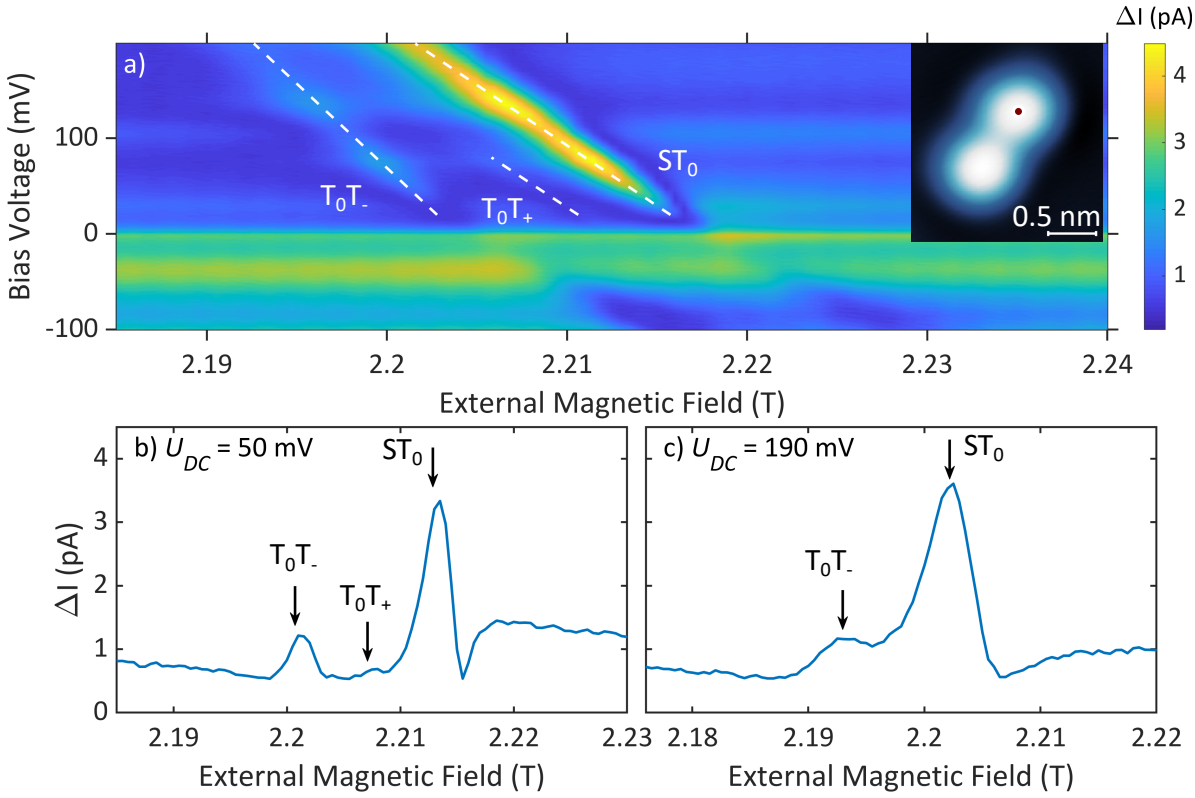

Figure 7.7: a) Bias dependent ESR sweep measured on a TiH_{OO}-TiH_{OO} dimer ($U_{SP} = 100$ mV, $I_{SP} = 200$ pA, $U_{RF} = 20$ mV, $f = 61.545$ GHz). White dashed lines are a linear fits to the ESR peaks. Dimer topography is inset on the top right of the panel with the red dot indicating the position of the tip during the measurement ($U_{DC} = 100$ mV, $I = 20$ pA). b-c) ESR sweeps at $U_{DC} = 50$ mV and $U_{DC} = 190$ mV respectively (same data and parameters at panel a)). Arrows indicate position of ESR peaks.

will be investigated and analyzed further in the next section along with other bias-magnetic sweeps on dimers.

7.1.5 Effect of Changing Spin Centers and Tips

As a final consistency check we also performed bias-magnetic sweeps on three different TiH_{OO} and TiH_{O} molecules. Fig. 7.8 presents these sweeps and shows that there are no major differences between measurements on the same species. Changing tips also did not significantly affect the behaviour of bias-magnetic sweeps, although full data sets with four ZEs and four set points were only performed with one tip.

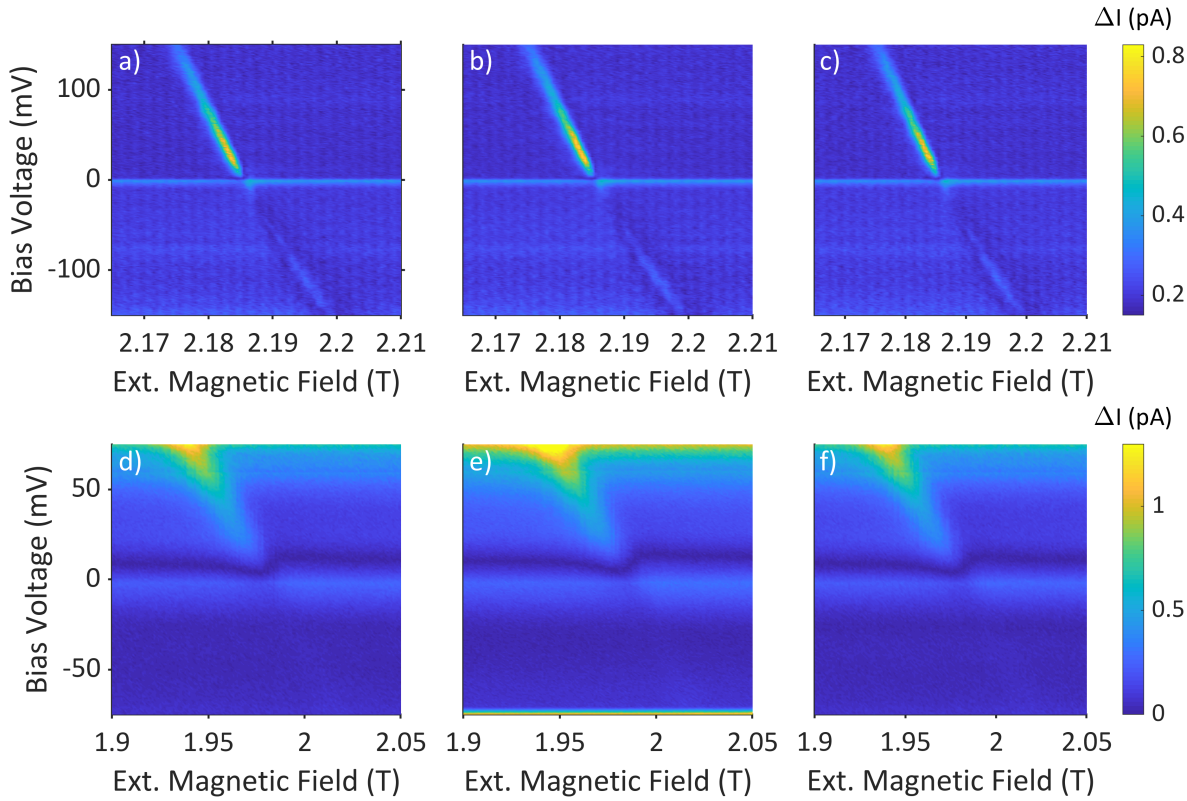

Figure 7.8: a-c) Bias dependent ESR sweeps measured on three different TiH_{OO} molecules ($U_{SP} = 100\,\text{mV}$, $I_{SP} = 100\,\text{pA}$, $U_{RF} = 12\,\text{mV}$, $f = 61.545\,\text{GHz}$). d-f) Bias dependent ESR sweeps measured on three different TiH_{O} molecules ($U_{SP} = 100\,\text{mV}$, $I_{SP} = 50\,\text{pA}$, $U_{RF} = 25\,\text{mV}$, $f = 19\,\text{GHz}$).

7.2 Analysis and Discussion

7.2.1 Bias Dependent ESR-STM Mechanism

Extracting g-Factors and Tip Fields

The main analysis that we performed on the measured data sets was the extraction of *g*-factors and tip fields as a function of the bias. This is very similar to what was shown in Fig. 6.4 d) with the addition of performing a spline fit to ESR signals measured at varying biases. To perform this spline fit we must first extract the positions of the ESR signals which is done by fitting the ESR signal with a fano resonance in the positive bias (20 mV to 150 mV) and by finding the peak maximas at negative bias (-20 mV to -150 mV). If we take a look at any of the bias-magnetic sweeps presented in this chapter, we see that near zero bias the ESR signal disappears and we are not able to find the peak positions. We overcome this shortcoming by performing an interpolated spline fit over the full bias range using the ESR positions we found at biases away from zero bias. This fit over the full bias range is shown as a white dashed line in Fig. 7.9 a). The assumption here is that even though the ESR signal is not visible in certain bias regions, this disappearance is due to low currents. Therefore, we assume the resonance does exist there we are just not able to detect it. Fig. 7.9 b) shows the linear fits to the bias dependent ESR signals. Each colored line in Fig. 7.9 b) is an interpolated spline fit demonstrated in panel a) and the dotted and dashed lines are linear fits to ESR peaks at two biases. By performing this procedure at all biases we can then extract the dependency of the linear fit on bias, and therefore the dependency of the *g*-factor and tip field on the bias. This was done at four set points and the results are shown in Fig. 7.10.

In the case of extracting the ESR peak positions on the Ti_O molecules a spline fit was not performed. This is due to the fact the ESR peak is not visible in the negative bias range, and therefore there are no empty regions that have to be connected as in the case of the Ti_{OO} data. The analysis is then simplified as we make a linear fit to the ESR peak positions in the positive bias range (from 20 mV to 80 mV). We then followed the same procedure as shown in Fig. 7.9 b) and extracted the bias dependencies of the *g*-factor and tip field at four current set points.

The extracted bias dependencies of the *g*-factor and tip field of both the TiH_{OO} and TiH_O molecule are presented in Fig. 7. 7.10 a-d) with the left column pertaining to the TiH_{OO} analysis and the right column pertaining to the TiH_O. We see that for both molecules both the tip

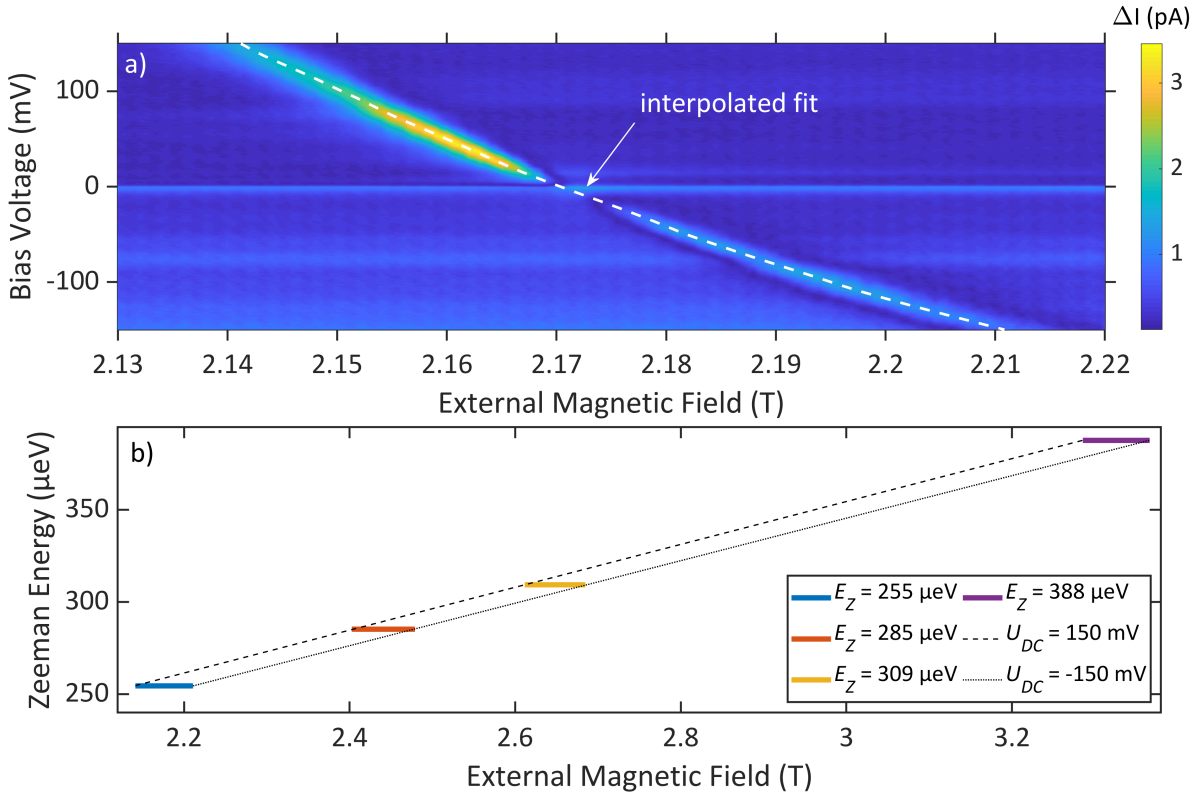

Figure 7.9: a) Bias dependent ESR sweep with a spline fit to the ESR peak positions ($U_{SP} = 100\,\text{mV}$, $I_{SP} = 250\,\text{pA}$, $U_{RF} = 20\,\text{mV}$, $f = 61.545\,\text{GHz}$). White dashed line indicates spline fit to ESR peak positions. b) Demonstration of the linear fits to multiple bias dependent ESR sweeps. The four colors show four spline fits at four ZEs (extraction of spline fit for one ZE was demonstrated in panel a)). Dashed line shows linear fit to the four spline fits at $U_{DC} = 150\,\text{mV}$. Dotted line shows same as dashed line but at $U_{DC} = -150\,\text{mV}$.

field and *g*-factor have dependencies on the bias. In the case of TiH_{OO} increasing the bias increases the *g*-factor and the tip field of the system. The dependency also seems to be roughly linear in the positive bias regime and then changes to be non-linear in the negative regime. Furthermore, increasing the set point also increases the *g*-factor and tip field. Increasing the set point will change the tip field but the change in the *g*-factor is not something that has been observed experimentally. Looking at the results for the TiH_O molecule we see that the tip field behaves in a similar way to the case of the TiH_{OO} molecule although the tip field is much stronger and the bias dependency is much stronger. This is very likely due to the tip being closer to TiH_O than the TiH_{OO} species even at similar set points, which is a result of the smaller DOS in the TiH_O at the set point bias ($U_{SP} = 100\,\text{mV}$). In contrast to the TiH_{OO} molecule, the *g*-factor of the Ti_O molecule does not seem to always increase with the bias voltage. In fact there seems to be some transition from low to high set point, where at lower

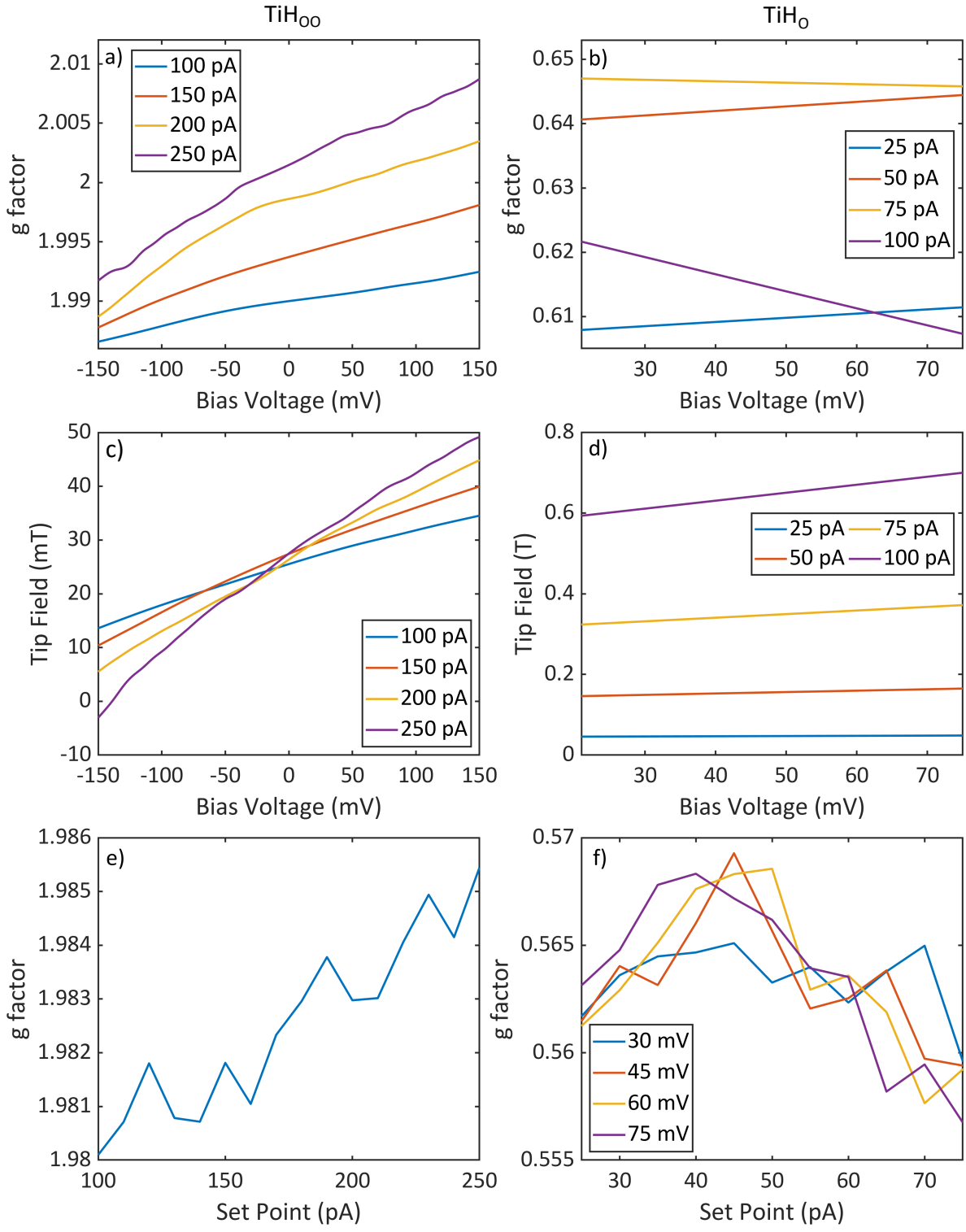

Figure 7.10: a) Extracted bias dependencies of the g-factor in TiH_{OO} at four set points. b) Extracted bias dependencies of the g-factor in TiH_O at four set points. c) Extracted bias dependencies of the tip field measured on TiH_{OO} at four set points. d) Extracted bias dependencies of the tip field measured on TiH_O at four set points. e) Extracted set point dependent *g*-factor in TiH_{OO} at one bias ($U_{DC} = 100\,\text{mV}$). f) Extracted set point dependent *g*-factor in TiH_O at four biases.

set points the *g*-factor increases with bias and at higher set points the *g*-factor decreases with bias.

To further investigate the *g*-factor transition measured on the TiH_O molecule we measured ESR signals at sixteen set points and four ZEs for both TiH_{OO} and TiH_O, and extracted the *g*-factor at those sixteen set points. For the case of TiH_O we performed this measurement at four biases. Fig. 7.10 e) and f) shows the behaviour of the *g*-factor in TiH_O and TiH_{OO} as a function of set point. We see that for TiH_{OO} the *g*-factor increases with decreasing tip sample distance. What kind of dependency is being observed is difficult to say due to the large error of our data, but we believe it is related to the exponential dependence of the current on the tip sample distance. We will be investigating this interpretation and decreasing the error in our data by repeating these measurements at more ZEs. For the case of the TiH_O molecule, there is clearly a regime were the *g*-factor increases with increasing set point and a regime where the inverse happens. We also see an indication that this transition from increasing to decreasing *g*-factor has some dependency on the bias voltage (this is further validated in Fig. 7.10 b)), but this has to be confirmed by further measurements. Similarily to the TiH_{OO} measurements we plan to repeat measurements on TiH_O at more ZEs.

Bias Control of Molecule z-Displacement

When looking at the given data and analysis one of the most obvious interpretations might be a Stark shift [91]. This interpretation would be that the dipole moment of the TiH molecule is effected by the electric field from the tip and this would change the ESR signal of the molecule. This interpretation is disregarded as we have no good evidence that there is a change in the dipole moment between the excited and ground spin state of the TiH molecule. That is to say, the dipole moment may shift the whole spectrum (which would difficult to study), but as there is no relative change between the excited and ground state the ESR signal should stay the same. Fortunately, there is a more likely interpretation proposed in Ref. [28] which suggests that a z-displacement of the TiH molecule can modulate the *g*-factor. The analysis and data presented in this chapter is compared to this interpretation to check its validity.

To understand this interpretation we have to first understand why a change in the bias would result in a change in the TiH z-position, and to understand that we have to consider the forces acting on the molecule while in the junction. In our simple model we consider the electric force acting on the molecule, which is a result of the electric field in the junction, and the elastic force acting on the molecule from the substrate. A schematic of the STM junction along

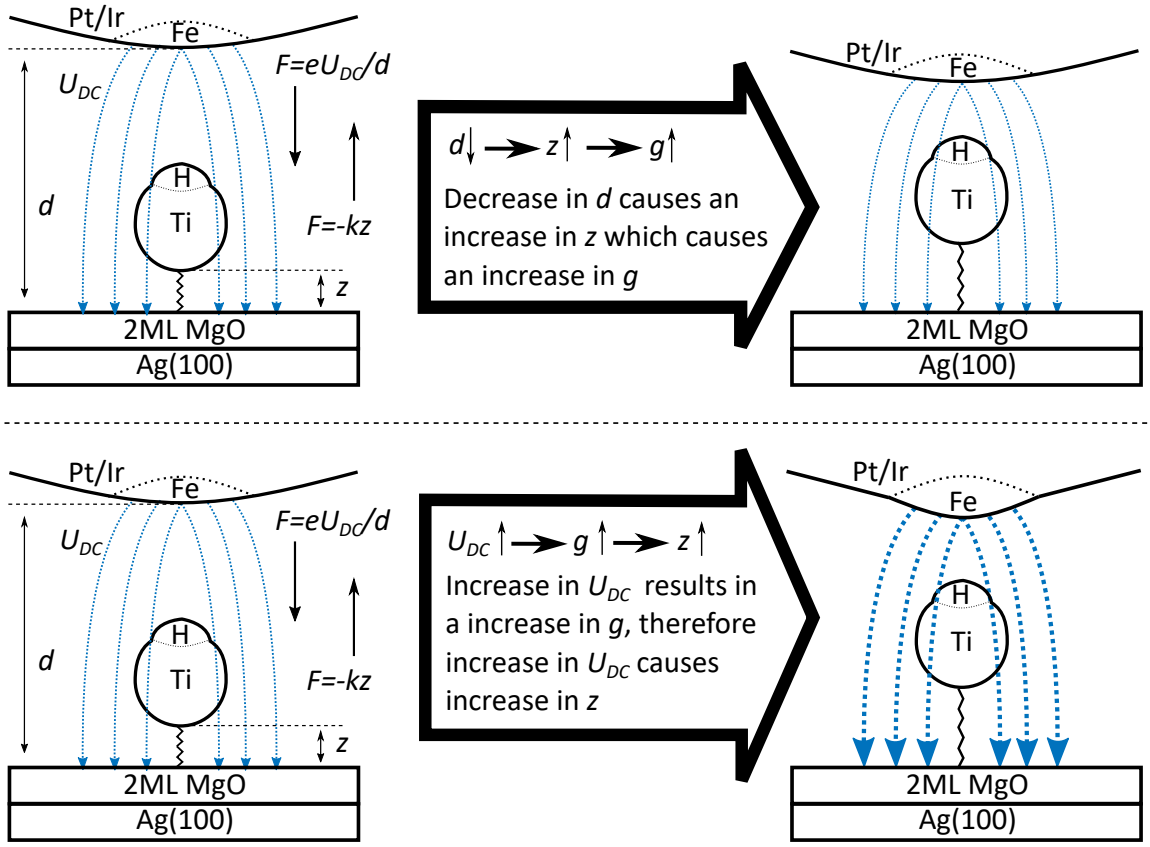

Figure 7.11: Schematic representation of forces acting on the TiH molecule in the STM junction. Top half shows the effect of changing the tip sample distance on the z-position of the molecule. We interpret this z-movement to cause the *g*-factor to change. Bottom half shows how the bias changes the z-position of the molecule along with our interpretation of how the bias changes the *g*-factor.

with these opposing forces can be seen on the top and bottom left of Fig. 7.11. Here d is the tip sample distance, z is the TiH molecule distance from the substrate, k is the elastic constant of the TiH-substrate bond and U_{DC} is the bias voltage applied. Our initial interpretation and model forgoes the atomic force of the tip acting on the molecule, as this force is relatively small at low tip sample distances (which is the case for most of our experiments). On the other hand, we observe certain behaviours which we speculate could be due to the atomic force acting on the tip, and we will be building on this interpretation in the future. For this dissertation, we find that considering only the electric force and the elastic force is sufficient enough to understand the majority of our data. When we equate the electric force and the elastic force from the substrate, we can find that z is linearly dependent on U_{DC} and inversely

dependent on d as seen in Eq 7.1.

$$z = -\frac{eU_{DC}}{kd} \tag{7.1}$$

First, let us consider the effect of d on z. We know from literature that z should increase as d decreases (at least in the regime of the experiment) [96]. Looking at Fig. 7.10 a), which shows that the g-factor increases with a decrease in d, we can make the conclusion that an increase in z increases the g-factor (why this is the case is explained in the next subsection). This is schematically represented in the top half of Fig. 7.11. Now comparing this to the bias's effect on z we can make a similar analogy. That is to say, knowing that a z increase causes an increase in the g-factor and the g-factor increases with U_{DC}, we can conclude that an increase in U_{DC} pulls the TiH molecule from the substrate. This is schematically represented in the bottom half of Fig. 7.11. This is further corroborated by comparing the data at different set points. We can see in Fig. 7.10 a) that as d decreases the effect of U_{DC} on the g-factor is stronger and therefore stronger on z. This is in agreement with what can be expected from Eq. 7.1.

We can also understand the relationship between the tip field and bias using this framework. As increasing the bias pulls on the molecule, this change in position will cause the molecule to feel a larger tip field from the Fe on the tip as the molecule is now closer to the Fe. In addition, another effect is likely taking place similar to the movement of the TiH molecule. The Fe atom on the tip is also under the influence of electric and elastic forces and will move when the bias increases or decreases. If the Fe atom moves more closely to the spin then the tip field felt by the system will also increase. How strong or weak this effect is, is difficult to quantify and is beyond the scope of this work, but we might be able to investigate it using spatially resolved ESR-STM that probes the dipole moment of the tip [109]. The tip field analysis is Fig. 7.10 c) also shows something interesting when comparing the measurements performed at different set points. We see that the individual data sets for each set point intersect with each other around zero bias. This is quite strange as it means that a movement of the tip at zero bias does not change the tip field. Furthermore, at negative biases bringing the tip closer to the sample decreases the tip field and can even result in a zero tip field. This is not yet fully understood but our initial explanation is that it has to do with the direction of the tip magnetic field rotating with respect to to the quantization axis of the ESR signal. It is also possible, and in fact very likely, that features of this can change when the tip changes.

What was previously discussed is in agreement with what is observed on the TiH_{OO} molecule but in the case of TiH_O there are some extra details. The behaviour on TiH_O is similar to TiH_{OO} when the set point is small (d is large), but when d is small we see that the g-factor decreases with bias. The current interpretation is that a regime is reached where an increase in the bias voltage starts to push the molecule into the sample due to a change in Eq. 7.1 caused by the atomic force from the tip becoming non-negligible (we know from the previous analysis that a movement of the molecule into sample lowers the g-factor). This would be consistent with the set point dependency on z, as z can decrease with a decrease of d if d is small enough [96]. Although this is the current interpretation, further data has and will be taken to further understand and confirm this model. In regards to the tip field behaviour on the TiH_O, the interpretation is the same as for the TiH_{OO} molecule although it is not possible to confirm if the behaviour is the same at negative bias. As previously stated, the tip field is stronger due to the tip being closer to the TiH_O molecule during measurements.

g-Factor Dependency on the Molecule z-Displacement

Understanding why and how the z-displacement of the molecule can affect the g-factor is the final piece in interpreting bias dependent ESR-STM. This is presented thoroughly in Ref. [28] and what is shown here is a summary based on the aforementioned work. We start with the model Hamiltonian for the system, (Eq. 7.2), which considers the crystal field anisotropy (F_c, D), spin orbit coupling (Λ) and Zeeman splitting. Furthermore, this Hamiltonian works both on the angular momentum operator (l) of the electron found in the $d_{x^2-y^2}$ orbital and the spin (S) of this electron.

$$H = -|D|l_z^2 + F_c((l^{(+)})^4 + (l^{(-)})^4) + \Lambda\tilde{S}\cdot\tilde{l} + \mu_B\tilde{B}\cdot(g\tilde{S} + \tilde{l}) \tag{7.2}$$

Diagonalizing this Hamiltonian and performing a Taylor expansion can lead to the following dependency of g on F_c:

$$\frac{\partial g_z}{\partial F_c} = -\frac{2304\Lambda F_c}{(576F_c^2 + \Lambda^2)^{3/2}}. \tag{7.3}$$

Here the subscript on the g-factor refers to the quantization axis of the measurement which in our case is always in the z-direction. This result leads us to expand the term $\delta g_z/\delta z$ using

the chain rule:

$$\frac{\delta g_z}{\delta F_c} = (\frac{\partial g_z}{\partial F_c}\frac{\partial F_c}{\partial z}). \tag{7.4}$$

From here all the pieces are available to be put into this equation. δz is given in Eq. 7.1, $\partial g_z/\partial F_c$ is given by Eq. 7.3, and $\partial F_c/\partial z$ can be estimated using DFT [28]:

$$\delta g_z = (\frac{\partial g_z}{\partial F_c}\frac{\partial F_c}{\partial z})\delta z = \frac{2304\Lambda F_c}{(576F_c^2+\Lambda^2)^{3/2}}\frac{\partial F_c}{\partial z}\frac{eU_{DC}}{kd}. \tag{7.5}$$

In the case when $\partial g_z/\partial F_c$ and $\partial F_c/\partial z$ are not dependant on z (this is assumed in Ref. [28]), the *g*-factor will change linearly with bias because the z-displacement changes linearly with bias. This seems to be the case at positive biases as the behaviour is linear for both TiH_{OO} and TiH_O. On the other hand when going to negative bias the behaviour deviates from being linear. The current hypothesis is that in this regime the molecule starts be pushed and "tilted" into the sample due the reversal of the electric field. That is to say when the molecule is pulled at positive bias, both the Ti and H are moved directly in the z-direction (very likely by different displacements but this is difficult to quantify). When the molecule is in a negative bias, the field causes the TiH to tilt into the sample. This is shown schematically in Fig. 7.12. At this point $\partial g_z/\partial F_c$ and $\partial F_c/\partial z$ may have some dependency on z which is why the data shows a non-linear behaviour. It is important to note that this is currently just a hypothesis but it seems to agree with all the other findings of this experiment. Furthermore, it is difficult to

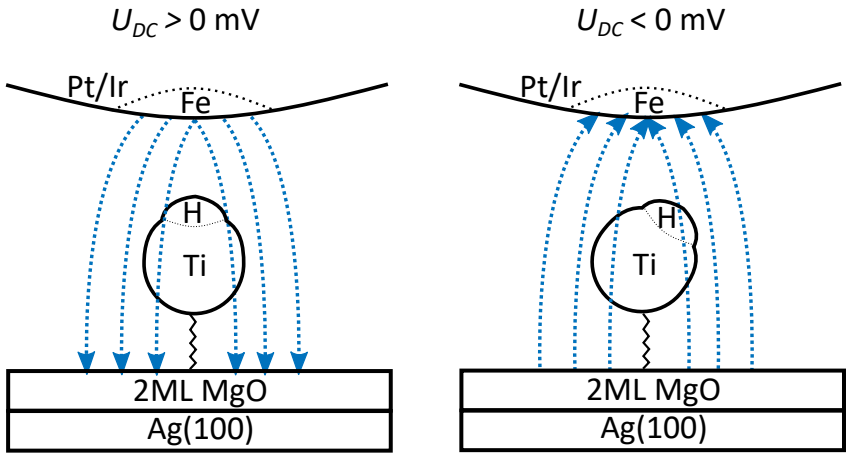

Figure 7.12: Schematic of the TiH molecule geometry in the junction at positive and negative bias.

probe $\partial g_z/\partial F_c$ and $\partial F_c/\partial z$ experimentally therefore more detailed models would have to be created to confirm our interpretation .

7.2.2 Bias Dependent Electron Spin Resonance on Dimers

Initial Experiments and Interpretation

Fig. 7.13 shows the three bias-magnetic sweeps we performed on TiH-TiH dimers as a proof that the bias can be used to control separate spin transitions. Two dimers were tested whose topographies are shown in the inlets of Fig. 7.13 a) to c) where the red dot represents the positions of the tip during the measurement. Fig. 7.13 a) and b) show experiments performed on the same dimer at two different set points ($U_{SP} = 100$ mV, $I_{SP} = 200$ pA and $U_{SP} = 150$ mV, $I_{SP} = 1$ nA) where in both cases we see distances between different transitions changing depending on bias. Here the white dashed lines represent linear fits to ESR peaks and the dotted lines represent linear extrapolations. For the lower set point experiment we find the distance between the ST_0 transition and the T_0T_- transition changes from $\Delta B = 14.3$ mT at $U_{DC} = 20$ mV to $\Delta B = 10.2$ mT at $U_{DC} = 200$ mV. When measured at a higher set point we see that all three transitions seem to merge; the transitions here being separate at low bias and combined at high bias. For the second dimer we see a different behaviour with only two transitions whose distance does not change considerably with bias. To understand the observations presented in Fig. 7.13 we have to start with the model Hamiltonian for a coupled spin system [104, 111]:

$$H = -\mu_B(B_{ext} + B_{tip})g_1\hat{S}_1^z - \mu_B B_{ext} g_2 \hat{S}_2^z + J\hat{S}_1 \cdot \hat{S}_2 + D(3\hat{S}_1^z\hat{S}_2^z - \hat{S}_1 \cdot \hat{S}_2). \qquad (7.6)$$

Here B_{ext} and B_{tip} are aligned with z and the first two terms are the Zeeman splittings of the individual molecules in the dimer. The third term is the Heisenberg exchange interaction with the strength of J, and the fourth term is the dipole interaction of the two molecules with the strength of D. Lastly, μ_B is the bohr magneton, $\hat{S}_1$ is the spin operator of the molecule below the tip, $\hat{S}_2$ is the spin operator for the other molecule and g_1 and g_2 are the g-factors of the two molecules respectively. Working in the basis of the combined $\hat{S}_1^z\hat{S}_2^z$ states ($|\uparrow\uparrow\rangle, |\downarrow\uparrow\rangle, |\uparrow\downarrow\rangle, |\downarrow\downarrow\rangle$), known as the Zeeman product states, we can diagonalize the Hamiltonian and find that the eigenstates for the low energy and high energy triplet states to be simply

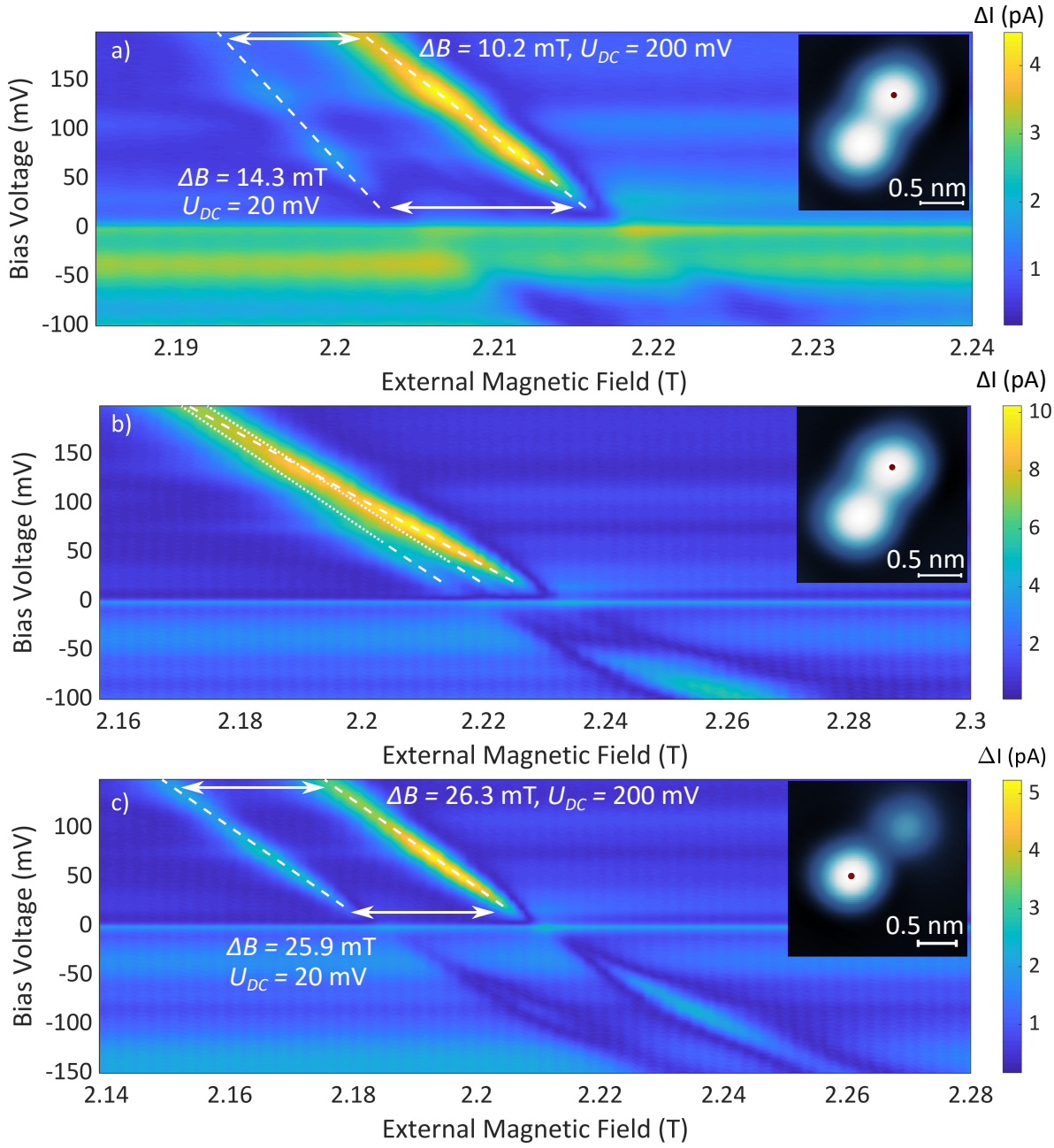

Figure 7.13: Bias dependent ESR sweeps for a TiH_{OO}-TiH_{OO} dimer (a-b) and a TiH_{OO}-TiH_{O} dimer (c). Topographies are displayed as insets in the panels with a red dot indicating the position of the tip during measurements ($U_{DC} = 100\,\text{mV}$, $I = 20\,\text{pA}$). a) ($U_{SP} = 100\,\text{mV}$, $I_{SP} = 200\,\text{pA}$, $U_{RF} = 20\,\text{mV}$, $f = 61.545\,\text{GHz}$). White dashed lines are linear fits to the ESR peaks and the distance between fits is indicated at 200 mV and 20 mV ($\Delta B = 10.2\,\text{mT}$ and $\Delta B = 14.3\,\text{mT}$ respectively). b) ($U_{SP} = 150\,\text{mV}$, $I_{SP} = 1\,\text{nA}$, $U_{RF} = 20\,\text{mV}$, $f = 61.545\,\text{GHz}$). White dashed lines are a linear fits to the ESR peaks and dotted lines are linear extrapolations. c) ($U_{SP} = 100\,\text{mV}$, $I_{SP} = 300\,\text{pA}$, $U_{RF} = 20\,\text{mV}$, $f = 61.545\,\text{GHz}$). White dashed lines are a linear fits to the ESR peaks and the distance between fits is indicated at 200 mV and 20 mV ($\Delta B = 26.3\,\text{mT}$ and $\Delta B = 25.9\,\text{mT}$ respectively).

$|T_+\rangle = |\uparrow\uparrow\rangle$ and $|T_-\rangle = |\downarrow\downarrow\rangle$, while the middle triplet state and singlet state are found to be:

$$\begin{aligned} |T_0\rangle &= \cos(\theta/2)|\uparrow\downarrow\rangle + \sin(\theta/2)|\downarrow\uparrow\rangle \\ |S\rangle &= \sin(\theta/2)|\uparrow\downarrow\rangle - \cos(\theta/2)|\downarrow\uparrow\rangle. \end{aligned} \tag{7.7}$$

Here, $\theta = \arctan(1/|\eta|)$ and η is the ratio between the energy detuning, which is the difference in the ZSs between the molecules ($\mu_B(g_1(B_{ext} + B_{tip}) - g_2 B_{ext}$), and the flip-flop coupling ($J - D$). When η is largely negative or positive, the eigenstates in Eq. 7.7 approach the states described by the Zeeman product states and when η is near zero the eigenstates approach the linear superposition of states as defined in Eq. 7.7. The latter is the case for the data shown in Fig. 7.13 a) and b), which is why we see three transitions, and the former is the case for Fig. 7.13 c), which is why we see two transitions ($\Delta E_1 = E_{\uparrow\uparrow} - E_{\downarrow\uparrow}$, $\Delta E_2 = E_{\uparrow\downarrow} - E_{\downarrow\downarrow}$). This is further validated by our estimated flip flop coupling (186 µeV for the dimer in the top panels and 1.57 µeV for the dimer in the bottom panel) and energy detuning (2.32 µeV for panel a), 5.79 µeV for panel b) and 178 µeV for panel c)) which are based on literature values [114]. Now one might ask why we do not observe a fourth transition in the TiH_{OO}-TiH_{OO} dimer and that is due to the large exchange interaction estimated to be 242 µeV. When the exchange interaction is so large the energy of the singlet state becomes lower than the lowest energy triplet state allowing for only three transitions due to selection rules for the magnetic quantum number, $\Delta m = \pm 1, 0$. These transitions are shown schematically in an energy diagram presented in Fig. 7.14 b).

Modelling Bias Dependent Electron Spin Resonance on Dimers

Fig. 7.14 shows modelling that was performed to describe the behaviour observed in Fig. 7.13 b). Here all the colored transitions between different panels correspond to the same colored transitions in the other panels. The modelling was performed constructing a set of equations that can defined by equating the RF energy to the transitions energies (i.e. we take the difference between eigenenergies of different states and set them equal to the RF energy):

$$\begin{aligned} hf = E_{T_+} - E_{T_0} = \frac{1}{2}(J + 2D + \mu_B(g_1(B_{ext} + B_{tip}) + g_2 B_{ext}) \\ - \sqrt{(J-D)^2 + (\mu_B(g_1(B_{ext} + B_{tip}) + g_2 B_{ext}))^2}) \end{aligned} \tag{7.8}$$

$$hf = E_{T_0} - E_{T_-} = \frac{1}{2}(J + 2D - \mu_B(g_1(B_{ext} + B_{tip}) + g_2 B_{ext}) - \sqrt{(J-D)^2 + (\mu_B(g_1(B_{ext} + B_{tip}) + g_2 B_{ext}))^2}) \quad (7.9)$$

$$hf = E_{T_0} - E_S = \sqrt{(J-D)^2 + (\mu_B(g_1(B_{ext} + B_{tip}) + g_2 B_{ext}))^2} \quad (7.10)$$

We then estimate the magnetic field values at which the transitions occur at 0 mV and 200 mV based off the data presented in Fig. 7.13 b). By inserting these magnetic field values in our set of equations we can solve for values of g_1, g_2 and B_{tip} at both 0 mV and 200 mV. We then assume that the g-factors and tip field change linearly from 0 mV to 200 mV and then reverse

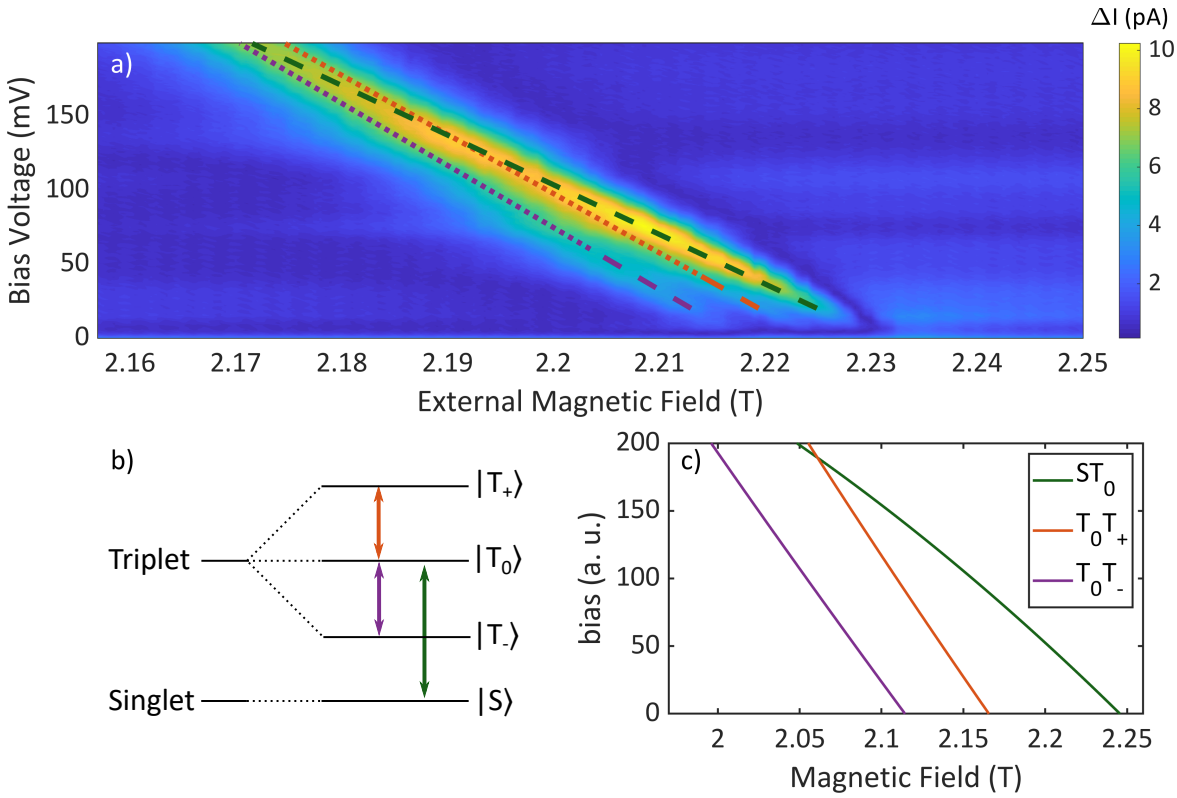

Figure 7.14: Colors of transitions in each panel are representative of the same transitions in each other panel. a) Bias dependent ESR sweeps on a TiH_{OO}-TiH_{OO} dimer ($U_{SP} =$ 150 mV, $I_{SP} = 1$ nA, $U_{RF} = 20$ mV, $f = 61.545$ GHz). Dashed lines are linear fits to the ESR peaks and dotted lines are linear extrapolations. b) Schematic energy level diagram for dimers with a large interaction energy ($J > E_Z$). In this case the singlet state becomes the ground state. c) Modelled ESR transitions showing the behaviour observed in panel a).

the process solving for B_{ext} using the g_1, g_2 and B_{tip} found at each bias. We assume this change in the *g*-factors and tip field based off the analysis in the previous subsection. The result from the last step is shown in Fig. 7.14 c). We find good agreement but not precise agreement which we account to the neccesity for us to estimate the dipole coupling and exchange interaction. With this demonstration we believe we can conclusively say that we used the bias to control different transitions at different rates. It is important to note that not all dimers will behave in this way as seen with the dimer in Fig. 7.13 c). Here the spin transitions are equidistant over bias as the changing tip field and changing *g*-factors will effect the energy of the transitions at the same rate.

Avoided Crossing in an Engineered Dimer

One of the ultimate goals for this project was to measure the avoided crossing in the coupled eigenstates of TiH-TiH dimers. This avoided crossing occurs when the energies of $|T_0\rangle$ and $|S\rangle$ approach each other, leading to transitions TT_+ and ST_- to approach each other. More specifically, this crossing occurs when the detuning energy η is equal to zero. At this point the two states are seperated by the flip flop energy $J - D$. This avoided crossing has been previously measured by adjusting the energies of $|T_0\rangle$ and $|S\rangle$ by changing the tip field which was done by varying the tip sample distance [104, 119]. Interestingly, this avoided crossing has been shown to be a regime where the two spins in the individual molecules are entangled and flip flop oscillations can be observed using pump-probe experiments. Knowing that the bias in ESR-STMs changes the tip field, we envisioned measuring this avoided crossing by using the bias as a tuning parameter.

Unlike the dimers that we previously presented, which where all found by chance on the sample, we had to design a dimer that would show an avoided crossing in the bias range and set point current we are interested in. If the molecules in the dimear are too close to each other then we can not access the avoided crossing due to the exchange interaction being too large. In this situation we would get a behaivour similar to dimer presented in Fig 7.13 and analyzed in Fig. 7.14. On the other hand, if the dimer is too largely seperated then the transitions we are interested in resolving become close in energy and they become difficult to resolve individually. We designed a dimer where the distance between molecules was 0.99 nm, which we estimate results in an exchange interaction of 1.5 GHz. The dimer was made using atom manipulation with the recipes for our manipulation presented in Chap. 2. Fig. 7.15 a) shows the avoided crossing measured using bias dependent ESR-STM with the white dashed lines positioned on the resonances. We also find that adjusting the tip sample

distance moves the avoided crossing up or down in bias. Specifically, if we lower the set point enough we can bring the avoided crossing to be near zero bias as seen in Fig. 7.15 b). Fig 7.15 c) shows how changing the initial current set point can move the transitions in the magnetic field axis. The avoided crossing we find is always at the same energy or magnetic field for any specific dimer (this fact comes from the behaivour of the eigenvalues of the states Eq. 7.7), so a movement of the three transitions in Fig. 7.15 c) is a direct demonstration that this crossing can be placed exactly at zero bias by fine tuning the tip sample distance. The origin of this movement must come from the small changes in g_1, g_2 and B_{tip} when adjusting the tip sample distance, which in turn will change the conditions for η. To confirm this interpretation we plan to study the behaivours of the *g*-factors and tip field in dimers

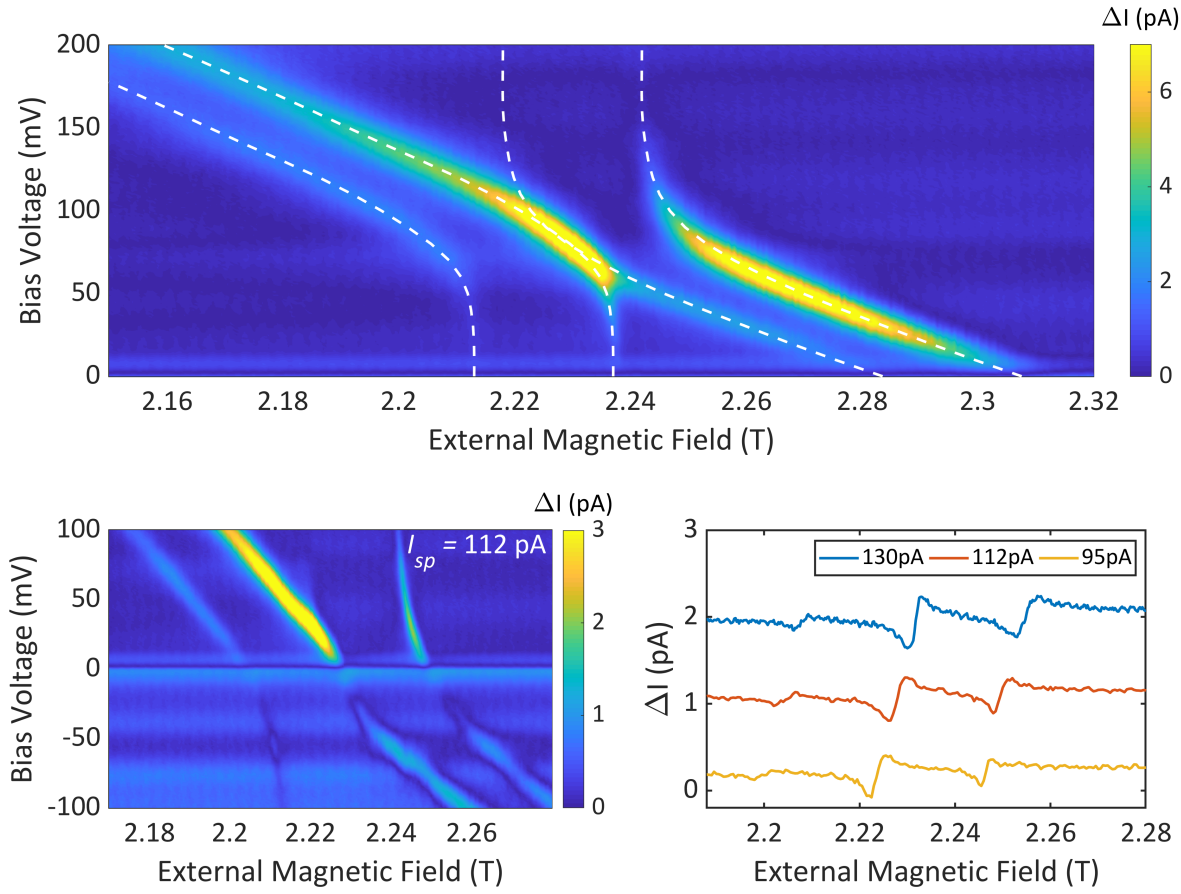

Figure 7.15: a) Avoided crossing of the singlet and triplet states measured using bias dependent ESR-STM ($U_{SP} = 100$ mV, $I_{SP} = 400$ pA, $U_{RF} = 20$ mV, $f = 61.545$ GHz). White dashed lines label the transitions. b) Bias-magnetic sweep showing the avoided crossing near zero bias ($U_{SP} = 100$ mV, $I_{SP} = 112$ pA, $U_{RF} = 20$ mV, $f = 61.545$ GHz). c) ESR sweeps at zero bias showing the movement of the ESR peaks when changing the initial current set point ($U_{SP} = 100$ mV, $U_{RF} = 20$ mV, $f = 61.545$ GHz). Data is offset for clarity.

more deeply in the future.

With the measurements presented in Fig. 7.15 and Fig. 7.13, we show conclusively how the bias can be used as a tuning parameter in ESR-STM experiments. In fact, we believe the bias has some advantages over other parameters such as the tip field. Importantly, the tip field is not a parameter that can be pulsed as the adjustment of the tip field needs a mechanical movement on the tip. The bias on the other hand is purely electronic and can be pulsed. For the purpose of ultrafast experiments, which are necessary in regards to quantum information processing, the bias gives a way to pulse the tip field. This gives us a larger control of ESR-STM systems as we can use the bias to pulse from a region were the spin states are entangled to disentangled. Previously, this could only be done by pulsing the driving frequency. Furthermore, we also show that we can place the entangled states at zero bias, which is also of interest for quantum computing. One of the main struggles for any quantum computing experiment is the coherence time of the states used as qubits. In ESR-STM a majority of the decoherence comes from the tunneling electrons [108]. As no electrons tunnel at zero bias, putting the entangled states at zero bias optimizes the coherence time between those states.

7.2.3 Deviations from the Tien-Gordon Model

One of the observations we posited at the beginning of this chapter is the fact that these bias-magnetic sweeps have some RF background signal off resonance. We wanted to gain some insight into this background by trying to model the behaviour. The most obvious analysis is to attempt is to try to replicate the background signal using the TG model which should, in theory, be the correct model. Fig. 7.16 shows slices of the background data at 2.24 T at four set points along with the TG modelling for each set point. One thing is immediately clear; the TG model perhaps can imitate certain features but the fine details are lost. Therefore, a more detailed theory has to be made to match the experimental results. One possibility is using a green's function formalism that considers electrons tunneling through a spin impurity and interacting with microwave radiation. Such a theory has the potential to be important as it could shine light onto how the ESR-STM mechanism functions and could even lead to a complete theory of the ESR-STM mechanism.

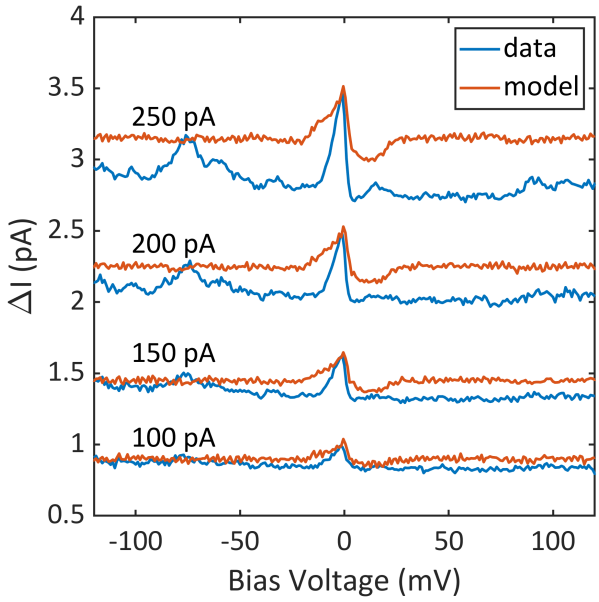

Figure 7.16: RF backgrounds of bias dependent ESR sweeps plotted along with expected behaviour based off TG interpretation. Presented at four current set points. RF backgrounds are taken at one magnetic field value. Data is offset for clarity.

7.3 Comparison with Bulk Electron Spin Resonance

Before concluding, we would like to take the oppurtunity to compare our experiments with bulk ESR experiments. In recent years several works have come out showing shifts in ESR signals caused by applying an electric field [51, 52, 53]. Similar to us, they find that their shifts are caused by crystal field terms being affected by the electric field. In contrast to our work, they have also found some systems where the spin-orbit coupling changes when an electric field is applied which in turn causes the spin transitions to shift. This is something to consider for the future of bias dependent ESR-STM as perhaps it would be possible to find a spin system whose spin-orbit coupling is modulated by the bias. When comparing our experiments to that of bulk ESR, we also see that our effect is stronger than what has been measured. For most materials it is very difficult to measure a shift past the natural linewidth of the ESR signal in bulk measurements. As we have seen, it is very easy to shift the ESR peak by tens, and even hundreds, of the natural linewidth in ESR-STM. This is very likely due to the different geometries in our experiments. Specifically, in STM experiments we can create large electric fields as we can bring the tip very close to the sample. Assuming a junction height of around 300 pm, and a bias of 100 mV, our junction would contain a field of 300 MV/m. In the case of bulk ESR, the experiments use plate capacitors to create their electric fields, whose spacing is macroscopic rather than nanoscopic, and we find fields on the order of 3 MV/m in

literature.

7.4 Conclusions and Outlook

What has been presented in this chapter is a good start in understanding the observations pondered in the second paragraph. On the other hand, a deeper analysis has also introduced new questions such as whether there is a transition in the TiH_O molecule from a regime where the bias causes the molecule to away from the substrate to one where it causes it to move towards the substrate. This one point should still be looked into by repeating the measurements in Fig. 7.10 e) and f) but increasing the quality. This will be done by measuring the ESR signal at more ZEs which would significantly decrease the error in the analysis. Another experiment that should be repeated and built upon is the observed change in th tip field with respect to bias (Fig. 7.10 c)). Again this measurement could be done at more ZEs to decrease error, and it could be performed along with spatially resolved measurements of the ESR peak at each bias. The ultimate purpose of these measurements would be to really see if a non-changing tip field near zero bias is a fundamental property of ESR tips (and therefore something that should be understood) or simply a feature of the particular tip that was used during the measurements of this dissertation. These measurements would also help explain what causes the change in the tip field as spatially resolved ESR-STM gives direct information on the dipole and/or exchange interaction between the tip and sample [109]. Lastly, the bias control of coupled dimers could be further investigated. We envision extracting the *g*-factor and tip field dependencies on the bias voltage for both the of the molecules in the dimer. Analysis of dimers in ESR-STM experiments generally assumes that the tip only functions on the molecule beneath the tip. This is likely not the case as the second atom of the dimer is probably close enough to feel the tip magnetic field and electric field in the junction. Modelling the *g*-factor changes in the individual molecules of a dimer could lead to a way to understand the different movements of the molecules caused by the tip. Furthermore, adjusting the dimer length would further add value to this project as we might be able to make a claim on the effect the distance from the tip has on the electric field and tip field felt by the molecule.

There is also one more aspect that could be understood better but at this point it seems to be a modelling problem rather than a problem with a lack of data. That is the question of the RF background that is off resonance from the ESR signal. Understanding this could help

explain the ESR mechanism itself and could perhaps shine light on why some spin species are ESR sensitive and others are not.

To conclude, we have demonstrated that spin transitions can be electrically controlled in an ESR-STM set-up. This effect was measured on the TiH species but should be a general effect for any species whose *g*-factor can be modulated by the crystal field or by spin-orbit coupling. We show that this effect is likely linear in the positive bias regime and deviates from a linear behaviour when approaching negative bias. We show that this is due the linear coupling between z-displacement of the molecule and the bias and speculate that the nonlinear behaviour arises when $\partial g_z/\partial F_c$ and $\partial F_c/\partial z$ starts being dependent on z. Furthermore, we show that this effect is far stronger in the ESR-STM than in bulk ESR which is likely due to the far larger electric fields we are able to produce. This effect also presents a new tuning parameter, similar to the tip field or current, for ESR-STM experiments as it can both be used to maximize the ESR signal and adjust eigenenergies of coupled spin systems.

8 Temperature Dependent Single Molecule Electron Spin Resonance

One of the initial goals when developing our ESR-STM was to probe the thermally induced transition from a fully initiated ground state to a mixed state. Not only is this a fundamental experiment, it is interesting for the field of quantum information processing as the controlled initialization of states is important in this framework [24]. Here we present initial results of experiments where we measured the ESR signal at ten ZEs and eight temperatures. We find that the baseline of the ESR signal is not entirely reproducible and that the tip changes the behaviour of the ESR peaks, making analysis challenging. We also find indication that initialization of the spin system starts near 1 K.

8.1 Different Tips at Base Temperature

During our experiment our tip changed several times causing us to start over; this gave us an opportunity to compare the behaviour of different tips at base temperature. What we see is that how the ESR peak changes with ZE is tip dependent (Fig. 8.1). Fig. 8.1 b) shows ESR amplitudes at various ZEs for two different tips and we see different behaviours for the two tips with respect to ZE. This is actually to be expected as the SP sensitivity of the tip is very likely magnetic field dependent [72]. The height of the ESR peak is also, of course, dependent on the RF driving amplitude, and an uncertainty in the amplitude would cause unwanted deviations in our measurements. As a consistency check we measured the transmission at a given frequency directly before each ESR sweep, and measured the RF response of the IETS on TiH_O right after each sweep. Fig. 8.1 c) shows the ten spectra that were measured directly after every ESR sweep for tip 2. We see that the data for all ten ZEs lie on top of each other assuring us that the RF amplitude is indeed the same over the ten ESR sweeps. This makes us more certain that what is being observed in Fig. 8.1 a) and b) is some change in the sensitivity of the ESR pick up mechanism. Fig. 8.1 a) also shows the tip might change the baseline of

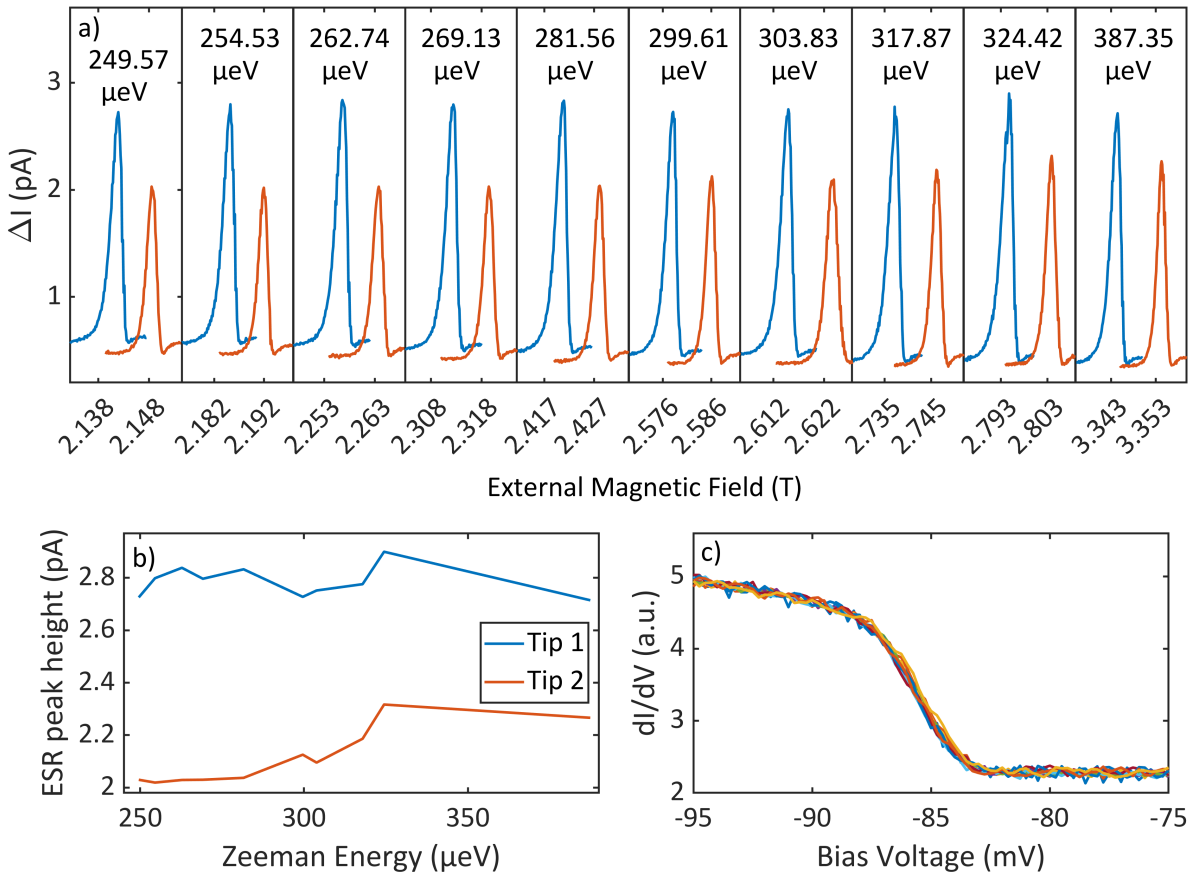

Figure 8.1: a) ESR signals measured with two different tips at ten ZEs ($U_{DC} = 100\,\text{mV}$, $I = 40\,\text{pA}$, $U_{RF} = 8\,\text{mV}$). Tip 1 is shown in blue and tip 2 is shown in orange. b) ESR peak heights of two tips at 10 ZEs extracted from data in panel a). c) RF response of the IETS in TiH_O at 10 frequencies ($U_{DC} = 100\,\text{mV}$, $I = 40\,\text{pA}$, $U_{RF} = 8\,\text{mV}$). Each measurement was done directly after measuring the ESR signal at the given frequency.

the measurement (although this is difficult to be certain of as we will see in the next section) and the position of the ESR signal changes slightly. This last effect is due to different tip fields from the two different tips. It is also important to note that although this measurement was performed at base temperature not each measurement is at the same temperature as the heating of the junction caused by the RF radiation is different for each frequency. This of course can lead to the question of whether the difference in the ESR peaks is due to something thermally induced. As there is no evident relation between the temperature and the height of the ESR peaks this is disregarded. Furthermore, it is very likely that in this regime the system is still initialized to the ground state which is discussed in the following sections. From the data presented in this section it is clear that the ZE dependent change in the ESR pick up sensitivity is non-negligible. As we are interested in measuring the change in the ESR peak

amplitudes at varying ZEs and temperatures we have to eliminate this effect in our analysis by normalizing our data to the peak height at base temperature.

8.2 Experimental Results and Analysis

The full experiment was performed by measuring ten ESR signals at ten ZEs at a given temperature. This is important as there often was maintenance (in the form of LHe filling or He^3 condensation) done on the machine in between each temperature. Fig. 8.3 shows the main results that came from this experiment. Only three ZEs are considered for clarity of data. One of the challenges that came with interpreting the measurements is that the baseline had a tendency to change from measurement to measurement. This is shown in Fig. 8.2 where the averaged baseline over ten ZEs is shown as a function of temperature (LHe filling events are also shown as dashed lines). As this baseline does not seem to be correlated to the temperature (nor any other parameter or operation that we can currently come up with) it is difficult to get an accurate analysis of the ESR signal versus temperature. Indeed, this is another reason why we would like to get a better understanding of how the RF background behaves in the previous chapter, as this might give us the answer as to why the baseline is so unpredictable during these temperature dependent measurements. Keeping this obstacle in mind, we plot the ESR heights both from the signal baseline and zero signal in Fig. 8.3 a) and b). The idea here is to compare analysis that eliminates deviations in the baseline with conventionally correct analysis. Furthermore, Fig. 8.3 c) and d) show the previous analysis normalized to the base temperature ESR peak heights. This is done to compensate for the magnetic field dependent tip pick up sensitivity investigated in the previous section.

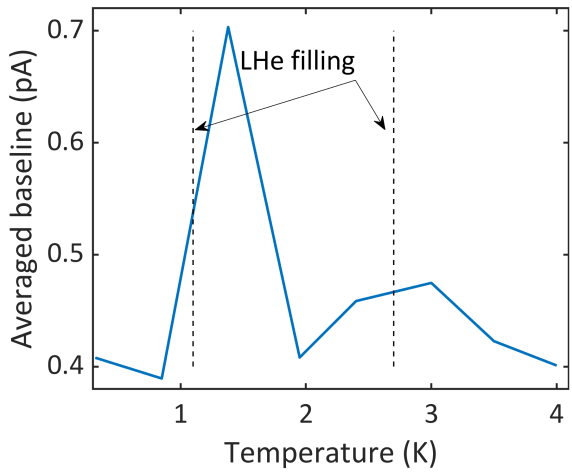

Figure 8.2: Baseline of the ESR signals averaged over ten ESR sweeps performed at each temperature. LHe filling occurences between measurements are shown with a dashed line.

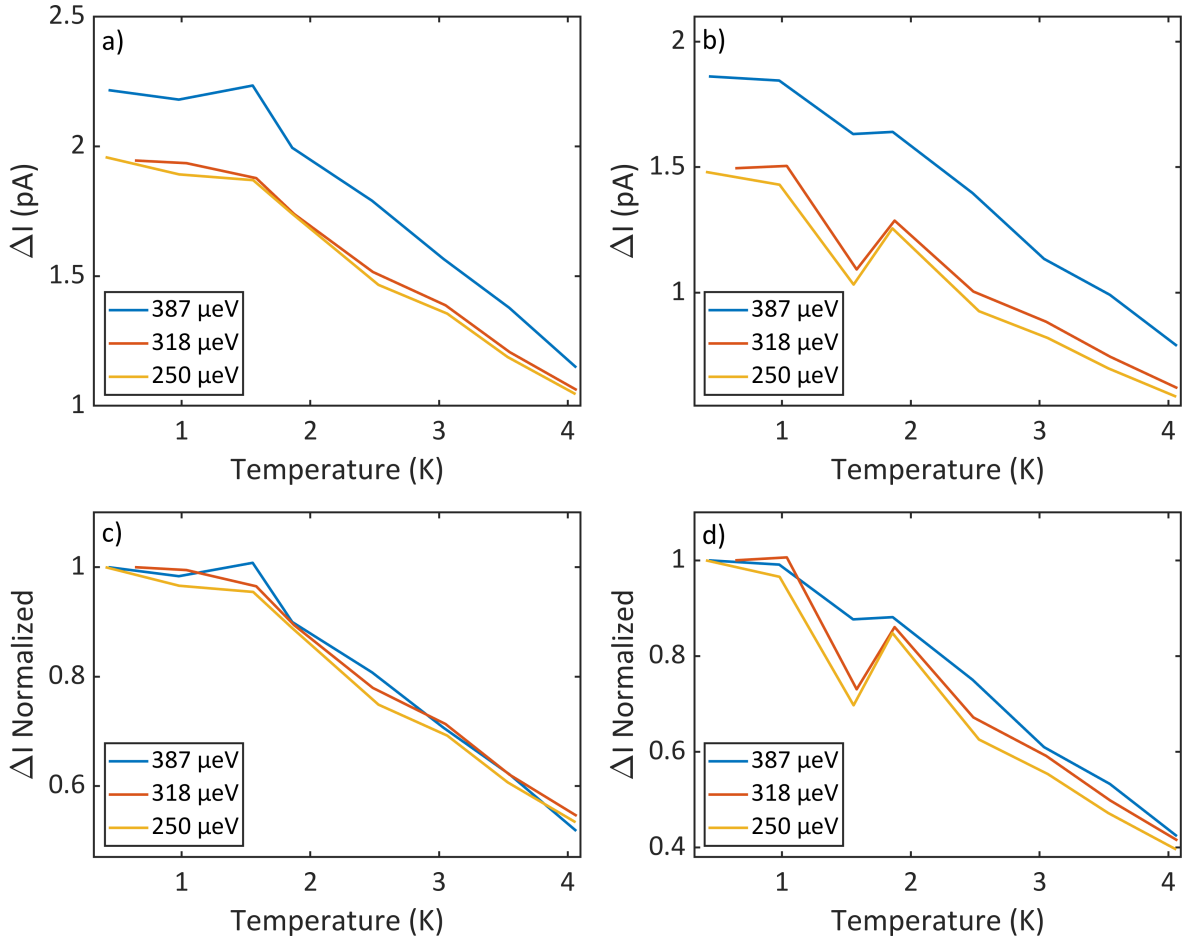

Figure 8.3: a) ESR peak heights at three ZEs measured as a function of temperature ($U_{DC} = 100$ mV, $I = 40$ pA, $U_{RF} = 8$ mV). Peak heights are taken from zero signal. a) ESR peak heights at three ZEs measured as a function of temperature ($U_{DC} = 100$ mV, $I = 40$ pA, $U_{RF} = 8$ mV). Peak heights are taken from the signal baseline. c) Data in panel a) normalized to the peak heights at base temperature. d) Data in panel b) normalized to the peak heights at base temperature.

Looking at the analyses, it is clear that the non-normalized data shows some temperature dependency, but there are also large differences in the ESR peak amplitudes between ZEs which we know is partially due to varying tip sensitivities when changin ZEs. On the other hand the normalized data seems to eliminate these tip effects and gives a clearer picture of how the temperature effects the ESR signal. From here we compare the two normalized data sets in Fig. 8.3 c) and d). In both cases the ESR peaks start to decrease around 1K, but the two analyses differ with respect to ZE dependency. Fig. 8.3 c) shows that in the analysis that considers the ESR peak height to be from zero signal, the dependency of the ESR peaks with respect to temperature does not change depending on the ZE. On the other hand, the analysis that considers the ESR amplitudes to be from the signal baseline, the dependency of the ESR peaks with respect to temperature does change slightly at different ZEs. The general trend is that for larger ZEs the ESR amplitude is larger at a given temperature. Due to the fact that we expect a change with respect to ZE and that in most experiments the peak height of a signal is from the baseline, we consider Fig. 8.3 d) to be the most correct analysis currently. Of course there is still a question of how the changing baseline introduces deviations into the data and therefore this analysis. It is clear that the data point at 1 K strongly deviates from the trend presented from the other data points.

With it in mind that Fig. 8.3 d) is the most correct analysis, we plot the analysis along with a simple model. This model is based on the Boltzmann distribution of a two level system and we can solve for the population of the ground state to be:

$$P_{\downarrow} = \frac{1}{e^{-\frac{E_Z}{k_B T}} + 1}. \tag{8.1}$$

We can adapt this to more closely describe our data by taking the difference between the ground state population and 0.5 (which is the population in resonance) and then normalizing the result to the 0 K value. The idea here is that in the experiment the peak amplitude is related to the difference between the resonant state and the thermally mixed state. With this simple model we can see in Fig. 8.4 that the trend of the data can be reproduced but there are some fine details that are not matched. Namely, the ZE does not have such a drastic effect on the population dyanmics as the model suggests. This could be accounted to errors in our experimental methodology, specifically the error in the temperature and the irreproducability of the baseline, or it could be accounted to a missing part of the model. For example, it has been demonstrated that state of the spin can be initialized with a SP current and this is not something that we currently consider [56, 113]. Fortunately though, the data does show one interesting thing in respect to the ZE. That is that the ZE does change at what temperature

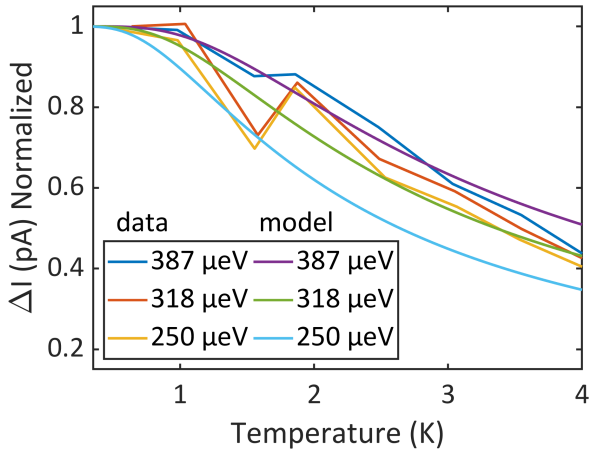

Figure 8.4: Normalized ESR peak heights at three different ZEs measured as a function of temperature ($U_{DC} = 100$ mV, $I = 40$ pA, $U_{RF} = 8$ mV). ESR amplitudes are taken from the signal baseline. Model based off the Boltzmann distribution is plotted alongside the data.

the ESR peak starts to decay, which indicates the ZE having an effect on the spin initialization. Although this seems to be the case, a model that can explain the behaviour in Fig. 8.4 more correctly is needed to confirm this interpretation.

8.3 Discussion

As shown in this chapter, measuring the thermal dynamics of an ESR signal comes with some challenges. First, it is shown that the signal intensity is tip dependent and not consistent over different magnetic fields. This is likely due to the magnetization of the tip being field dependent. Our method to eliminate this effect is by normalizing the data set to the base temperature. Second, we found that the baseline is not entirely reproducible between measurements, making analysis and interpretation difficult. To tackle this problem we consider the height of the ESR signals from the signal baseline and from zero signal. We see that the former analysis has some dependency on the ZE. As we expect some dependency on the ZE and because typically amplitudes of signals are considered from the baseline, we assume this analysis to be the most correct; to confirm the validity of this analysis the behaviour of the baseline should be better understood. This could be done phenomologically in a way that would let us redo the experiment presented in this chapter with a reproducible baseline. More preferably though would be to understand the origin of this baseline and this would be

in conjunction with understanding the behaviour of the RF background in the previous chapter. In either instance, measurements in this chapter should be repeated once the baseline can be reproducible.

The analysis and interpretation still have to be built on before we can make any conclusions, but there are some things that can be said based on the phenomenology of the data. The first is that below approximately 1 K the peak of the ESR signal is not noticeably temperature dependent and above 1 K the peak decays with respect to temperature. This suggests that around 1 K the initialization of the spin system starts to occur. The second feature that the data shows is that depending on the ZE the thermal decay of the ESR peak will start at a different temperature. Currently, this effect is rather small and should be measured again once the baseline is better understood. If this is confirmed then it is very likely that the change in the spin splitting of the system is being probed by the temperature dependent ESR sweeps. Indeed if this is the case, it may be possible to use a set of temperature dependent measurements as a thermometer. Of course, to further confirm this interpretation a more correct model has to be found which fits the data in Fig. 8.4. The modelling in Fig. 8.4 is a good starting point but something more has to be added. One proposal would be to include the initialization that occurs from the SP current. Another proposal would be to calculate the density matrix of a two level spin system and combine that with the thermal dynamics already proposed. Both proposals are beyond the scope of this dissertation.

9 Conclusions and Outlook

In this dissertation, we have shown the development of and first results from a state of the art ESR-STM. Our goal was to create an experiment that allows us to measure signals at far larger ZEs than what has previously been reported. As of the date of publication, we believe that we are the only group that can measure resonances above 40 GHz. We strived to this specific goal so that we could investigate two ideas. The first idea was to use the TM effect as a SP current source for ESR-STM experiments, and secondly we wanted to have an experiment where the spin is initialized to the ground state. Although we faced some obstacles with our first goal, which we have presented, we have successfully managed to implement a system that is capable of measuring high quality data and is now ready to be used as a tool for studying spin physics on the nanoscale. In this work, we have also presented the steps up to measuring an ESR signal and the initial experiments we performed with this new functionality.

The first project that we worked on after purchasing the machine and installing the HF components, was the measurement of the transfer function of our cabling using the RF response of spectroscopy measured in our junction. Due to the expertise in our group and the sharp states that superconducting gaps provide, we decided to use an SIS junction to accomplish this task. We successfully used the TG model to find the amplitude of the RF radiation that was confining into the apex of the STM tip. We found the dependency of this amplitude on the frequency of the radiation, to characterize our first transfer function. From there we also took the opportunity to use microwave-assisted tunneling as a way to study the different tunneling processes occuring in a superconducting junction. What we found is that the TG model breaks down at high conductances where many tunneling processes are present, and a more in depth model considering the tunneling Hamiltonian better describes the observations. This lead us to conclude that the seemingly seperate processes in SIS tunneling are not separate but interfere in a way that has to be considered at higher transmissions. With these initial investigations into microwave-assisted tunneling we inspired the creation of a new microwave-STM which is solely focused on this research. The initial goal of this ma-

chine is to excite a Shiba state by matching the Shiba energy to the microwave energy, and we believe that we have observed this effect recently.

The next project presented in this dissertation is the study of VOPcs on Pb(111). The goals of this project were to investigate the feasibility of the TM effect as a source of SP current and to expand ESR-STM experiments past atoms/molecules deposited on MgO. In both regards, we found significant challenges. The first challenge is the small RF amplitudes at which we would have to measure the ESR signal at if we wanted to use the TM effect. The second challenge is that the TM effect did not react while probing spin centers in our system. These two challenges would have to be overcome by increasing the sensitivity of the spin/ESR signal pick up mechanism. This could be done by either optimizing the creation of TM tips or by changing the sample system. In either regard, we do not currently plan to continue investigating the feasibility of using TM tips for ESR-STM experiments. Nevertheless, we found VOPc nanocrystals on Pb(111) to be a novel system with many unique features. Other groups have investigated Pcs on SCs, but what was new in our experiment was an addition of an out of plane atom protruding from our molecules. This lead to nanocrystals that have molecules with two orientations at each layer. We investigated these various orientations on the first and second layer, and found that some of them were magnetically and spin active while others were not. We speculate that the magnetically active species on the second layer has the same orientation as the magnetically active species on the first layer. Our experiments also directly show how the proximity effect of the superconducting Pb(111) is on a larger length scale than the screening of the electrons provided by a conducting Pb(111) surface.

In due course, we managed to measure ESR signals by using a sample system that has been shown to be effective by many groups. We show the ways we characterize the sample by identifying the different atomic and molecular species along with multilayer MgO. We also show the way we tip shape to create an ESR tip by looking for ESR candidate tips. Finally, we present ESR frequency sweeps above 60 GHz and magnetic field sweeps from 60 GHz to 98 GHz, showing definitively that our STM works in the operational frequency range we intended. A preference arises in doing magnetic field sweeps in our machine due to our sporadic transfer function and day-to-day changes in the transfer function. Lastly, we also investigate the changes in our transfer function that occur when changing the tip and after heating up and cooling down the machine. We find that both of these occurrences can cause significant changes that we combat by replacing the HF cabling at the junction during heat ups, and by using long tip wires. With the implementation of our machine, our specific outlook is either already presented in this thesis or written about in the following paragraphs. The general outlook for ESR-STM experiments and our machine would be to expand the sam-

ple systems on which ESR signals can be measured. The idea of VOPcs could be returned to by depositing them on MgO, which guarantees that they would decoupled strongly enough from the substrate. ESR-STMs have also been recently shown to be able to coherently manipulate quantum states, which is a prerequisite for quantum computation. This, along with the demonstration of entangled spin states in ESR-STM experiments, leads us to believe that quantum information processing using individual atoms as qubits is a promising avenue for research in the field of ESR-STM.

After collecting a first data set that shows proof of principle of our machine, we set out to understand an observation that we first made when characterizing our ESR signals. That observation was the change in the ESR signal when measured at differing bias voltages. By doing bias-magnetic sweeps we are able to observe the bias dependent behaviour of ESR signals at one ZE. We see a shifting ESR signal with respect to to bias along with a background signal that seems to interact with the main ESR peak. We then strove to understand this shifting signal and found that it is due to changes in the *g*-factor and tip field that occur when changing the electric field in the junction. This interpretation was found to be consistent when adjusting the set point and the molecule's binding site in our experiment. After understanding this effect we also wanted to see how it could be used to control spin transitions in coupled dimers. We performed bias-magnetic sweeps on a strongly coupled dimer to show that the varying transitions move at different rates with respect to bias. Bringing the STM tip very closely, we were even able to induce a regime where several transitions are found at the same energy and we have modelled this behaivour using a conventional spin Hamiltonian. By designing specific dimers, we were also able to measure the avoided crossing of two entangled spin states using a bias-magnetic sweep and we were also able to show a way to place this avoided crossing at zero bias. This leads to a way of optimizing the coherence time between two entangle states (which would be of interest in regards to quantum computing) as the current is a direct source of decoherence in ESR-STM. With our demonstrations on coupled spin systems, we show that the bias in ESR-STM experiments is a powerful tuning parameter.

Even with the significant step in understanding this phenomenon, there are some remaining questions in regards to the source of the RF background and the change in the dependency of the *g*-factor on the bias that we have observed in TiH_O. We consider the first problem to be that of modelling, where the correct theory has to be formulated to understand the RF background. The second question regarding the *g*-factor dependency should be further investigated experimentally. We envision reproducing some of the experiments in this dissertation at more ZEs to increase statistics and improve the error in our analysis. Furthermore, we

could try to induce a similar transition on the dependency of the *g*-factor in the TiH_{OO} species by measuring at higher conductances. This project could be done in conjunction with experiments on dimers as we speculate that we could induce a regime were the bias pushes on the molecule beneath the tip and pulls on the molecule away from the tip. We would extract the *g*-factor and tip field dependencies with respect to bias for both molecules in the dimer, and use the change in the *g*-factor as a measure of the movement of the molecules. The complete set of goals for this project would be to investigate the dependency of the *g*-factor on the set point and bias and see if we indeed can push the molecule with the electric field if we bring the tip close enough. Then we would measure the tip field and *g*-factor dependencies on the set point, bias, and dimer length for dimers in order get a sense of the effect of the tip field and bias on the neighbouring molecule in the dimer. The final outlook for bias dependent ESR-STM, is to investigate the tip field dependency on the electric field. We see in this dissertation that the tip field moves linearly with bias, which leads to the question of how the spin system and Fe atom in the junction are changing relative to each other when the electric field is swept. This can, in principle, be directly observed using spatially-resolved ESR-STM, which has been shown to give information on the dipole and/or exchange interaction between the tip and spin system. Performing this experiment at many biases would lead to information on the change in this interaction, which could lead to the direct mapping of the movement of the spin system and Fe cluster on the apex at the tip.

Lastly, we performed temperature dependent measurements to observe the transition from an initialized experiment to a mixed state experiment. We show that there are some challenges that come with this experiment. The first challenge is that the sensitivity of the ESR signal is ZE dependent so this has to be considered and eliminated. We countered this by checking that the RF amplitude is consistent between each measurement, after each measurement, and by normalizing our data sets to the base temperature ESR signal magnitude. The second challenge came for an inconsistent signal baseline that we do not currently understand. This ultimately makes analysis difficult and any interpretation questionable. With these limitations we can model the general trend of the data, and speculate that the initialization of the system occurs near 1 K, but we do not reproduce the dependency of the data on the ZE. This is very likely due to us not considering spin initialization that the SP current facilitates in the experiment. Continuing to investigate this, along with the remainder of Chap. 8, may be the most promising avenue to continue research on this machine as it takes advantage of this machine's unique properties. Namely, the following project is proposed with the idea of studying thermally induced population dynamics. With the assumption that the ESR signal baseline is understood and consistent, we would measure dependencies of the ESR signal at various ZEs and temperatures, as we have done in this work, along with varying currents and

RF amplitudes. The goal here is to understand more deeply the role of the current on spin initialization and whether it is dependent on the spin splitting or population dynamics. The RF amplitude also directly effects the amplitude of the signal and this may also be related to the population dynamics or ZE. After these experiments, pump-probe functionality could be implemented. Not only is measuring the decay rate and coherence time of an initialized system as a function of ZE a fundamental experiment that is possible in our STM, the temporal dynamics of spins could be studied in relation to the population dynamics. With such a promising future, we believe that we can expect more interesting and novel research coming from our ESR-STM.

Bibliography

[1] Vanadyl phthalocyanine. https://www.sigmaaldrich.com/DE/de/product/aldrich/791997. Accessed: 2022-01-17.

[2] A. Andreev. Thermal conductivity of the intermediate state of superconductors ii. *Soviet Physics JETP*, 20:1490, 1965.

[3] F. Arute, K. Arya, R. Babbush, D. Bacon, J. C. Bardin, R. Barends, R. Biswas, S. Boixo, F. G. Brandao, D. A. Buell, et al. Quantum supremacy using a programmable superconducting processor. *Nature*, 574(7779):505–510, 2019.

[4] C. R. Ast, B. Jäck, J. Senkpiel, M. Eltschka, M. Etzkorn, J. Ankerhold, and K. Kern. Sensing the quantum limit in scanning tunnelling spectroscopy. *Nature communications*, 7(1):1–8, 2016.

[5] D. Averin and A. Bardas. ac josephson effect in a single quantum channel. *Physical Review Letters*, 75(9):1831, 1995.

[6] Y. Bae, K. Yang, P. Willke, T. Choi, A. J. Heinrich, and C. P. Lutz. Enhanced quantum coherence in exchange coupled spins via singlet-triplet transitions. *Science advances*, 4(11):eaau4159, 2018.

[7] A. V. Balatsky, M. Nishijima, and Y. Manassen. Electron spin resonance-scanning tunneling microscopy. *Advances in Physics*, 61(2):117–152, 2012.

[8] J. Bardeen, L. N. Cooper, and J. R. Schrieffer. Theory of superconductivity. *Physical Review*, 108(5):1175, 1957.

[9] A. Barone and G. Paterno. *Physics and applications of the Josephson effect*, volume 1. Wiley Online Library, 1982.

[10] S. Baumann, F. Donati, S. Stepanow, S. Rusponi, W. Paul, S. Gangopadhyay, I. Rau, G. Pacchioni, L. Gragnaniello, M. Pivetta, et al. Origin of perpendicular magnetic

anisotropy and large orbital moment in fe atoms on mgo. *Physical Review Letters*, 115(23):237202, 2015.

[11] S. Baumann, W. Paul, T. Choi, C. P. Lutz, A. Ardavan, and A. J. Heinrich. Electron paramagnetic resonance of individual atoms on a surface. *Science*, 350(6259):417–420, 2015.

[12] P. Berggren and J. Fransson. Electron paramagnetic resonance of single magnetic moment on a surface. *Scientific Reports*, 6(1):1–7, 2016.

[13] G. Binnig and H. Rohrer. Scanning tunneling microscopy—from birth to adolescence. *Reviews of Modern Physics*, 59(3):615, 1987.

[14] J. Bork, Y.-h. Zhang, L. Diekhöner, L. Borda, P. Simon, J. Kroha, P. Wahl, and K. Kern. A tunable two-impurity kondo system in an atomic point contact. *Nature Physics*, 7(11):901–906, 2011.

[15] M. Chauvin, P. Vom Stein, H. Pothier, P. Joyez, M. Huber, D. Esteve, and C. Urbina. Superconducting atomic contacts under microwave irradiation. *Physical review letters*, 97(6):067006, 2006.

[16] T. Choi, W. Paul, S. Rolf-Pissarczyk, A. J. Macdonald, F. D. Natterer, K. Yang, P. Willke, C. P. Lutz, and A. J. Heinrich. Atomic-scale sensing of the magnetic dipolar field from single atoms. *Nature Nanotechnology*, 12(5):420–424, 2017.

[17] L. N. Cooper. Bound electron pairs in a degenerate fermi gas. *Physical Review*, 104(4):1189, 1956.

[18] M. F. Crommie, C. P. Lutz, and D. M. Eigler. Confinement of electrons to quantum corrals on a metal surface. *Science*, 262(5131):218–220, 1993.

[19] J. Cuevas, J. Heurich, A. Martín-Rodero, A. L. Yeyati, and G. Schön. Subharmonic shapiro steps and assisted tunneling in superconducting point contacts. *Physical Review Letters*, 88(15):157001, 2002.

[20] J. Cuevas, A. Martín-Rodero, and A. L. Yeyati. Hamiltonian approach to the transport properties of superconducting quantum point contacts. *Physical Review B*, 54(10):7366, 1996.

[21] J. Cuevas, A. L. Yeyati, and A. Martín-Rodero. Microscopic origin of conducting channels in metallic atomic-size contacts. *Physical Review Letters*, 80(5):1066, 1998.

[22] J. C. Cuevas and W. Belzig. Full counting statistics of multiple andreev reflections. *Physical Review Letters*, 91(18):187001, 2003.

[23] R. W. Darbeau. Nuclear magnetic resonance (nmr) spectroscopy: a review and a look at its use as a probative tool in deamination chemistry. *Applied Spectroscopy Reviews*, 41(4):401–425, 2006.

[24] D. P. DiVincenzo. The physical implementation of quantum computation. *Fortschritte der Physik: Progress of Physics*, 48(9-11):771–783, 2000.

[25] R. Drost, T. Ojanen, A. Harju, and P. Liljeroth. Topological states in engineered atomic lattices. *Nature Physics*, 13(7):668–671, 2017.

[26] M. Eltschka, B. Jäck, M. Assig, O. V. Kondrashov, M. A. Skvortsov, M. Etzkorn, C. R. Ast, and K. Kern. Probing absolute spin polarization at the nanoscale. *Nano Letters*, 14(12):7171–7174, 2014.

[27] G. Falci, V. Bubanja, and G. Schön. Quasiparticle and cooper pair tenneling in small capacitance josephson junctions. *Zeitschrift für Physik B Condensed Matter*, 85(3):451–458, 1991.

[28] A. Ferrón, S. A. Rodríguez, S. S. Gómez, J. L. Lado, and J. Fernández-Rossier. Single spin resonance driven by electric modulation of the g-factor anisotropy. *Physical Review Research*, 1(3):033185, 2019.

[29] R. P. Feynman. There's plenty of room at the bottom [data storage]. *Journal of Microelectromechanical Systems*, 1(1):60–66, 1992.

[30] A. Filler. The history, development and impact of computed imaging in neurological diagnosis and neurosurgery: Ct, mri, and dti. *Nature Precedings*, pages 1–1, 2009.

[31] K. Franke, G. Schulze, and J. Pascual. Competition of superconducting phenomena and kondo screening at the nanoscale. *Science*, 332(6032):940–944, 2011.

[32] H.-J. Freund, M. Heyde, H. Kuhlenbeck, N. Nilius, T. Risse, T. Schmidt, S. Shaikhutdinov, and M. Sterrer. Chapter model systems in heterogeneous catalysis at the atomic level: a personal view. *Science China Chemistry*, 63(4):426–447, 2020.

[33] J. R. Gálvez, C. Wolf, F. Delgado, and N. Lorente. Cotunneling mechanism for all-electrical electron spin resonance of single adsorbed atoms. *Physical Review B*, 100(3):035411, 2019.

[34] M. Garg and K. Kern. Attosecond coherent manipulation of electrons in tunneling microscopy. *Science*, 367(6476):411–415, 2020.

[35] R. Gutzler, M. Garg, C. R. Ast, K. Kuhnke, and K. Kern. Light–matter interaction at atomic scales. *Nature Reviews Physics*, 3(6):441–453, 2021.

[36] A. Heinrich, C. Lutz, J. Gupta, and D. Eigler. Molecule cascades. *Science*, 298(5597):1381–1387, 2002.

[37] A. J. Heinrich, J. A. Gupta, C. P. Lutz, and D. M. Eigler. Single-atom spin-flip spectroscopy. *Science*, 306(5695):466–469, 2004.

[38] H. Huang, C. Padurariu, J. Senkpiel, R. Drost, A. L. Yeyati, J. C. Cuevas, B. Kubala, J. Ankerhold, K. Kern, and C. R. Ast. Tunnelling dynamics between superconducting bound states at the atomic limit. *Nature Physics*, 16(12):1227–1231, 2020.

[39] G.-L. Ingold, H. Grabert, and U. Eberhardt. Cooper-pair current through ultrasmall josephson junctions. *Physical Review B*, 50(1):395, 1994.

[40] M. W. Johnson, M. H. Amin, S. Gildert, T. Lanting, F. Hamze, N. Dickson, R. Harris, A. J. Berkley, J. Johansson, P. Bunyk, et al. Quantum annealing with manufactured spins. *Nature*, 473(7346):194–198, 2011.

[41] B. D. Josephson. Possible new effects in superconductive tunnelling. *Physics Letters*, 1(7):251–253, 1962.

[42] B. D. Josephson. The discovery of tunnelling supercurrents. *Reviews of Modern Physics*, 46(2):251, 1974.

[43] F. Kalff, M. P. Rebergen, E. Fahrenfort, J. Girovsky, R. Toskovic, J. L. Lado, J. Fernández-Rossier, and A. F. Otte. A kilobyte rewritable atomic memory. *Nature Nanotechnology*, 11(11):926–929, 2016.

[44] L. Keldysh et al. Ionization in the field of a strong electromagnetic wave. *Sov. Phys. JETP*, 20(5):1307–1314, 1965.

[45] J. Kim, W.-j. Jang, T. H. Bui, D.-J. Choi, C. Wolf, F. Delgado, Y. Chen, D. Krylov, S. Lee, S. Yoon, et al. Spin resonance amplitude and frequency of a single atom on a surface in a vector magnetic field. *Physical Review B*, 104(17):174408, 2021.

[46] C. Kittel and P. McEuen. *Kittel's Introduction to Solid State Physics*. John Wiley & Sons, 2018.

[47] Y. Kobayashi, T. Imai, and T. Sakakibara. Phenomenological description of" coherence peak" of high-tc superconductors by improved three-fluid model. In *1993 23rd European Microwave Conference*, pages 596–599. IEEE, 1993.

[48] J. Kondo. Resistance minimum in dilute magnetic alloys. *Progress of Theoretical Physics*, 32(1):37–49, 1964.

[49] P. Kot, R. Drost, M. Uhl, J. Ankerhold, J. C. Cuevas, and C. R. Ast. Microwave-assisted tunneling and interference effects in superconducting junctions under fast driving signals. *Physical Review B*, 101(13):134507, 2020.

[50] J. L. Lado, A. Ferrón, and J. Fernández-Rossier. Exchange mechanism for electron paramagnetic resonance of individual adatoms. *Physical Review B*, 96(20):205420, 2017.

[51] J. Liu, V. V. Laguta, K. Inzani, W. Huang, S. Das, R. Chatterjee, E. Sheridan, S. M. Griffin, A. Ardavan, and R. Ramesh. Coherent electric field manipulation of fe3+ spins in pbtio3. *Science Advances*, 7(10):eabf8103, 2021.

[52] J. Liu, J. Mrozek, W. K. Myers, G. A. Timco, R. E. Winpenny, B. Kintzel, W. Plass, and A. Ardavan. Electric field control of spins in molecular magnets. *Physical Review Letters*, 122(3):037202, 2019.

[53] J. Liu, J. Mrozek, A. Ullah, Y. Duan, J. J. Baldoví, E. Coronado, A. Gaita-Ariño, and A. Ardavan. Quantum coherent spin–electric control in a molecular nanomagnet at clock transitions. *Nature Physics*, 17(11):1205–1209, 2021.

[54] X.-g. Liu, H.-j. Du, B. Li, Y.-l. Zhao, A.-d. Zhao, and B. Wang. π-electron-assisted relaxation of spin excited states in cobalt phthalocyanine molecules on au (111) surface. *Chinese Journal of Chemical Physics*, 30(2):161–165, 2017.

[55] S. Loth, M. Etzkorn, C. P. Lutz, D. M. Eigler, and A. J. Heinrich. Measurement of fast electron spin relaxation times with atomic resolution. *Science*, 329(5999):1628–1630, 2010.

[56] S. Loth, K. Von Bergmann, M. Ternes, A. F. Otte, C. P. Lutz, and A. J. Heinrich. Controlling the state of quantum spins with electric currents. *Nature Physics*, 6(5):340–344, 2010.

[57] D. MacIsaac. A boy and his atom. *The Physics Teacher*, 57(4):270–270, 2019.

[58] L. Malavolti, M. Briganti, M. Hänze, G. Serrano, I. Cimatti, G. McMurtrie, E. Otero, P. Ohresser, F. Totti, M. Mannini, et al. Tunable spin–superconductor coupling of spin 1/2 vanadyl phthalocyanine molecules. *Nano letters*, 18(12):7955–7961, 2018.

[59] Y. Manassen, E. Ter-Ovanesyan, D. Shachal, and S. Richter. Electron spin resonance–scanning tunneling microscopy experiments on thermally oxidized si (111). *Physical Review B*, 48(7):4887, 1993.

[60] P. T. Mathew and F. Fang. Advances in molecular electronics: a brief review. *Engineering*, 4(6):760–771, 2018.

[61] J. Merkt. Entwurf und untersuchung einer antenne für 84ghz zur strahlungseinkopplung in ein stm. *Bachelor's thesis, Karlsruher Institut für Technologie,*, 2017.

[62] R. Meservey and P. Tedrow. Spin-polarized electron tunneling. *Physics Reports*, 238(4):173–243, 1994.

[63] E. Meyer, R. Bennewitz, and H. J. Hug. Introduction to scanning tunneling microscopy. In *Scanning Probe Microscopy*, pages 13–45. Springer, 2021.

[64] J. S. Moodera, G.-X. Miao, and T. S. Santos. Frontiers in spin-polarized tunneling. *Phys. Today*, 63(4):46–51, 2010.

[65] T. Nan, Y. Lee, S. Zhuang, Z. Hu, J. D. Clarkson, X. Wang, C. Ko, H. Choe, Z. Chen, D. Budil, et al. Electric-field control of spin dynamics during magnetic phase transitions. *Science Advances*, 6(40):eabd2613, 2020.

[66] F. D. Natterer, K. Yang, W. Paul, P. Willke, T. Choi, T. Greber, A. J. Heinrich, and C. P. Lutz. Reading and writing single-atom magnets. *Nature*, 543(7644):226–228, 2017.

[67] M. Octavio, M. Tinkham, G. Blonder, and T. Klapwijk. Subharmonic energy-gap structure in superconducting constrictions. *Physical Review B*, 27(11):6739, 1983.

[68] W. Paul, S. Baumann, C. P. Lutz, and A. J. Heinrich. Generation of constant-amplitude radio-frequency sweeps at a tunnel junction for spin resonance stm. *Review of Scientific Instruments*, 87(7):074703, 2016.

[69] W. Paul, K. Yang, S. Baumann, N. Romming, T. Choi, C. P. Lutz, and A. J. Heinrich. Control of the millisecond spin lifetime of an electrically probed atom. *Nature Physics*, 13(4):403–407, 2017.

[70] O. Peters, N. Bogdanoff, S. A. González, L. Melischek, J. R. Simon, G. Reecht, C. B. Winkelmann, F. von Oppen, and K. J. Franke. Resonant andreev reflections probed by photon-assisted tunnelling at the atomic scale. *Nature Physics*, 16(12):1222–1226, 2020.

[71] S.-H. Phark, Y. Chen, C. Wolf, H. T. Bui, Y. Wang, M. Haze, J. Kim, C. P. Lutz, A. J. Heinrich, and Y. Bae. Double electron spin resonance of engineered atomic structures on a surface. *arXiv preprint arXiv:2108.09880*, 2021.

[72] S.-h. Phark and D. Sander. Spin-polarized scanning tunneling microscopy with quantitative insights into magnetic probes. *Nano Convergence*, 4(1):1–17, 2017.

[73] M. Planck. The theory of heat radiation. *Entropie*, 144(190):164, 1900.

[74] N. Quaas, M. Wenderoth, A. Weismann, R. Ulbrich, and K. Schönhammer. Kondo resonance of single co atoms embedded in cu (111). *Physical Review B*, 69(20):201103, 2004.

[75] E. Rashba and V. Sheka. Symmetry of energy bands in crystals of wurtzite type ii. symmetry of bands with spin-orbit interaction included. *New J. Phys.*, (17):050202, 2015.

[76] I. G. Rau, S. Baumann, S. Rusponi, F. Donati, S. Stepanow, L. Gragnaniello, J. Dreiser, C. Piamonteze, F. Nolting, S. Gangopadhyay, et al. Reaching the magnetic anisotropy limit of a 3d metal atom. *Science*, 344(6187):988–992, 2014.

[77] N. Romming, C. Hanneken, M. Menzel, J. E. Bickel, B. Wolter, K. von Bergmann, A. Kubetzka, and R. Wiesendanger. Writing and deleting single magnetic skyrmions. *Science*, 341(6146):636–639, 2013.

[78] A. M. Roslawska. Dynamics of nanoscale systems probed by time-resolved stm-induced luminescence. Technical report, EPFL, 2019.

[79] A. Roychowdhury, M. Dreyer, J. Anderson, C. Lobb, and F. Wellstood. Microwave photon-assisted incoherent cooper-pair tunneling in a josephson stm. *Physical Review Applied*, 4(3):034011, 2015.

[80] A. Rusinov. Superconductivity near a paramagnetic impurity. *JETP Lett. USSR*, 9, 1969.

[81] S. Sahoo, T. Kontos, J. Furer, C. Hoffmann, M. Gräber, A. Cottet, and C. Schönenberger. Electric field control of spin transport. *Nature Physics*, 1(2):99–102, 2005.

[82] M. P. Sarachik. Resistivity of some 5 d elements and alloys containing iron. *Physical Review*, 170(3):679, 1968.

[83] T. S. Seifert, S. Kovarik, D. M. Juraschek, N. A. Spaldin, P. Gambardella, and S. Stepanow. Longitudinal and transverse electron paramagnetic resonance in a scanning tunneling microscope. *Science Advances*, 6(40):eabc5511, 2020.

[84] T. S. Seifert, S. Kovarik, C. Nistor, L. Persichetti, S. Stepanow, and P. Gambardella. Single-atom electron paramagnetic resonance in a scanning tunneling microscope driven by a radio-frequency antenna at 4 k. *Physical Review Research*, 2(1):013032, 2020.

[85] J. Senkpiel, S. Dambach, M. Etzkorn, R. Drost, C. Padurariu, B. Kubala, W. Belzig, A. L. Yeyati, J. C. Cuevas, J. Ankerhold, et al. Single channel josephson effect in a high transmission atomic contact. *Communications Physics*, 3(1):1–6, 2020.

[86] A. M. Shakirov, A. N. Rubtsov, and P. Ribeiro. Spin transfer torque induced paramagnetic resonance. *Physical Review B*, 99(5):054434, 2019.

[87] S. Shapiro. Josephson currents in superconducting tunneling: The effect of microwaves and other observations. *Physical Review Letters*, 11(2):80, 1963.

[88] G. Shavit, B. Horovitz, and M. Goldstein. Generalized open quantum system approach for the electron paramagnetic resonance of magnetic atoms. *Physical Review B*, 99(19):195433, 2019.

[89] H. Shiba. Classical spins in superconductors. *Progress of Theoretical Physics*, 40(3):435–451, 1968.

[90] R. Sk and A. Deshpande. Unveiling the emergence of functional materials with stm: metal phthalocyanine on surface architectures. *Molecular Systems Design & Engineering*, 4(3):471–483, 2019.

[91] J. Stark. Observation of the separation of spectral lines by an electric field. *Nature*, 92(2301):401–401, 1913.

[92] M. Steinbrecher, W. M. Van Weerdenburg, E. F. Walraven, N. P. Van Mullekom, J. W. Gerritsen, F. D. Natterer, D. I. Badrtdinov, A. N. Rudenko, V. V. Mazurenko, M. I. Katsnelson, et al. Quantifying the interplay between fine structure and geometry of an individual molecule on a surface. *Physical Review B*, 103(15):155405, 2021.

[93] B. C. Stipe, M. A. Rezaei, and W. Ho. Single-molecule vibrational spectroscopy and microscopy. *Science*, 280(5370):1732–1735, 1998.

[94] J. A. Stroscio and D. Eigler. Atomic and molecular manipulation with the scanning tunneling microscope. *Science*, 254(5036):1319–1326, 1991.

[95] M. Ternes. Scanning tunneling spectroscopy at the single atom scale. Technical report, EPFL, 2006.

[96] M. Ternes, C. González, C. P. Lutz, P. Hapala, F. J. Giessibl, P. Jelínek, and A. J. Heinrich. Interplay of conductance, force, and structural change in metallic point contacts. *Physical Review Letters*, 106(1):016802, 2011.

[97] M. Ternes, A. J. Heinrich, and W.-D. Schneider. Spectroscopic manifestations of the kondo effect on single adatoms. *Journal of Physics: Condensed Matter*, 21(5):053001, 2008.

[98] J. Tersoff and D. R. Hamann. Theory of the scanning tunneling microscope. *Physical Review B*, 31(2):805, 1985.

[99] P. Tien and J. Gordon. Multiphoton process observed in the interaction of microwave fields with the tunneling between superconductor films. *Physical Review*, 129(2):647, 1963.

[100] F. Trier, D. C. Vaz, P. Bruneel, P. Noël, A. Fert, L. Vila, J.-P. Attané, A. Barthélémy, M. Gabay, H. Jaffrès, et al. Electric-field control of spin current generation and detection in ferromagnet-free srtio3-based nanodevices. *Nano letters*, 20(1):395–401, 2019.

[101] G. L. Trigg and W. Greulich. *Encyclopedia of Applied Physics*, volume 1. VCH New York, 1991.

[102] M. Uecker, S. Zhang, D. Voit, A. Karaus, K.-D. Merboldt, and J. Frahm. Real-time mri at a resolution of 20 ms. *NMR in Biomedicine*, 23(8):986–994, 2010.

[103] W. M. van Weerdenburg, M. Steinbrecher, N. P. van Mullekom, J. W. Gerritsen, H. von Allwörden, F. D. Natterer, and A. A. Khajetoorians. A scanning tunneling microscope capable of electron spin resonance and pump–probe spectroscopy at mk temperature and in vector magnetic field. *Review of Scientific Instruments*, 92(3):033906, 2021.

[104] L. M. Veldman, L. Farinacci, R. Rejali, R. Broekhoven, J. Gobeil, D. Coffey, M. Ternes, and A. F. Otte. Free coherent evolution of a coupled atomic spin system initialized by electron scattering. *Science*, 372(6545):964–968, 2021.

[105] Y. Wang, K. Wu, J. Kroeger, and R. Berndt. Structures of phthalocyanine molecules on surfaces studied by stm. *AIP Advances*, 2(4):10400, 2012.

[106] J. Wei, Y. Zhang, H. Ou, B. Xie, D. Shen, J. Zhao, L. Yang, M. Arita, K. Shimada, H. Namatame, et al. Superconducting coherence peak in the electronic excitations of a single-layer bi 2 sr 1.6 la 0.4 cuo 6+ δ cuprate superconductor. *Physical Review Letters*, 101(9):097005, 2008.

[107] R. Wiesendanger. Spin mapping at the nanoscale and atomic scale. *Reviews of Modern Physics*, 81(4):1495, 2009.

[108] P. Willke, W. Paul, F. D. Natterer, K. Yang, Y. Bae, T. Choi, J. Fernández-Rossier, A. J. Heinrich, and C. P. Lutz. Probing quantum coherence in single-atom electron spin resonance. *Science Advances*, 4(2):eaaq1543, 2018.

[109] P. Willke, K. Yang, Y. Bae, A. J. Heinrich, and C. P. Lutz. Magnetic resonance imaging of single atoms on a surface. *Nature Physics*, 15(10):1005–1010, 2019.

[110] S. A. Wolf, A. Y. Chtchelkanova, and D. M. Treger. Spintronics—a retrospective and perspective. *IBM Journal of Research and Development*, 50(1):101–110, 2006.

[111] K. Yang, Y. Bae, W. Paul, F. D. Natterer, P. Willke, J. L. Lado, A. Ferrón, T. Choi, J. Fernández-Rossier, A. J. Heinrich, et al. Engineering the eigenstates of coupled spin-1/2 atoms on a surface. *Physical review letters*, 119(22):227206, 2017.

[112] K. Yang, W. Paul, F. D. Natterer, J. L. Lado, Y. Bae, P. Willke, T. Choi, A. Ferrón, J. Fernández-Rossier, A. J. Heinrich, et al. Tuning the exchange bias on a single atom from 1 mt to 10 t. *Physical Review Letters*, 122(22):227203, 2019.

[113] K. Yang, W. Paul, S.-H. Phark, P. Willke, Y. Bae, T. Choi, T. Esat, A. Ardavan, A. J. Heinrich, and C. P. Lutz. Coherent spin manipulation of individual atoms on a surface. *Science*, 366(6464):509–512, 2019.

[114] K. Yang, S.-H. Phark, Y. Bae, T. Esat, P. Willke, A. Ardavan, A. J. Heinrich, and C. P. Lutz. Probing resonating valence bond states in artificial quantum magnets. *Nature Communications*, 12(1):1–7, 2021.

[115] K. Yang, P. Willke, Y. Bae, A. Ferrón, J. L. Lado, A. Ardavan, J. Fernández-Rossier, A. J. Heinrich, and C. P. Lutz. Electrically controlled nuclear polarization of individual atoms. *Nature Nanotechnology*, 13(12):1120–1125, 2018.

[116] A. Yazdani, B. Jones, C. Lutz, M. Crommie, and D. Eigler. Probing the local effects of magnetic impurities on superconductivity. *Science*, 275(5307):1767–1770, 1997.

[117] L. Yu. Bound state in superconductors with paramagnetic impurities. *Acta. Phys. Sin.*, 21(1):75, 1965.

[118] E. Zavoisky. Spin-magnetic resonance in paramagnetics. *J. Phys. USSR*, 9:211–245, 1945.

[119] X. Zhang, C. Wolf, Y. Wang, H. Aubin, T. Bilgeri, P. Willke, A. J. Heinrich, and T. Choi. Electron spin resonance of single iron phthalocyanine molecules and role of their non-localized spins in magnetic interactions. *Nature Chemistry*, 14(1):59–65, 2022.

[120] Y.-h. Zhang, S. Kahle, T. Herden, C. Stroh, M. Mayor, U. Schlickum, M. Ternes, P. Wahl, and K. Kern. Temperature and magnetic field dependence of a kondo system in the weak coupling regime. *Nature communications*, 4(1):1–6, 2013.

[121] A. Zheltikov. Keldysh parameter, photoionization adiabaticity, and the tunneling time. *Physical Review A*, 94(4):043412, 2016.

Declaration

I affirm, that the presented thesis was written self-dependently and only the stated sources and resources were used. The submitted work was neither completely nor partly part of an other examination procedure. The content of the electronic version is identical to the printed version.

Stuttgart, March 23rd 2022

_____

Piotr Kot